
Thermoelectric Energy Conversion and Water Purification by Metal Chalcogenides and Layered Materials

A thesis submitted in Fulfillment of the Degree of

MASTER OF SCIENCE

as a part of

Integrated Ph.D. Program (Chemical Science)

By

Animesh Das



J N C A S R

New Chemistry Unit

**Jawaharlal Nehru Centre for Advanced Scientific
Research**

(A deemed University)

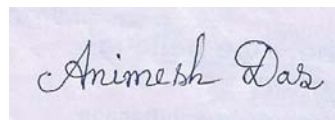
Bangalore, India

(March 2022)

Dedicated to my beloved family

DECLARATION

I hereby declare that this thesis entitled “Thermoelectric Energy Conversion and Water Purification by Metal Chalcogenides and Layered Materials” is a bonafide record of research work that has been carried out by me at Solid State Chemistry Laboratory, New Chemistry Unit, Jawaharlal Nehru Centre for Advanced Scientific Research, Bangalore, India under supervision of Prof. Kanishka Biswas. This work has not been submitted elsewhere for the award of any degree or diploma. Whenever contributions of others are required, every effort is made to indicate it clearly, with due reference to the literature, and acknowledgement of collaborative research and discussions.

A rectangular box containing a handwritten signature in black ink that reads "Animesh Das".

Animesh Das

Date: 31.03.2022

Bangalore, India



Kanishka Biswas, Ph.D., FRSC

Associate Professor

New Chemistry Unit

Jawaharlal Nehru Centre for

Advanced Scientific Research (JNCASR)

Bangalore, India -560064

Executive Editor, ACS Applied Energy Materials

Email :kanishka@jncasr.ac.in

Phone: +91-80-22082678 (office)

+91-9902063469 (mobile)

FAX : +91-80-2208-2627

Web: <http://www.jncasr.ac.in/kanishka/>

CERTIFICATE

Certified that the work described in this thesis titled “**Thermoelectric Energy Conversion and Water Purification by Metal Chalcogenides and Layered Materials**” has been carried out by Mr. Animesh Das at Solid State Chemistry Laboratory, New Chemistry Unit, Jawaharlal Nehru Centre for Advanced Scientific Research, Bangalore, India under my supervision and that it has not been submitted elsewhere for the award of any degree or diploma.

Date: 31.03.2022

Bangalore, India

Prof. Kanishka Biswas

(Research Supervisor)

Acknowledgements

The fulfilment of my MS-Thesis required guidance and support from innumerable people. I would like to take this opportunity to thank some of them. However, my sincerest thanks extend to the people whom I have unintentionally missed mentioning in this section.

First and foremost, I would like to thank my supervisor, Prof. Kanishka Biswas. Since the first day I entered his lab, we had fruitful discussion about several research problems and he has guided me throughout. I admire his enthusiasm towards science to the greatest extent possible and this enthusiasm has made me work as best as I could. From the bottom of my heart, I appreciate him for giving me a chance to be a part of his research group and work under his guidance. I am greatly obliged to him for showing immense patience towards me by correcting me at my every wrong step and forgiving my mistakes.

I would like to thank Prof. C. N. R. Rao, FRS, the former chairman of New Chemistry Unit (NCU) for providing me with such immense inspiration. The zeal with which he practices science, even at his age, is truly inspiring. His presence has given me immense encouragement to indulge in active research.

I would like to thank Prof. Subi Jacob George, the current chairman of New Chemistry Unit (NCU) for providing the infrastructure and facilities to carry out my research work.

I would like to thank my past and present lab members – Dr Shidaling, Dr Tanmoy, Dr Kaushik, Dr Prabir, Dr Archana, Dr Gopal, Dr Jayita, Mr Subarna, Dr. Abdul, Dr Ananya, Dr Subhajit, Dr Manisha, Dr. Ekashmi, Dr. Moinak, Krishnendu Paribesh, Sushmita, Debattam, Animesh Bhui, Anustoop, Anupama, Ivy, Vaishali, Aman and last but not the least Subhajit Das for keeping a cheerful and healthy working environment in the lab. I have received tremendous guidance from them in learning the instruments in the lab and their valuable inputs in research life have helped me immensely.

I am thankful to my course instructors- Dr. Premkumar Senguttuvan, Dr. Sarit Agasti, Prof. Alok Nath Chakraborty, Prof. Eshwaramurthy Muthusamy, Prof. Sreedhar Rajaram, Prof. A Sundaresan, Prof. Tapas Kumar Maji, Prof. Ranjini Viswanatha, Prof. Subi Jacob George, Dr. Bivas Saha, Prof. Sebastian C. Peter, Prof. Kanishka Biswas and Prof. Jayanta Haldar. I have been successful in gaining knowledge in different fields of research by attending their courses.

Constant assistance and a friendly nature of the technical staff helped me doing my experiments smoothly. I would like to thank Dr. Jay Ghatak (TECHNAI-TEM), Mrs. Meenakshi (SEM), Mr. Rahul (TEM), Mr. Kanan (SEM), Mr. Vasu (Band Gap) and Mr. Sachin (SEM) for their technical help. I am thankful to all the academic, administrative, technical, security, Complab, Utility and health centre staffs for making our campus life smooth and easy.

I am thankful to my batchmates – Aasish, Uttam, Dipanjana, Surabhi, Sohini, Aditya, Amit, Anustup, Vinay, Arif for their joyful companionship which made academic and non-academic life in JNCASR easier. I would like to thank Tarak for being such an incredible roommate and for engaging in interactive scientific discussions whenever it was needed.

A special thanks to Mr. Paribesh for always being there for me, for supporting me when needed and tolerating all my shenanigans.

I would like to thank my respected teachers from my alma-mater (Burdwan Municipal High School and Jadavpur University) for growing my interest in research field. I am thankful to my

school and college friends –Ayan, Rik, Joydeep, Sabyasachi, Reyana, Monalisa, Kingshuk, Soumyadip, Aritra, Arko for being there for me when needed.

I have benefited a lot from my Ph.D seniors and Post docs. Their help and advice made my academic and non-academic life a memorable and comfortable one here at JNCASR. Special thanks to Purnendu, Ritam, Subhajit, Subham, Triparna, Souvik, Sabyasachi for all the moments I spent with them.

I would also like to thank my elder brother Paramesh (currently doing Ph.D in JNCASR) for making my life more happier and cheerful in Bangalore.

Simple words of thanks are never enough to convey my feelings for my parents who have supported me and trusted me throughout my life. I will be forever grateful to them for what they have done for me and I dedicate my thesis to them.

Preface

Metal chalcogenides, Chalcophosphates and Three-dimensional Layered Double Hydroxide present an important platform for exploring various intriguing properties. This MS thesis present the design and synthesis of various metal chalcogenides, layered chalcophosphates for their application in thermoelectric energy conversion and water purification. This thesis work is divided into three parts (1-3), containing two chapters in each of them.

Part 1 presents a brief introduction to metal chalcogenides and chalcophosphates for energy conversion and environmental remediation, covering the summary of thermoelectric, ion-exchange, intercalation, water purification, synthesis and measurement techniques. It is divided into two chapters. **Chapter 1.1** of the thesis begins with a brief introduction to the thermoelectric effect, its conflicting parameters and the useful approaches required for the enhancement of the thermoelectric figure of merit. In this Chapter, I have also described some state-of-art thermoelectric material along with the present understandings and latest development. **Chapter 1.2** begins with a brief introduction to intercalation and ion exchange chemistry in layered inorganic solids and its useful approaches to solve water pollution related issues. Herein, I have discussed various state of art inorganic materials and their intercalation and ion exchange properties with latest development.

Part 2 of my thesis is related to energy conversion and is focused on the design and synthesis of metal chalcogenides (mainly, GeTe based systems) for high performance thermoelectric energy conversion. It is also divided into two chapters. **Chapter 2.1** of this part deals with the elevation of thermoelectric figure of merit to ~ 2.1 at 723 K in ball milled and sps processed $\text{Ge}_{1-2x}\text{Pb}_x\text{Sn}_x\text{Te}$. Initially, the addition of equimolar PbTe and SnTe in the GeTe reduces the κ_L by effective phonon scattering owing to excess point defects and rich microstructures. In the second step, introduction of Sb doping leads additional phonon scattering centers and optimizes the p-type carrier concentration and finally, ball milled and sps processed 11 mol% Sb-doped $\text{Ge}_{0.95}\text{Pb}_{0.025}\text{Sn}_{0.025}\text{Te}$ exhibits ultralow κ_L of ~ 0.60 W/m.K at 300 K. Subsequently, ball milled 11 mol% Sb-doped $\text{Ge}_{0.95}\text{Pb}_{0.025}\text{Sn}_{0.025}\text{Te}$ exhibits high TE figure of merit (zT) of ~ 2.1 at 723 K. Further, we have achieved a high output power, ~ 240 mW for the temperature difference of 434 K, in single leg TE device based on 11 mol% Sb-doped ball milled $\text{Ge}_{0.95}\text{Pb}_{0.025}\text{Sn}_{0.025}\text{Te}$. In **Chapter 2.2**, we unraveled the complimentary role of Sn and Bi doping in GeTe system with a high thermoelectric performance. In this chapter, we have demonstrated the reduction of κ_L of ball milled and SPS processed $\text{Ge}_{0.91}\text{Sn}_{0.03}\text{Bi}_{0.06}\text{Te}$ very near to its κ_{min} . Initially, the addition of 3 mol % Sn and 6 mol % Bi in the GeTe reduces the κ_L by optimizing the p type carrier concentration and effective phonon scattering owing to excess point defects. In the second step, ball milled and SPS were performed on the optimized $\text{Ge}_{0.91}\text{Sn}_{0.03}\text{Bi}_{0.06}\text{Te}$, resulting very low κ_L of 0.57 W/m.K at exhibiting high TE figure of merit (zT) of ~ 1.9 at 623 K.

Part 3 of my thesis is related to selective and efficient removal of heavy metals from water as environmental remediation by inorganic layered materials. In **Chapter 3.1**, I discuss about the detailed Cd^{2+} adsorption and ion-exchange kinetics of layered metal chalcophosphate, $\text{K}_{0.48}\text{Mn}_{0.76}\text{PS}_3 \cdot \text{H}_2\text{O}$ (K-MPS-1). K-MPS-1 is capable of efficient removal of Cd^{2+} ($>99\%$) from very dilute concentration (1-1000 ppb) selectively even in presence of other monovalent and divalent cations such as Na^+ , Ca^{2+} , Mg^{2+} . It can operate within a broad pH range of 2-12

effectively with high distribution co-efficient (K_d^{Cd}) of $\sim 10^4$ mL/g. In **Chapter 3.2**, we have shown that the nature-inspired coral like layered Co, Al-LDH selectively and efficiently sequesters toxic oxoanions As (V) and Se (IV) in a very wide pH range from ~ 1.9 to 12.5 and with a high capacity of 129.22 mg g^{-1} for As (V) and 130.56 mg g^{-1} for Se (IV). The high adsorption capacity for As (V) and Se (IV) are superior of other reported adsorbents, indicating the great potential of this material for trapping these oxoanions. The adsorption equilibrium is reached within ten minutes for both of them, indicating very rapid removal of As (V) and Se (IV) from wastewater by Co, AL-LDH. The reason for rapid removal can be attributed to the weak bonding interaction between SeO_3^{2-} and AsO_4^{3-} towards brucite-like layers which promotes the efficient anion exchange.

Contents

Declaration -----	III
Certificate-----	V
Acknowledgements -----	VII
Preface -----	IX
Contents-----	XI

PART-1. A Brief Introduction to Thermoelectric Energy Conversion and Water Purification as Environmental Remediation.

Chapter 1.1. A Brief Overview of Thermoelectric Energy Conversion---1

1.1.1. Introduction -----	3
1.1.2. Thermoelectric effect and thermoelectric figure of merit-----	4
1.1.3. Clashing thermoelectric parameters and ways to optimization-----	8
1.1.3.1. Conflicting thermoelectric parameter-----	8
1.1.3.1.1. Carrier concentration-----	8
1.1.3.1.2. Effective mass-----	10
1.1.3.1.3. Electrical thermal conductivity-----	10
1.1.3.1.4. Lattice thermal conductivity-----	11
1.1.3.2. Enhancement of power factor-----	12
1.1.3.2.1. Resonance level-----	13
1.1.3.2.2. Valence band convergence-----	14
1.1.4. Metal chalcogenides based high-performance thermoelectrics----	15
1.1.4.1. Germanium Telluride-----	16
1.1.4.1.1. Crystal structure-----	17
1.1.4.1.2. Thermoelectric properties-----	17
1.1.5. Summary-----	20
1.1.6. References-----	22

Chapter 1.2. A Brief Introduction to Intercalation and Ion-Exchange Reactions -----	25
1.2.1 Layered inorganic solids and intercalation chemistry-----	26
1.2.1.1 Intercalation reactions -----	28
1.2.1.2 Insulating 2D host lattices for intercalation-----	29
1.2.1.3 Redox active 2D host lattices for intercalation-----	31
1.2.2 Ion-exchange reactions-----	32
1.2.2.1 Mechanism of ion-exchange reactions -----	33
1.2.2.2 Ion-exchange reactions of layered inorganic solids---	33
1.2.3 Metal chalcophosphates -----	38
1.2.3.1 Molecular intercalations-----	39
1.2.3.2 Intercalations of organometallic molecules-----	39
1.2.3.3 Cationic substitution-intercalation -----	40
1.2.3.4 Ion-exchange in MPS ₃ -----	41
1.2.4 Summary-----	42
1.2.5 References -----	43

PART 2: Enhanced Thermoelectric Performance in GeTe Based Materials.

Chapter 2.1. Low Thermal conductivity and High Seebeck Coefficient Leads to High Thermoelectric Performance in Pseudoternary Ge_{1-2x}Pb_xSn_xTe -----	47
Summary-----	48
2.1.1 Introduction -----	49
2.1.2 Methods -----	50
2.1.3. Results and discussion -----	52
2.1.4 Conclusion-----	63
2.1.5 References -----	64

Chapter 2.2. Complementary co-doping of Sn and Bi Leads to Enhanced Thermoelectric Figure of Merit in GeTe----- 67

Summary ----- 68

2.2.1 Introduction----- 69

2.2.2 Methods----- 70

2.2.3. Results and discussion ----- 72

2.2.4 Conclusion----- 79

2.2.5 References ----- 80

PART 3: Selective and Efficient Removal of Heavy Metals from Water by Inorganic Layered Materials.

Chapter 3.1. Efficient Sequestration of Cd (II) from Water up to ppb Level by Layered Metal Chalcophosphate ----- 82

Summary-----83

3.1.1 Introduction----- 84

3.1.2 Experimental section ----- 85

3.1.3. Results and discussion----- 87

3.1.4 Conclusion----- 100

3.3.5 References ----- 101

Chapter 3.2. Hierarchical Layered Double Hydroxide as a Swift and Efficient Scavenger for Toxic Anions AsO_4^{3-} and SeO_3^{2-} from Water ----- 104

Summary ----- 105

3.2.1 Introduction----- 106

3.2.2 Experimental section ----- 108

3.2.3. Results and discussion----- 109

3.2.4 Conclusion----- 123

3.2.5 References----- 125

BIOGRAPHY 128

PART 1

**A Brief Introduction to
Thermoelectric Energy Conversion
and Water Purification as
Environmental Remediation.**

Chapter 1.1

A Brief Overview of Thermoelectric Energy Conversion

Chapter 1.1

A BRIEF OVERVIEW OF THERMOELECTRIC ENERGY CONVERSION

1.1.1 Introduction.

Ever growing energy consumption and increasingly grievous environmental issues have drawn ample awareness in recent years. To curb this energy crisis which is looming in large, exploring sustainable and eco-friendly energy resources has considerable significance. Driven by this huge demand for clean and sustainable energy sources, thermoelectric materials and devices, based on the direct energy conversion between heat and electricity, have been considered as promising alternative materials for power generation¹⁻³ as $\sim 65\%$ of the total energy is inevitably lost through heat dissipation⁴ (Figure 1). The thermoelectric materials and devices are successful in recycling the waste heat energy which are produced in large amount through automobile exhaust, domestic heating exhaust and industrial processes. Furthermore, thermoelectric devices are all-solid-state devices well equipped without any mobile parts thus making them tailor-made for small scale power generation and distribution². Additionally, thermoelectric materials have found its place as the most important power source in distant terrestrial and extra-terrestrial environment especially in deep space probes like Voyager, Cassini etc^{5, 6}. In this chapter, I will briefly discuss the origin of thermoelectric effect, the conflicting parameters in this field and some of the most well-known and widely researched upon materials in this field.

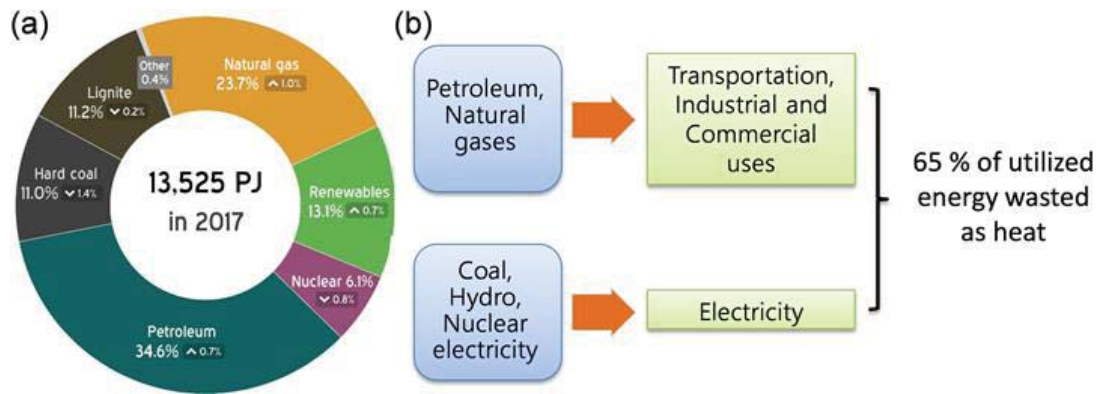


Figure 1. (a) Total energy consumption by type for India in year 2017 in petajoules and percents. (b) Schematic demonstrates how ~65 % of the utilized energy being lost as waste heat.

1.1.2 Thermoelectric effect and thermoelectric figure of merit

The thermoelectric effect is a phenomenon by which a temperature difference is directly converted to electric voltage and vice versa. It is based on two different transport effects- Seebeck effect and Peltier effect.

The Seebeck effect is a thermoelectric phenomenon discovered in 1821 by Thomas Johann Seebeck. It arises when electricity is created between a thermocouple as soon as the ends are subjected to a temperature difference between them.⁷ The voltage difference created between the two ends (ΔV) is directly proportional to the temperature difference (ΔT) and the ratio of the former and the latter is known as Seebeck Co-efficient (S) or thermopower⁸ (equation 1). This effect can be realized by initiating a temperature difference across a material- the more excited carriers of hot junction diffuse to the colder junction till an electric field is established to inhibit the further flow of carriers.

$$S = \frac{\Delta V}{\Delta T} \quad (1)$$

When an electric current is passed through a circuit of a thermocouple, heat is evolved at one junction and absorbed at the other junction. This is known as the Peltier Effect. and is named after French physicist Jean Charles Athanase Peltier, who discovered it in 1834. The

evolution or absorption of heat. Fully depends upon the direction of applied current. In a Peltier cooler, the circuit is connected to a d.c supply which derives the electric current (I) and heat flow (Q), thereby cooling the hot end due to the peltier effect⁹. ($Q = STI$, where T is the temperature in Kelvin scale)

Seebeck Coefficient is very low for metals (of the order of $\sim 10^0$ - 10^1 $\mu\text{V/K}$) and much larger for semiconductors (10^2 - 10^3 $\mu\text{V/K}$). Seebeck co-efficient is positive for p-type semiconductors where the majority carriers are holes. On the other hand, S is negative for n-type semiconductors where the majority carriers are electrons. For example, degenerate semiconductor like $\text{Sn}_{1.03}\text{Te}$ has a Seebeck of ~ 90 $\mu\text{V/K}$ at high temperature. Thus use of semiconductor or degenerate semiconductors can offer considerable amount of voltage generation for a given temperature gradient thus acting as a decent thermoelectric materials.¹

10

A customary thermoelectric (TE) couple consists of both p-type and n-type semiconductors connected through a metallic pad which is conducting. A TE module or device comprises of an array of TE couples which are arranged electrically in series and thermally in parallel. Power generation as well as refrigeration are achieved through the same module (Figure 2). In a thermoelectric device, when temperature gradient is applied, the thermally energised hole from p-type and electrons from n-type disseminate towards the cold side from the hot side and thus generate power to the electrical load connected to an external circuit. (Figure 2). Power output is determined by the heat flow which drives the electrical current and the temperature gradient produces voltage as mentioned earlier.² In this way thermoelectric devices/modules convert heat (localised waste heat) into electricity or vice versa and this can be implemented for waste heat utilization in different automobiles, steel plants, thermal

management in microprocessors (Seebeck Effect) or can be used as portable coolers (Peltier effect).

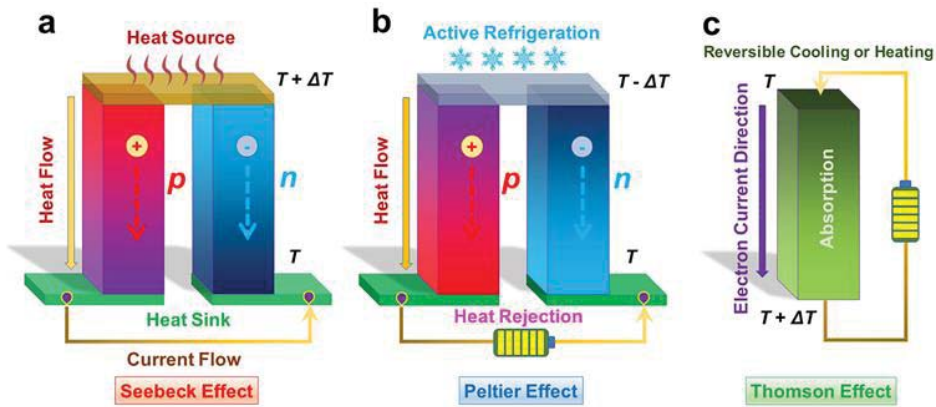


Figure 2 Schematic illustrations of a thermoelectric (TE) module for (a) power generation-Seebeck effect, (b) active refrigeration-Peltier effect and (c) Thomson effect (Ref. 2 © 2020 Chem. Rev.)

The usefulness of a material in thermoelectric systems is determined by the device efficiency. These are determined by the material's electrical conductivity (σ), thermal conductivity (κ), Seebeck coefficient (S) which change with temperature. The maximum efficiency of the energy conversion process (for both power generation and cooling) at a given point in the material is determined by the thermoelectric figure of merit, zT . (Equation 2)

$$zT = \frac{\sigma \cdot S^2}{\kappa} T \quad (2)$$

First introduced by E. Altenkirch in 1900s, he qualitatively showed that a good thermoelectric material should have a high zT i.e a high electrical conductivity like that of metals to minimise Joule heating, a high Seebeck coefficient like that of a semiconductor for maximum conversion of heat to electrical power and vice versa and low thermal conductivity like that of an insulator to preserve the heat at the junctions and maintain a large temperature gradient.

The term σS^2 is known as power factor and it is pivotal for achieving high thermoelectric figure of merit. High power factor means a large voltage and a high current generation. The thermal conductivity, κ has contributions from two factors) i) electrical thermal conductivity (κ_{el}) where

the heat is carried by the carriers present in the system and ii) lattice thermal conductivity (κ_{lat}) where heat is propagated through vibration of bonds or phonons. Thus, we can say, $\kappa = \kappa_{\text{el}} + \kappa_{\text{lat}}$. The efficiency of a thermoelectric device for electricity generation is given by η defined as

$$\eta = \frac{\text{energy provided to the load}}{\text{heat energy absorbed at hot junction}} \quad (3)$$

For power generation, the maximum thermoelectric efficiency (η) is defined by combining the Carnot efficiency and the average figure of merit.²

$$\eta_{TE} = \eta_C \frac{(\sqrt{1+ZT_{av}})-1}{(\sqrt{1+ZT_{av}})+\frac{T_{cold}}{T_{hot}}} \quad (4)$$

Where η_C is Carnot efficiency ($\eta_C = (T_{\text{hot}} - T_{\text{cold}})/T_{\text{hot}}$), ZT_{av} is the average figure of merit and T_c and T_h are the cold and hot ends of in a thermoelectric device. As shown in equation 4, for a high thermoelectric efficiency a material needs both high ZT values as well as a high temperature difference around it. Market based thermoelectric devices usually have a $ZT_{\text{av}} \sim 1$ with an efficiency of around 8% which is very much lower than Carnot efficiency (62.5%). By increasing the ZT_{av} by a factor of 4, the efficiency can be increased to around 30% which is an

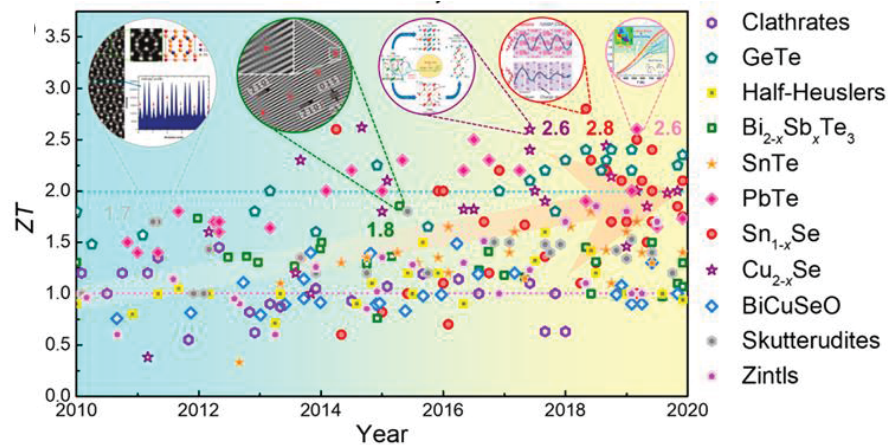


Figure 3. ZT values for state-of-the-art thermoelectric materials in the last decade. (Ref. 2 © 2020, Chem. Rev.)

intriguing prospect.^{2, 3} The reported thermoelectric figure of merit of different materials are shown in figure 3.

1.1.3 Clashing thermoelectric parameters and ways to optimization

As mentioned earlier, a conventional thermoelectric material should have the properties of a metal (high conductivity), a semiconductor (high Seebeck coefficient) and an insulator (low thermal conductivity). The real challenge in the field of thermoelectric is to incorporate all these three properties in one single material. In this section, I will be discussing about some of the conflicting parameters which makes it difficult to incorporate all the three properties in their superior level within a thermoelectric material. I will be also discussing certain methods by the means of which it is possible to decouple the parameters resulting in a superior thermoelectric performance of a material.

1.1.3.1 Conflicting thermoelectric parameters

To obtain a high figure of merit (ZT) in a material, it must have a high σ , high S and low κ . As these transport properties characteristics depend upon interrelated material properties, a number of properties needs to be optimized to amplify ZT .

1.1.3.1.1 Carrier concentration

A material to have a high Seebeck coefficient, it must have only one type of carrier. If both the types of carrier- i.e holes and electrons are present in the system, mixed n-type and p-type conduction (bipolar effect) will take place and both the carrier will move towards the colder end cancelling out the Seebeck voltages and decreasing the thermoelectric performance. One of the materials showing this detrimental effect is $\text{Bi}_{1.1}\text{Sb}_{0.9}\text{Te}_2\text{S}$. Due to the low carrier concentration in insulator and semiconductor, the Seebeck coefficient is high, (Equation 5) however the electrical conductivity is low (Equation 6). Seebeck coefficient is related to n

through the following equation for metals and degenerate semiconductors (single parabolic band and energy-independent scattering approximation)^{11, 12} :

$$S = \frac{8\pi^2 k_B^2}{3eh^2} m^* T \left(\frac{\pi}{3n}\right)^{\frac{2}{3}} \quad (5)$$

Where n is the carrier concentration, m^* is the effective mass of the carrier, h is the Plank's constant and k_B is the Boltzmann constant.

The electrical conductivity varies with n in the following way:

$$\sigma = n\mu e \quad (6)$$

Where μ is the carrier mobility. The carrier mobility on the other hand is inversely proportional to the effective mass ($\mu = (e\tau)/m^*$) where τ is the relaxation time.

The electrical conductivity is directly proportional to the carrier concentration while on the other hand the Seebeck coefficient is inversely proportional to the carrier concentration. Thus,

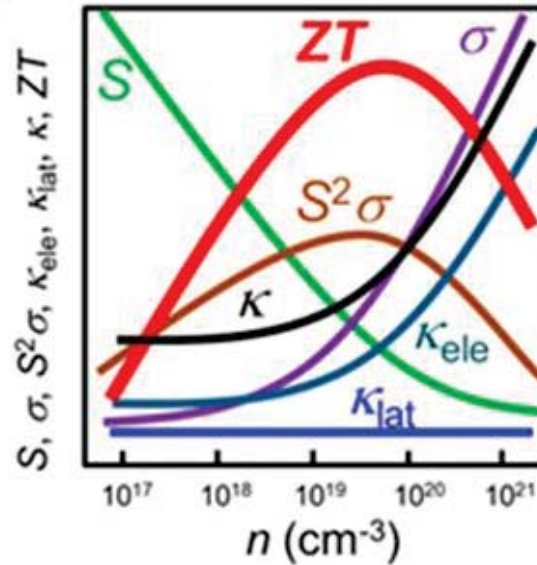


Figure 4. Schematic diagram showing the variation of zT and related TE parameters, electrical conductivity (σ), Seebeck coefficient (S), power factor ($S^2\sigma$), electronic thermal conductivity (κ_{ele}), lattice thermal conductivity (κ_{lat}) and total thermal conductivity (κ), as a function of carrier concentration (n). The TE parameters are highly correlated thereby limiting the maximum zT

the peak value of zT arises in an optimum range of carrier concentration – in the range 10^{19} to 10^{21} cm^{-3} (Figure 4). This range is usually found in semiconductors and heavy-doped semiconductors (degenerate semiconductor)¹³⁻¹⁶.

1.1.3.1.2 Effective mass

The effective mass of the charged carrier provides another squabble in this field as high effective mass provides high Seebeck coefficient as shown in equation 5. The m^* mentioned in this equation refers to the density-of-states effective mass which increases with flat and narrow bands with high DOS at the Fermi surface. However, charge carriers with high effective mass will conduct slowly in the material thus the electrical conductivity will be low. An equilibrium must be found for the effective mass for the dominant charge carrier, forming a compromise between high effective mass and high mobility. The optimum effective mass is still not known. Good thermoelectric materials are found in a wide range of effective mass- high effective mass degenerate semiconductors like oxides and chalcogenides and low effective mass semiconductors like GaAs, SiGe³ etc.

1.1.3.1.3 Electrical thermal conductivity

Thermal conductivity of a material arises from two sources – i) electron and holes carrying heat also known as electrical thermal conductivity (κ_{ele}) and ii) vibration of bonds i.e phonons carrying heat within the system also known as lattice thermal conductivity (κ_{lat}). Here,

$$\kappa_{el} = L \cdot \sigma \cdot T \quad (7)$$

This is the Weidemann-Franz Law where the ratio of the electrical thermal conductivity (κ_{ele}) and electrical conductivity (σ) is directly proportional to temperature and the proportionality constant, L is known as Lorenz factor and for free electrons it has a value of $2.4 \times 10^{-8} \text{ W}\Omega\text{K}^{-2}$. So the problem arises for degenerate semiconductors like SnTe^{17, 18}, GeTe¹⁹⁻²¹ where it has a

high electrical conductivity however the thermoelectric performance of the pristine samples are poor due to large κ_{ele} . The same problem arises from materials having low thermal conductivity like BiSe²², AgSbTe₂²³ etc where the electrical conductivity is low and thus showing poor thermoelectric performance.

1.1.3.1.4 Lattice thermal conductivity

For a material to show good thermoelectric properties, it is preferred that it has a low lattice thermal conductivity. By this logic, glass, a well-known amorphous material should have been an obvious choice. In glass or amorphous material, heat transport is considered a random walk throughout the lattice rather than propagation of phonons and this leads to the concept of minimum thermal conductivity, κ_{min} . However, glasses do not make a good thermoelectric material due to its below-par electrical conductivity, carrier mobility and effective mass. The latter arises due to the presence of broader bands. Thus, a perfect thermoelectric material is a material which can effectively scatter the phonons without significantly interrupting the electrical conductivity. Phonons over a wide wavelength range (1nm to 10 μ m) carries heat and phonon scattering agents of different scale are required to reduce the lattice thermal conductivity. It is suppressed traditionally through a) point defects, b) endotaxial nanoscale precipitates in the host matrix and c) mesoscale grain boundaries. Sometimes all the above three are incorporated in what are referred to as hierarchical architectures where the atomic scale, nanoscale and mesoscale defects would scatter phonons with a broad range of wavelengths²⁴ (Figure 5). The All-scale hierarchical architecting has been shown to be promising especially for the lead chalcogenides. However, in addition to scattering of phonons, an undesirable scattering of carriers can occur limiting the overall zT in most other TE materials.

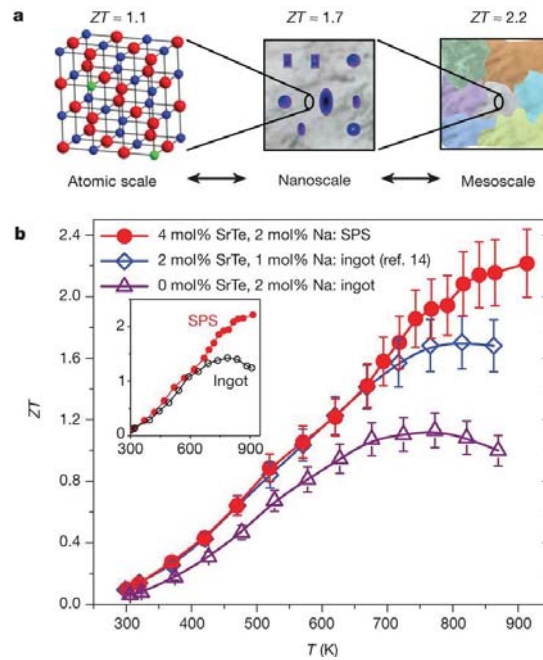


Figure 5. a) Sr doping in PbTe shows all scale hierarchical architectures and thus can scatter phonon in atomic scale, nanoscale and mesoscale which brings about an b) improvement in zT in PbTe. (Ref. 24 © 2012, *Nature*.)

1.1.3.2 Enhancement of power factor

A semiconductor to be a good thermoelectric material it must have a narrow band gap with high carrier mobility as mentioned by Slack *et. al*²⁵. Mahan and his colleagues agreed with Slack's idea and further classified that the narrow band gap of the semiconductors should be equal to or less than $10 K_B T$ (0.25 eV) at 300K with high mobility carriers²⁶. In semiconductors, both Seebeck and electrical coefficient depends on the chemical composition and doping level. These quantities must be perfected to reach an optimised carrier concentration which will maximise the zT .

The unsolved problem in current research is to enhance the thermoelectric power of materials without sacrificing the electrical conductivity and to predict precisely which materials will have high power factor. As mentioned earlier, increase in m^* can bring about an enhancement in the Seebeck coefficient. The well-known approach in this regard is a) formation of resonant levels and b) convergence of valence bands.

1.1.3.2.1 Resonance levels

This approach is to create distortion in the electronic density of states (DOS) near the Fermi energy. Electronic transport properties of semiconductor generally follow the Boltzmann theory. According to this, the Seebeck coefficient strongly depends on energy derivative of carrier density ($n(E)$) and mobility (μ) via Mott relation, in which slight change in DOS can alter the value of Seebeck coefficient.²⁷

$$S = \frac{\pi^2 k_B}{3 q} k_B T \left[\frac{d\{\ln(\sigma(E))\}}{dE} \right]_{E=E_F} \quad (8)$$

$$= \frac{\pi^2 k_B}{3 q} k_B T \left[\frac{1}{n} \frac{d(n(E))}{dE} + \frac{1}{\mu} \frac{d(\mu(E))}{dE} \right]_{E=E_F}$$

Here, $\sigma(E)$ is the electronic conductivity as a function of band filling or Fermi energy, E_F . Here $\sigma(E) = n(E) \cdot e \cdot \mu(E)$ and $n(E) = g(E) \cdot f(E)$ where e is the carrier charge, $\mu(E)$ is the mobility as the function of energy, $f(E)$ is the Fermi function and $g(E)$ is the density of state. When electronic scattering is independent of energy, $\sigma(E)$ is just proportional to the density of states (DOS) at E . Figure 6 shows two hypothetical DOS diagrams where in the first one the DOS varies rapidly near E_F however in the second one the DOS does not change near E_F . Based on the previously stated expression, the system with rapid changing DOS near E_F will show higher Seebeck coefficient. There are reports of Tl doping in PbTe ²⁸ and In doping in SnTe ²⁹ which shows resonant level formation and it arises from the impurity levels near E_F of the semiconductors.

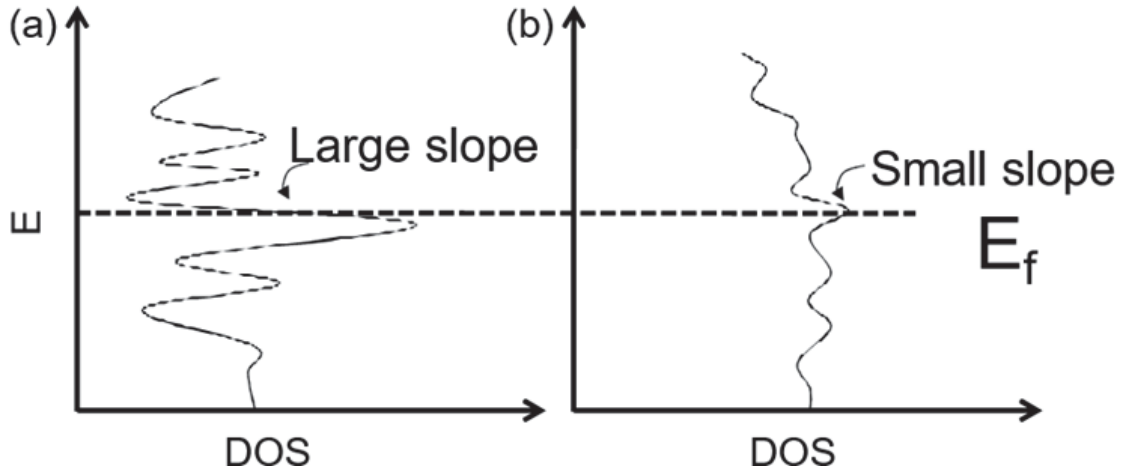


Figure 6 Hypothetical density of state (DOS) with (a) a large slope ($d\ln\sigma(E)/dE$) and (b) a small slope near E_F .

1.1.3.2.2 Valence band convergence

Multiple pockets in valence and conduction band extreme gives rise to high Seebeck coefficient. Multiple degenerate valleys (separate pockets of Fermi surface with the same energy) can be responsible for the increase in the Seebeck coefficient without explicitly increasing the carrier mobility. Hence when the system is heavily doped, more valleys are generated and thus resulting in high power factor. Convergence of multiple charge carrying electronic band valleys is another effective way to increase effective mass.

$$m^* = N_V \cdot m_b^* \quad (9)$$

Here N_V represents orbital degeneracy and m_b^* represents single valley density of state effective mass of degenerate valleys.

Pei et al demonstrated the band convergence of at least 12 valleys in Se doped PbTe alloys leading to an extraordinary high zT of 1.8 at 850K³⁰ as seen in Figure 7. Alloying with Se reduces the energy difference between L and Σ bands of the PbTe making the bands highly converged as a result the N_V increases from 4 to 12 thus amplifying the m^{*30} .

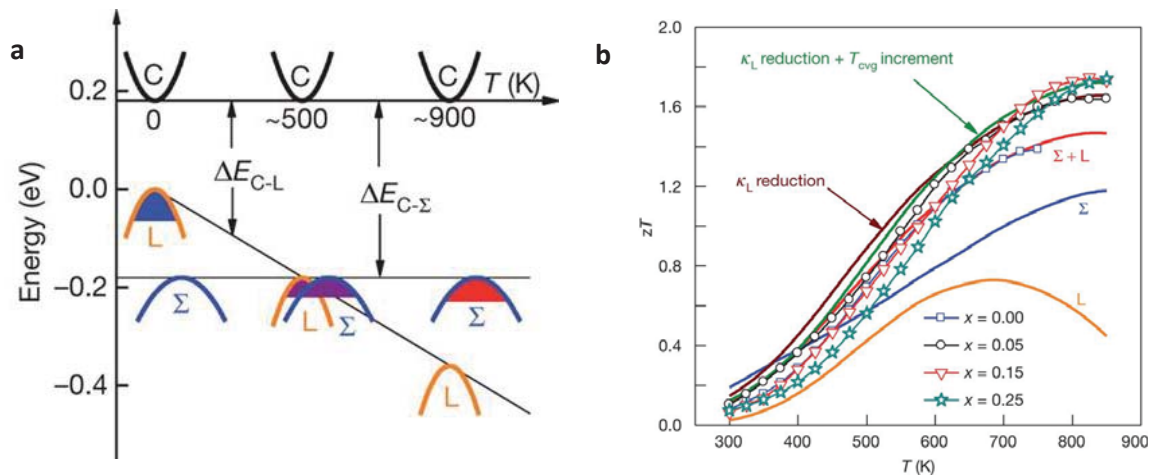


Figure 7. a) Relative energy of the valence bands in PbTe_{0.85}Se_{0.15}. At, 500K two valence bands converge resulting in increase in S b) Temperature dependant zT of PbTe_{1-x}Se_x. (Ref. 30 © 2011, *Nature*.).

1.1.4 Metal chalcogenides based high performance thermoelectric materials

In the past decade and a half, significant progress has been made on high-performance and cost-effective thermoelectric materials. Various approaches have been taken to push the thermoelectric figure of merit towards a value of 3. The approaches include nanostructuring, all-scale hierarchical architecturing, matrix/precipitate band alignment, energy carrier effect, ferroelectric instability effect, resonance level and valence band convergence. Bi₂Te₃ is an effective material which is used for refrigeration for the past four to five decades and was first investigated by H. Julian Goldsmid in 1954. The most commonly used p-type Bi₂Te₃ material is Bi_{0.4}Sb_{1.6}Te₃ whereas Bi₂Te_{2.4}Se_{0.6} is used as a n-type material. For medium temperature power generation, PbTe, GeTe and SnTe are the well-known candidates. On the other hand, for high temperature power generation (used in space shuttles, etc) alloys of germanium and silicon are used in both p-type and n-type legs. Figure 3 shows some of the materials and their high thermoelectric figure of merit obtained in this field of research in the last decade. In this section, I will briefly discuss about one of the champion IV-VI thermoelectric materials that are related to the thesis and their advancement in this field.

1.1.4.1 Germanium telluride

In recent years, plenty of new materials have been identified with satisfactory TE properties. TE materials which are used for mid-temperature (500–800 K) power conversion, are particularly interesting since the major share of the waste heat in industry and automobile exhaust is within this range.³¹ Lead chalcogenides, such as PbTe and other lead chalcogenides has been raised to the peak *via* synergistic effect of band engineering (resonance levels formation, band convergence and bands alignment)³² and nano/microstructure manipulation in all scaled hierarchical architectures²⁴. However, environmental concern about Pb, has slowed down the progress of its mass-market application. Hence, the solid-state chemist and TE community demand discovery of Pb- free high performance TE materials.

In recent years, germanium telluride (GeTe) and its derivatives from IV-VI semiconducting metal chalcogenides family is recently emerging as potential alternative of PbTe. Although GeTe-based thermoelectric is known since 1960,³³ recent years have witnessed tremendous improvement in thermoelectric performance ($zT > 2$) of various GeTe-based materials which is mainly originating from better understanding of its crystal-electronic structure as well as lattice dynamics.³⁴⁻³⁶ In order to gain a better insight into the structure-properties correlation of GeTe, we must understand the nature of chemical bonding, crystal structure and phase transition of GeTe in-details.

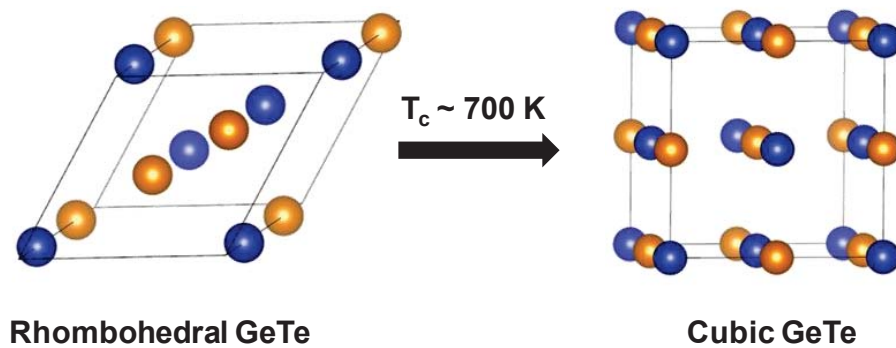


Figure 8. Rhombohedral to a cubic structural phase transition in GeTe (blue and yellow atoms are Ge and Te, respectively).

1.1.4.1.1 Crystal structure

GeTe has rocksalt crystal structure (space group $Fm\bar{3}m$ with a lattice constant of $a = 6.009 \text{ \AA}$, β phase), similar to lead chalcogenides (PbX ; $X = S/Se/Te$) only at high temperature ($>700 \text{ K}$). Below 700 K , GeTe undergoes a structural distortion along $[111]$ direction of cubic structure and adopts rhombohedral structure ($R\bar{3}m$ with the lattice parameters of $a = b = 4.164 \text{ \AA}$ and $c = 10.690 \text{ \AA}$, α phase) (Figure.8). Although similar structural distortion is also observed in semimetal Sb and Bi, GeTe is ferroelectric because of the presence of two different atoms (Ge and Te) with different electronegativity making the bonding polar. At room temperature, the crystal structure of PbTe and SnTe is cubic, whereas GeTe crystallizes in the less symmetric rhombohedral crystal structure. This anomaly mainly governs by the presence of the ns^2 lone pair on the cation.³⁴

The relative displacement of Ge and Te sublattice along the $[111]$ direction make GeTe ferroelectric near room temperature. This distortion changes the angle $\alpha = 88.35^\circ$ from ideal angle of 90° between the axes in the face-centered cubic unit cell.³⁴

1.1.4.1.2 Thermoelectric properties.

Electronic transport.

GeTe is rich with naturally formed and thermodynamically stable Ge-vacancies which drives the system to be intrinsically off-stoichiometric along with naturally occurring Ge precipitations in the matrix.³⁷ These thermodynamically favourable Ge vacancies makes pristine GeTe to be highly p-type with a very high carrier concentration of $\sim 10^{21} \text{ cm}^{-3}$. The high concentration of Ge vacancies results in high electrical conductivity of $\sim 8000 \text{ S/cm}$ and moderate Seebeck coefficient of $\sim 32 \text{ \mu V/K}$ in GeTe at room temperature (Figure 9a).³⁶ Interesting, GeTe exhibits higher S values compared to that of SnTe although both the materials possesses similar carrier concentration. Further, GeTe exhibits exceptionally high-power factor

($\sim 50 \mu\text{W}/\text{cmK}^2$) compared to other TE materials from IV-VI family, especially PbTe ($\sim 30 \mu\text{W}/\text{cmK}^2$) and SnTe ($\sim 20 \mu\text{W}/\text{cmK}^2$) which can be understood by analysing their electronic structure.³⁶

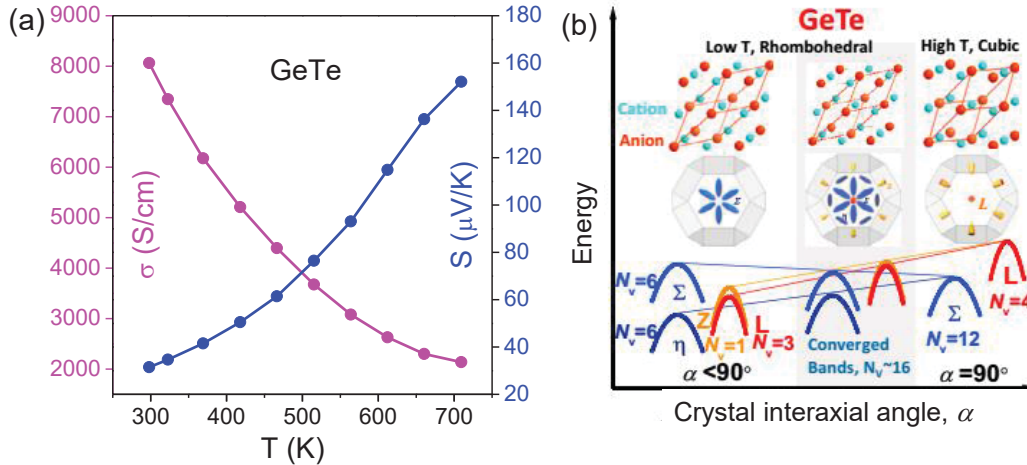


Figure 9. (a) Temperature dependent electrical conductivity and Seebeck Coefficient of GeTe. (b) Schematic energy diagram of the evolution of the electronic structure of GeTe from the rhombohedral phase cubic to depending on interaxial angle. Reproduced from ref 20 ©Elsevier for(b).

Both SnTe and PbTe possess rock-salt NaCl structure ($Fm-3m$) with valence band maxima occurring at L in Brillouin zone. Electronic structure calculations of GeTe have been demonstrated that 8 half-valleys at L band (4 equivalent L band) in cubic GeTe ($Fm-3m$) split into 6 half-valleys at L- point (3 equivalent L band) and 2 half-valleys at Z- point (1 equivalent Z band) in rhombohedral GeTe phase ($R3m$), while 12 full valleys of Σ -band in $Fm-3m$ split into 6 along Σ and rest 6 full valleys along η -line (Figure 9b)²⁰. Notably, valence band maximum at L-point in cubic GeTe shifts to heavy Σ -band in rhombohedral GeTe during phase-transition. As a result, heavier effective mass carriers of Σ -band are dominated in transport properties in rhombohedral GeTe at room temperature, which, in fact, led to the unconventional enhancement in power factor in GeTe, unlike PbTe and SnTe. Further, GeTe has relatively low energy difference ($\sim 0.23 \text{ eV}$) between the heavy hole Σ band and light hole L band, and the energy offset decreases with increasing temperature which results in the increasing contribution of the lower lying valence band in electronic transport.²⁰ A part of my

thesis (**part 2**) is involved understanding structure-property relationship and enhanced the thermoelectric performance of GeTe by using aforementioned strategies and improving its thermoelectric performance.

Thermal conductivity.

Wdowik et al provide clear insight into the lattice dynamics of GeTe (both the phases α & β) together with inelastic neutron scattering experiments and density functional theory calculation.³⁸ To understand the thermal transport of both rhombohedral and cubic GeTe, it is important to examine phonon dispersions of both the phases. Phonon dispersion for α -GeTe at Γ point exhibits six vibrational modes namely 3 acoustic modes, 2 transverse optical modes (TO) and one longitudinal optical mode (LO) (Figure 10a). Both A_1 (non-degenerate) and E (doubly degenerate) modes for rhombohedral GeTe (α -GeTe) are Raman and IR active owing to the absence of inversion symmetry in the structure. Whereas phonon-dispersion of the high-symmetry rocksalt structure of GeTe (β phase) provide the evidence for the presence of several soft phonon modes mainly TO components which are responsible for the symmetry change at the phase transition (Figure 10b).³⁸ Notably, phonon dispersion of cubic GeTe exhibits several imaginary modes in the Brillouin Zone which is the one of the reason for the absence of cubic GeTe at ambient condition, whereas rhombohedral phase exhibits real modes. β phase exhibits local distortions similar to Peierls distortion, which result in three shorter (2.86 Å) and three longer (3.25 Å) Ge-Te bonds.³⁹

GeTe is much more resistant to heat conduction compared to another polycrystalline thermoelectric alloy with a strong mass disorder like InSb (InSb, $\kappa_{\text{lat}} \sim 16$ W/m.K; GeTe, $\kappa_{\text{lat}} \sim 3$ W/m.K, Figure 10c).⁴⁰ Here, chemical bonding plays an important role. Softer bonding in GeTe compared to InSb leads to decrease in the speed of sound and the lattice thermal conductivity. Octahedral coordination in GeTe results in softer bonding compared to that of InSb (tetrahedral bonding) which leads to the decrease in the average sound velocity in GeTe

(1900 m/s) compared to InSb (2300 m/s), thereby lower lattice thermal conductivity in GeTe. Moreover, the strong anharmonic interaction between soft ferroelectric transverse optic mode and longitudinal acoustic modes cause sudden decrease in lattice thermal conductivity of GeTe near the phase transition (Figure 10c).⁴⁰ This soft-phonon mode mediated phase transition temperature can be decreased to room temperature from 700 K through proper doping/alloying,⁴¹ which can bring down the lattice thermal conductivity of GeTe to its minimum value ($\kappa_{\text{min}} \sim 0.3$ W/mK), thus can improve thermoelectric performance of GeTe near room temperature. κ_{lat} of GeTe can be further decreased by employing convention strategies like alloying and nanostructuring in order to improve its TE performance.^{34, 36}

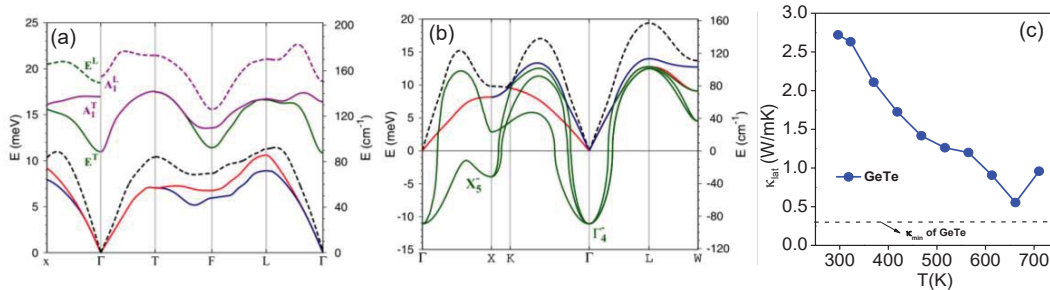


Figure 10. Phonon dispersion plot of (a) rhombohedral and (b) cubic GeTe. Solid and dashed lines represent transverse (T) and longitudinal (L) modes, respectively. (c) Temperature dependent lattice thermal conductivity of GeTe showing sudden drop near the phase transition. Reproduced from ref 38 ©American Physical Society for (a, b).

1.1.5 Summary

In this chapter, I have discussed the basics of thermoelectric effect, how heat is transported in crystalline solid and lastly some metal chalcogenide based thermoelectric materials. The figure of merit has seen a huge amplification in the past decade through different techniques discussed earlier and it has reached a value of ~ 1.8 - 2.8 at 700-900 K. To cross this value, we need to either significantly increase the power factor or reduce the thermal conductivity (preferably the κ_{lat} to its amorphous limit). In the following chapters (Part 2: Chapter 1 & 2), I will be discussing certain strategies which brings about an increase in the thermoelectric figure of merit

of GeTe based thermoelectric material and I will discuss how those materials can be utilized in power generation application via device fabrication.

1.1.6 References:

1. Tan, G.; Zhao, L.-D.; Kanatzidis, M. G., Rationally designing high-performance bulk thermoelectric materials. *Chem. Rev.* **2016**, *116* (19), 12123-12149.
2. Shi, X.-L.; Zou, J.; Chen, Z.-G., Advanced Thermoelectric Design: From Materials and Structures to Devices. *Chem. Rev.* **2020**, *120* (15), 7399-7515.
3. Xiao, Y.; Zhao, L.-D., Seeking new, highly effective thermoelectrics. *Science* **2020**, *367* (6483), 1196.
4. Forman, C.; Muritala, I. K.; Pardemann, R.; Meyer, B., Estimating the global waste heat potential. *Renew. Sust. Energ. Rev.* **2016**, *57*, 1568-1579.
5. Rowe, D. M., Applications of nuclear-powered thermoelectric generators in space. *Appl. Energy.* **1991**, *40* (4), 241-271.
6. Bennett, G. L.; Skrabek, E. A. In *Power performance of US space radioisotope thermoelectric generators*, Fifteenth International Conference on Thermoelectrics. Proceedings ICT '96, 26-29 March 1996; 1996; pp 357-372.
7. Moulif, N.; Divay, A.; Joubert, E.; Latry, O., 8 - Reliability Study of High-Power Mechatronic Components by Spectral Photoemission Microscopy. In *Reliability of High-Power Mechatronic Systems 2*, El Hami, A.; Delaux, D.; Grzeskowiak, H., Eds. Elsevier: 2017; pp 241-271.
8. Seebeck, T. J., Ueber die magnetische Polarisierung der Metalle und Erze durch Temperaturdifferenz. *A. Ann. Chim. Phys.* **1826**, *82* (3), 253-286.
9. Drebuschak, V. A., The Peltier effect. *J. Therm. Anal. Calorim* **2007**, *91* (1), 311.
10. Zhao, L.-D.; Dravid, V. P.; Kanatzidis, M. G., The panoscopic approach to high performance thermoelectrics. *Energy Environ. Sci.* **2014**, *7* (1), 251-268.
11. Snyder, G. J.; Toberer, E. S., Complex thermoelectric materials. *Nat. Mater.* **2008**, *7* (2), 105-114.
12. Sootsman, J. R.; Chung, D. Y.; Kanatzidis, M. G., New and old concepts in thermoelectric materials. *Angew Chem Int Ed* **2009**, *48* (46), 8616-8639.
13. Wang, S.; Xiao, Y.; Chen, Y.; Peng, S.; Wang, D.; Hong, T.; Yang, Z.; Sun, Y.; Gao, X.; Zhao, L.-D., Hierarchical structures lead to high thermoelectric performance in $\text{Cu}_{m+n}\text{Pb}_{100}\text{Sb}_m\text{Te}_{100}\text{Se}_{2m}$ (CLAST). *Energy Environ. Sci.* **2021**, *14* (1), 451-461.
14. Wu, H.; Zhao, L.-D.; Zheng, F.; Wu, D.; Pei, Y.; Tong, X.; Kanatzidis, M. G.; He, J., Broad temperature plateau for thermoelectric figure of merit $ZT > 2$ in phase-separated $\text{PbTe}_{0.7}\text{S}_{0.3}$. *Nat. Commun.* **2014**, *5* (1), 1-9.
15. Moshwan, R.; Yang, L.; Zou, J.; Chen, Z.-G., Eco-Friendly SnTe Thermoelectric Materials: Progress and Future Challenges. *Adv. Funct. Mater.* **2017**, *27* (43), 1703278.

16. Zhang, X.; Bu, Z.; Lin, S.; Chen, Z.; Li, W.; Pei, Y., GeTe Thermoelectrics. *Joule* **2020**, *4* (5), 986-1003.
17. Sarkar, D.; Ghosh, T.; Banik, A.; Roychowdhury, S.; Sanyal, D.; Biswas, K., Highly Converged Valence Bands and Ultralow Lattice Thermal Conductivity for High-Performance SnTe Thermoelectrics. *Angew. Chem. Int. Ed.* **2020**, *59* (27), 11115-11122.
18. Banik, A.; Ghosh, T.; Arora, R.; Dutta, M.; Pandey, J.; Acharya, S.; Soni, A.; Waghmare, U. V.; Biswas, K., Engineering ferroelectric instability to achieve ultralow thermal conductivity and high thermoelectric performance in $\text{Sn}_{1-x}\text{Ge}_x\text{Te}$. *Energy Environ. Sci.* **2019**, *12* (2), 589-595.
19. Samanta, M.; Biswas, K., Low Thermal Conductivity and High Thermoelectric Performance in $(\text{GeTe})_{1-2x}(\text{GeSe})_x(\text{GeS})_x$: Competition between Solid Solution and Phase Separation. *J. Am. Chem. Soc.* **2017**, *139* (27), 9382-9391.
20. Li, J.; Zhang, X.; Chen, Z.; Lin, S.; Li, W.; Shen, J.; Witting, I. T.; Faghaninia, A.; Chen, Y.; Jain, A., Low-symmetry rhombohedral GeTe thermoelectrics. *Joule* **2018**, *2* (5), 976-987.
21. Acharyya, P.; Roychowdhury, S.; Samanta, M.; Biswas, K., Ultralow Thermal Conductivity, Enhanced Mechanical Stability, and High Thermoelectric Performance in $(\text{GeTe})_{1-2x}(\text{SnSe})_x(\text{SnS})_x$. *J. Am. Chem. Soc.* **2020**.
22. Samanta, M.; Pal, K.; Pal, P.; Waghmare, U. V.; Biswas, K., Localized Vibrations of Bi Bilayer Leading to Ultralow Lattice Thermal Conductivity and High Thermoelectric Performance in Weak Topological Insulator n-Type BiSe. *J. Am. Chem. Soc.* **2018**, *140* (17), 5866-5872.
23. Roychowdhury, S.; Ghosh, T.; Arora, R.; Samanta, M.; Xie, L.; Singh, N. K.; Soni, A.; He, J.; Waghmare, U. V.; Biswas, K., Enhanced atomic ordering leads to high thermoelectric performance in AgSbTe_2 . *Science* **2021**, *371* (6530), 722.
24. Biswas, K.; He, J.; Blum, I. D.; Wu, C.-I.; Hogan, T. P.; Seidman, D. N.; Dravid, V. P.; Kanatzidis, M. G., High-performance bulk thermoelectrics with all-scale hierarchical architectures. *Nature* **2012**, *489* (7416), 414-418.
25. Slack, G. A. In *Design concepts for improved thermoelectric materials*, Materials research society symposium proceedings, Materials Research Society: 1997; pp 47-54.
26. Mahan, G.; Sales, B.; Sharp, J., Thermoelectric Materials: New Approaches to an Old Problem. *J. Phys. Today.* **1997**, *50* (3), 42-47.
27. Heremans, J. P.; Wiendlocha, B.; Chamoire, A. M., Resonant levels in bulk thermoelectric semiconductors. *Energy Environ. Sci.* **2012**, *5* (2), 5510-5530.
28. Heremans, J. P.; Jovovic, V.; Toberer, E. S.; Saramat, A.; Kurosaki, K.; Charoenphakdee, A.; Yamanaka, S.; Snyder, G. J., Enhancement of Thermoelectric Efficiency in PbTe by Distortion of the Electronic Density of States. *Science* **2008**, *321* (5888), 554.

29. Zhang, Q.; Liao, B.; Lan, Y.; Lukas, K.; Liu, W.; Esfarjani, K.; Opeil, C.; Broido, D.; Chen, G.; Ren, Z., High thermoelectric performance by resonant dopant indium in nanostructured SnTe. *Proc. Natl. Acad. Sci.* **2013**, *110* (33), 13261-13266.
30. Pei, Y.; Shi, X.; LaLonde, A.; Wang, H.; Chen, L.; Snyder, G. J., Convergence of electronic bands for high performance bulk thermoelectrics. *Nature* **2011**, *473* (7345), 66-69.
31. Yang, J.; Caillat, T., Thermoelectric materials for space and automotive power generation. *MRS bulletin* **2006**, *31* (3), 224-229.
32. Heremans, J. P.; Jovovic, V.; Toberer, E. S.; Saramat, A.; Kurosaki, K.; Charoenphakdee, A.; Yamanaka, S.; Snyder, G. J., Enhancement of thermoelectric efficiency in PbTe by distortion of the electronic density of states. *Science* **2008**, *321* (5888), 554-557.
33. Rosi, F.; Dismukes, J.; Hockings, E., Semiconductor materials for thermoelectric power generation up to 700 C. *Electr. Eng.* **1960**, *79* (6), 450-459.
34. Roychowdhury, S.; Samanta, M.; Perumal, S.; Biswas, K., Germanium chalcogenide thermoelectrics: electronic structure modulation and low lattice thermal conductivity. *Chem. Mater.* **2018**, *30* (17), 5799-5813.
35. Duan, S.; Xue, W.; Yao, H.; Wang, X.; Wang, C.; Li, S.; Zhang, Z.; Yin, L.; Bao, X.; Huang, L., Achieving High Thermoelectric Performance by NaSbTe₂ Alloying in GeTe for Simultaneous Suppression of Ge Vacancies and Band Tailoring. *Adv. Energy Mater.* **2022**, *12* (3), 2103385.
36. Perumal, S.; Roychowdhury, S.; Biswas, K., High performance thermoelectric materials and devices based on GeTe. *J. Mater. Chem. C* **2016**, *4* (32), 7520-7536.
37. Zhang, X.; Li, J.; Wang, X.; Chen, Z.; Mao, J.; Chen, Y.; Pei, Y., Vacancy manipulation for thermoelectric enhancements in GeTe alloys. *J. Am. Chem. Soc.* **2018**, *140* (46), 15883-15888.
38. Wdowik, U. D.; Parlinski, K.; Rols, S.; Chatterji, T., Soft-phonon mediated structural phase transition in GeTe. *Phys. Rev. B* **2014**, *89* (22), 224306.
39. Sun, Z.; Zhou, J.; Mao, H.-K.; Ahuja, R., Peierls distortion mediated reversible phase transition in GeTe under pressure. *Proc. Natl. Acad. Sci.* **2012**, *109* (16), 5948-5952.
40. Lee, S.; Esfarjani, K.; Luo, T.; Zhou, J.; Tian, Z.; Chen, G., Resonant bonding leads to low lattice thermal conductivity. *Nat. Commun.* **2014**, *5* (1), 1-8.
41. Liu, Z.; Sun, J.; Mao, J.; Zhu, H.; Ren, W.; Zhou, J.; Wang, Z.; Singh, D. J.; Sui, J.; Chu, C.-W., Phase-transition temperature suppression to achieve cubic GeTe and high thermoelectric performance by Bi and Mn codoping. *Proc. Natl. Acad. Sci.* **2018**, *115* (21), 5332-5337.

Chapter 1.2

A Brief Introduction to Intercalation and Ion-Exchange Reactions

Chapter 1.2

A BRIEF INTRODUCTION TO INTERCALATION AND ION-EXCHANGE REACTIONS

1.2.1 Layered inorganic solids and intercalation chemistry.

Bulk layered materials have been studied extensively in the past several decades because of their unique structural features, and physical and chemical properties.¹ Materials with layered structures remain an extensively investigated subject in current chemistry and physics due to their interesting properties. The rich family of layered materials consists of single- element crystals, such as graphite, phosphorus, arsenic, antimony and bismuth, silicates, hydroxides, transition metal chalcogenides and many oxides.^{2, 3} The valuable properties of layered inorganic solids and the possibility of modification by various post-synthesis treatments have attracted a lot of attention for many years. Layered materials typically exhibit strong in-plane covalent bonding and weak out-of-plane van der Waals interactions through the interlayer gap.⁴ They exhibit a wide range of electronic band structures from insulators, semiconductors, metals, superconductors to topological insulators.⁴ Hence, layered phases present new physical and chemical properties that are not commonly encountered in three- dimensional materials.⁵⁻⁷ Many of these properties are strongly related to nature and extent of interactions between the layers, hence reflects the type of behavior which falls between two and three dimensional systems.⁸ Research into the basic science of layered solids has intensified in the last decade due to a number of emerging applications in catalysis, adsorption, photovoltaics and medicine.⁹ Most of the promising technological applications, however, deal with intercalation compounds of layered inorganic solids. These intercalated materials have various applications, for instance as catalysts, sorbents, ion-exchange,

electrochromic displays, electrodes for secondary batteries (Li-ion batteries) and components for fuel cells.⁸ Intercalation is a solid-state reaction which involves the chemical or thermal reversible inclusion or insertion of a guest species (ion or molecule) into a layered inorganic solid host. The structure of the host remains unchanged or is only slightly altered in the guest-host complex (intercalate). The reaction does not involve diffusive rearrangement of host and therefore is considered to be a topotactic reaction.⁸ A wide variety of intercalated structures can form including ordered vacancy compound because of the specificity of the interactions between the guest atoms and host lattice. Table 1 describes insulating host lattices and redox- active host lattices. The reversible ion-electron transfer reaction is described as

$x\text{A}^+ + xe^- + [\text{Host}] \rightleftharpoons \text{A}_x^+[\text{Host}]^{x-}$ where A is an alkali metal and x is the molar intercalation fraction.

Table 1 Two-dimensional host lattices for intercalation.

Insulating host lattices	Redox-active host lattices
Clays and layered silicates Kaolinite $\text{Al}_2\text{Si}_2\text{O}_5(\text{OH})_4$	Graphite Dichalcogenides MX_2 (M = Ti, Zr, Hf, V, Nb, Ta, Mo, W; X = S, Se, Te)
Hectorite $\text{Na}_x(\text{Mg}_{3-x}\text{Li}_x)\text{Si}_4\text{O}_{10}(\text{OH})_2 \cdot m\text{H}_2\text{O}$	Metal phosphorus trichalcogenides MPX_3 (M = Mg, V, Mn, Fe, Co, Ni, Zn, Cd, In; X = S, Se)
Montmorillonite $\text{Na}_x(\text{Al}_{2-x}\text{Mg}_x)\text{Si}_4\text{O}_{10}(\text{OH})_2 \cdot m\text{H}_2\text{O}$	Metal oxyhalides MOX (M = Ti, V, Cr, Fe; X = Cl, Br)
Niobates and tantalates $\text{K}[\text{Ca}_2\text{Na}_{n-3}\text{Nb}_n\text{O}_{3n+1}]$, $3 \leq n \leq 7$; $\text{K}_2\text{Ti}_4\text{O}_9$, KTiNbO_3	Metal Nitride Halides MNX (M = Zr, Hf; X = Cl, Br, I)
Hydrous oxides $\text{A}_x\text{UO}_2\text{XO}_4 \cdot m\text{H}_2\text{O}$	Ternary chalcogenides AMX_2 (A = Group 1; M = Ti, V, Cr, Mn, Fe, Co, Ni; X = O, S)
Layered double hydroxides $\text{LiAl}_2(\text{OH})_6\text{OH} \cdot 2\text{H}_2\text{O}$, $\text{Zn}_2\text{Cr}(\text{OH})_6\text{Cl} \cdot 2\text{H}_2\text{O}$	
Acid phosphates $\text{M}(\text{HPO}_4)_2 \cdot \text{H}_2\text{O}$; M = Ti, Zr, Hf, Ce, Sn, $\text{Ni}(\text{CN})_2$	MOXO_4 (M = V, Nb, Ta, Mo; X = P, As), MoO_3 ; V_2O_5

1.2.1.1 Intercalation reactions.

During intercalation two main effects take place. One is a change of preferential crystallographic parameters without destruction of the original structure and other is the charge transfer which can affect the electronic properties of host strongly. It is believed that the driving force for intercalation reaction comes from the tendency for charge transfer. The charge transfer takes place from the guest to the host layered compound's conduction band; thus electron-donating species can act generally as guest. The host spans the range of electronic conductivity from insulators such as MoO_3 , clays, zeolites through semiconductors such as graphite and transition metal dichalcogenides to metallic nature such as LaNi_5 .⁵

Both kinetics and thermodynamics play crucial role in the formation of these intercalated compounds. During a reaction, expansion of host lattice takes place due to nucleation of a new phase which is followed by diffusion of guest species into host lattice. Staging helps to minimize the energy required for expansion. Staging phenomenon is observed only in layered compounds. When an odd number of stages are found, it appears that in going from one stage to other an entire layer of guest should exit and re-intercalate (Figure 1). Lower guest concentration leads to higher stages.⁶

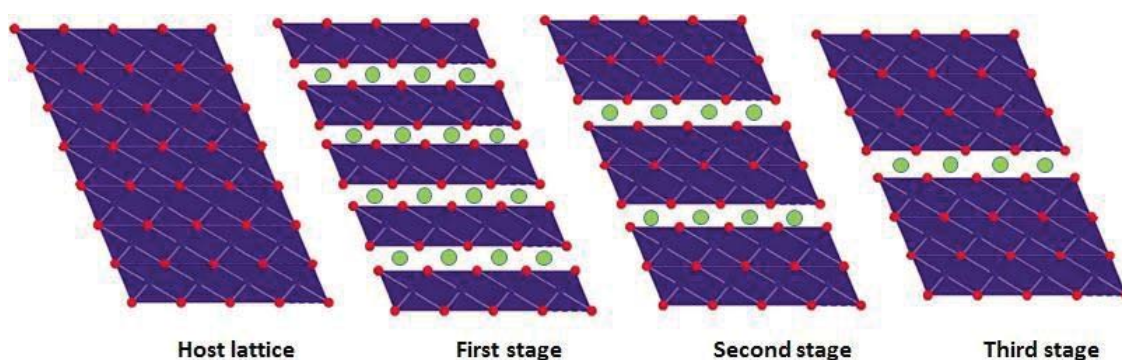


Figure 1 Schematic representation of different staging in intercalation compounds. Guest molecules are green spheres.

1.2.1.2 Insulating 2D host lattices for intercalation.

Clay minerals.

The sheet silicate or clay minerals constitute the largest group in insulating 2D host lattices for intercalation. Clay minerals have structures comprising complex layers made by condensing two types of sub layers. In one type, silicon is tetrahedrally coordinated, $\text{Si}_2\text{O}_3(\text{OH})_2$, and in the other aluminum is octahedral, $\text{Al}(\text{OH})_6$. The sub layers are connected to produce two different structure types that are illustrated by kaolinite, which has the ideal composition $\text{Al}_2\text{Si}_2\text{O}_5(\text{OH})_4$ and contains one octahedral and one tetrahedral layer (1:1), and pyrophyllite, $\text{Al}_2(\text{Si}_4\text{O}_{10})(\text{OH})_2$, which has one octahedral and two tetrahedral layers (2:1) (see Figure 2). Compounds are also known in which three Mg^{2+} cations replace two Al^{3+} cations to give serpentine, $\text{Mg}_3\text{Si}_2\text{O}_5(\text{OH})_4$, or talc, $\text{Mg}_3(\text{Si}_4\text{O}_{10})(\text{OH})_2$. Kaolinite forms intercalation compounds with urea, formamide, acetamide and hydrazine via hydrogen bonding.^{10, 11} Exceptional mechanical properties have been reported for clay-polymer intercalated nano- composites formed between organo-cation exchanged montmorillonites and nylon-6.¹²⁻¹⁴ Inorganic pillared clays have also been studied by inserting poly-oxocation like $[\text{Al}_{13}\text{O}_4(\text{OH})_{24}\cdot 12\text{H}_2\text{O}]^{7+}$ into the inter-lamellar space to separate the layers and form stable pillared clay.¹⁵

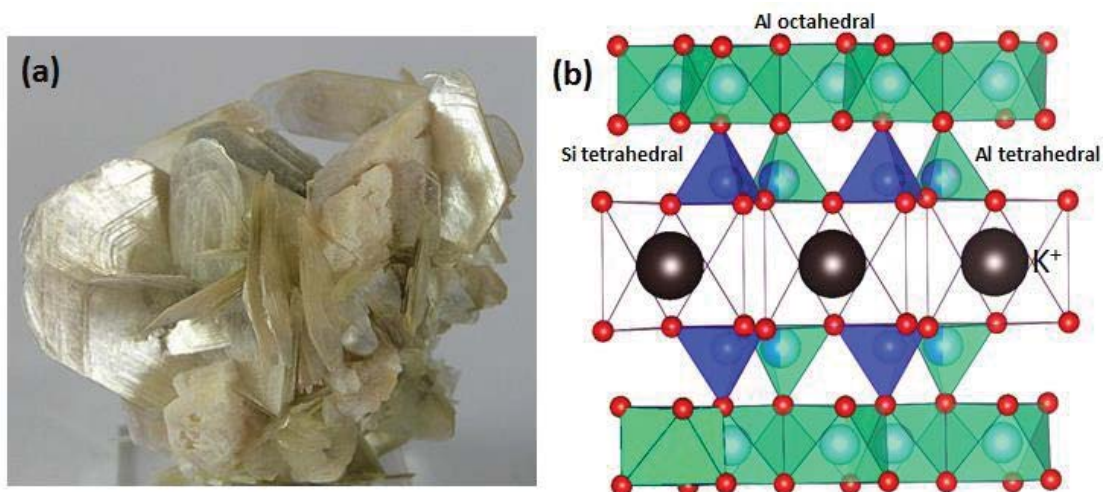


Figure 2 (a) Muscovite ($\text{KAl}_2(\text{Si}_3\text{AlO}_{10})(\text{OH})_2$) and (b) Structure of Muscovite, where red and black are oxygen and potassium. Potassium is intercalated between the layers of pyrophyllite ($\text{Al}_2(\text{Si}_4\text{O}_{10})(\text{OH})_2$).

Layered double hydroxides (LDH).

The layered double hydroxides are derived by partial substitution of a trivalent cation for a divalent cation in a hydroxide with the $\text{Mg}(\text{OH})_2$ brucite structure. Substitution results by the formula

$\text{M}_{1-x}\text{M}'_x(\text{OH})_2 \cdot \text{A}_{x/n} \cdot m\text{H}_2\text{O}$, where A is the solvated interlayer anion, $\text{M}^{2+} = \text{Mg}, \text{Zn}, \text{Fe}, \text{or Co}$ and

$\text{M}^{3+} = \text{Cr}, \text{Al}, \text{Mn}, \text{or Fe}$. The natural mineral hydrotalcite, $\text{Mg}_6\text{Al}_2(\text{OH})_{16}\text{CO}_3 \cdot 4\text{H}_2\text{O}$ is a best-known example with carbonate as guest species (see Figure 3).^{16, 17} The specific interlayer anion is

determined by synthesis method, but it can easily be exchanged after the compound is formed. LDHs can intercalate organic anions like n-alkanols, n-alkylamines, aliphatic carboxylates.¹⁸ LDHs have been used as anion exchangers, basic catalysts and catalyst precursors.

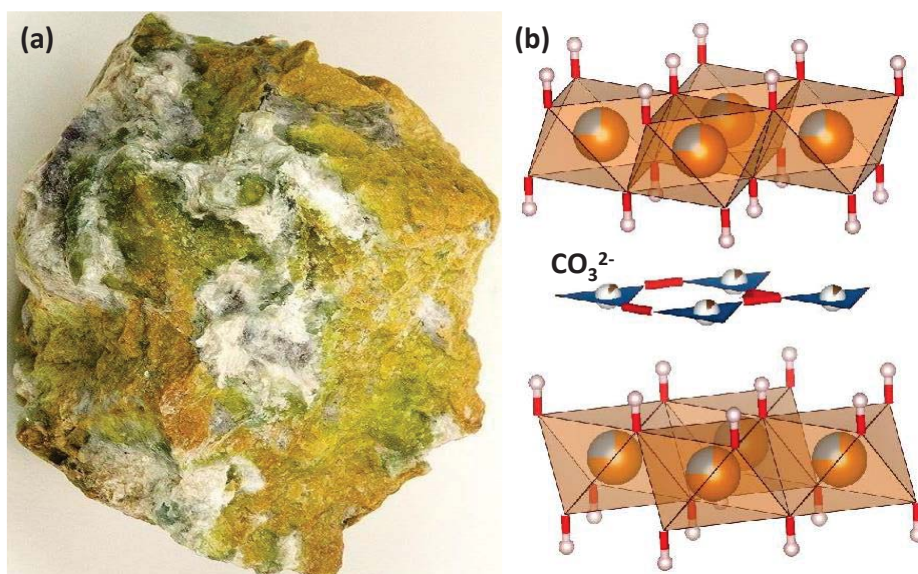


Figure 3 (a) Hydrotalcite ($\text{Mg}_6\text{Al}_2(\text{OH})_{16}\text{CO}_3 \cdot 4\text{H}_2\text{O}$) with serpentine ($\text{Mg}_3(\text{Si}_4\text{O}_{10})(\text{OH})_2$) and (b) The structure of Hydrotalcite. Carbonate is intercalated between the layers of substituted trivalent Al^{3+} $\text{Mg}(\text{OH})_2$.

1.2.1.3 Redox active 2D host lattices for intercalation.

Graphite.

The first intercalated, graphite sulphate, was reported by Schaufault in 1841.¹⁹ Graphite is well-

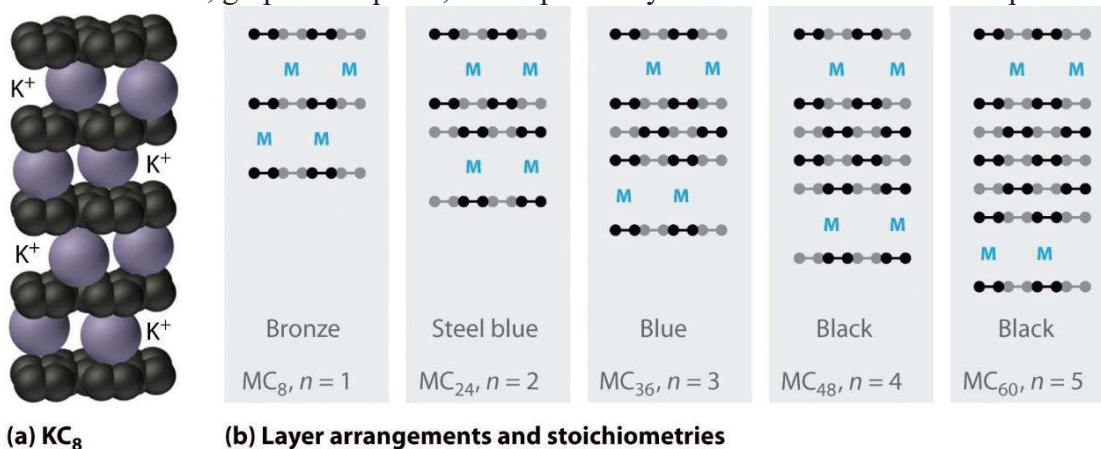


Figure 4 (a) Layers of K^+ ions are inserted between every pair of carbon layers, giving $n=1$ and (b) The stoichiometry and color of intercalation compounds depend on the number of layers of carbon atoms (n) between each layer of intercalated metal atoms.

known host which intercalates a variety of guest molecules which can be electron donors or acceptors. Alkali and alkaline earth metals, act as donors, results in cation-size dependent

expansion of the separation between the adjacent carbon planes.⁶ The stoichiometry MC_8 is observed for $M = K, Rb$ and Cs and MC_6 for smaller ions $M = Li^+, Sr^{2+}, Ba^{2+}, Eu^{2+}, Yb^{3+}$ and Ca^{2+} .⁵

Figure 4 shows the general layer arrangements and stoichiometries of intercalation compounds.



Graphite acts as electron donor when the intercalated guest species are electron acceptors such as $\text{HSO}_4, \text{NO}_3, \text{CrO}_2\text{Cl}_2, \text{CrO}_3, \text{Br}_2$ and metal halides like $\text{MoF}_6, \text{FeCl}_3$.⁵



1.2.2 Ion-exchange reactions.

Ion-exchange is a chemical reaction in which intercalated ions of a compound with open- network or layered structure are exchanged with different ions contained in a medium with which it is in contact. Certain inorganic materials can react with ionic solutions to selectively remove one ionic component and replace it with other ions from the solution, with the end result being new materials. Ion-exchangers are insoluble solid materials with exchangeable cations or anions. When ion-exchanger is in contact with an electrolyte solution, stoichiometrically equivalent amount of other ions of same sign can be exchanged.²⁰



The ion-exchange process, based on topotactic reactions, can result in a material crystallographically analogous to the parent phase but with a new chemical composition.

1.2.2.1 Mechanism of ion-exchange reactions.

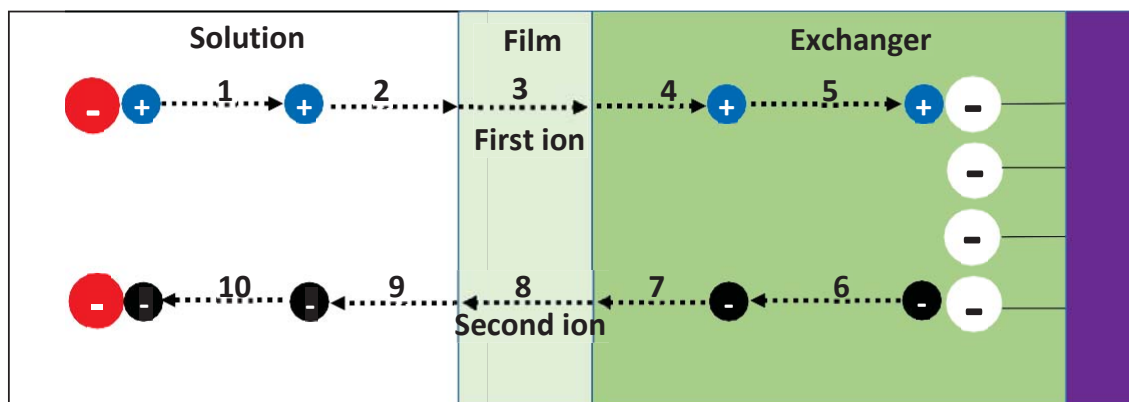


Figure 5 Mechanism of the ion-exchange process. (1) dissociation of the dissolved complexes containing first ion; (2) diffusion of the first ion from solution towards the inter-phase film; (3) diffusion of the first ion through the inter-phase film; (4) diffusion of the first ion inside the material phase; (5) association between the first ion and functional group; (6) dissociation of the associates between the second ion and functional group; (7) diffusion of the second ion inside the material phase towards the surface; (8) diffusion of the second ion through the interphase film; (9) diffusion and random distribution of the second ion in the solution; (10) formation of the second ion complexes in the solution.

Ion-exchange is an adsorption phenomenon where the mechanism of adsorption is electrostatic.

Electrostatic forces hold ions to charged functional groups on the surface of the ion-exchanger.

The adsorbed ions replace ions that are on the surface of ion-exchanger on a 1:1 charge basis.

England *et al.* revealed that ion-exchange occurs even when the diffusion coefficients are as small as $\sim 10^{-12}$ cm²/s.²⁰ Figure 5 explains the general mechanism of ion exchange reactions. Ion-exchange occurs at considerable rates in stoichiometric solid topochemically which enables the synthesis of metastable phases that are inaccessible by high-temperature reactions.¹¹

1.2.2.2 Ion-exchange reactions of layered inorganic solids.

Inorganic layered solids can react with ionic solutions to selectively remove one ionic component and replace it with other ions from the solution. For example, the ion-exchange reaction of Na₂Si₂O₅ with molten AgNO₃ produces a sheet silicate structure type Ag₂Si₂O₅.⁶ The α -NaCrO₂ type framework of α -LiFeO₂ changes to delafossite (A⁺B³⁺O₂; A=Ag, Cu, B=Fe, Ni, etc) when it

is converted to CuFeO_2 by exchange with molten CuCl to provide linear anion coordination for Cu^+ .⁹

Metal sulfides with layered anionic structure and intercalated cations constitute the well-studied class of ion-exchange reactions. They show excellent and selective ion-exchange property due to facile diffusion of the cations as they are able to access the internal surface of the metal sulfides and form strong bonds between the incorporated metal ions and S^{2-} ligands.²¹

KMS materials.

$\text{K}_{2x}\text{M}_x\text{Sn}_{3-x}\text{S}_6$ (KMS) compounds, reported by M. G. Kanatzidis and coworkers are derivatives of SnS_2 with partial substitution of Sn^{4+} by M^{2+} ($\text{M} = \text{Mn}^{2+}$ or Mg^{2+}) ions.^{22, 23} These materials have

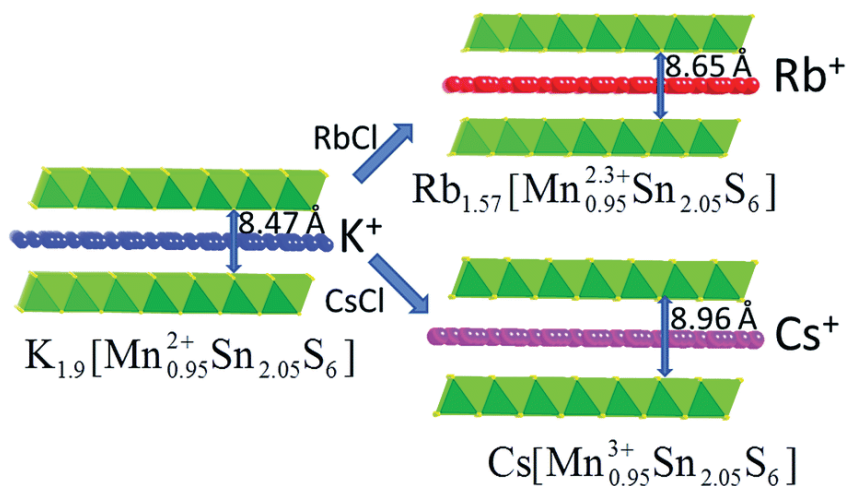


Figure 6 Representations of the crystal structures of KMS-1 and its Rb^+ and Cs^+ -exchanged analogs and the interlayer spacing. M. G. Kanatzidis, *Chem. Sci.*, **2016**, 7, 4804 © Royal Society of Chemistry.

general formula $\text{K}_{2x}\text{M}_x\text{Sn}_{3-x}\text{S}_6$ ($\text{M} = \text{Mn}^{2+}$, KMS-1; $\text{M} = \text{Mg}^{2+}$, KMS-2; $x = 0.5-1$), where interlayer spacing is filled with K^+ ions can be exchanged with radioactive Cs^+ , Sr^{2+} , Ni^{2+} and UO^{2+}

and cations like Rb^+ , Hg^{2+} , Pb^{2+} , Cd^{2+} , Ag^+ , Hg^{2+} and Cu^{2+} . The Figure 6 describes the representation of ion-exchange in KMS-1 by Rb^+ and Cs^+ .

LHMS material.

When KMS-1 is treated with strongly acidic solutions, hydronium ions replace potassium ions and

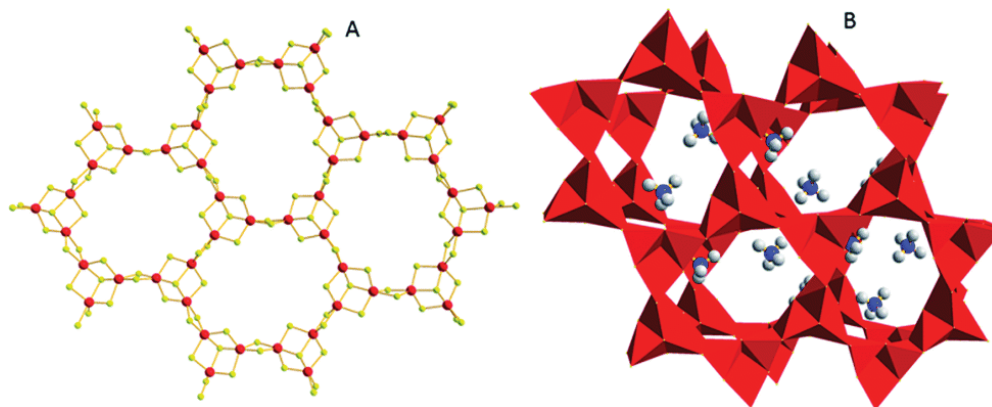


Figure 7 (a) The structure of $(\text{TMA})_2(\text{Sn}_3\text{S}_7) \cdot \text{H}_2\text{O}$ (Sn, red; S, yellow). (b) The arrangement of two adjacent layers (with a polyhedral representation) and the TMA^+ cations (C, grey; N, blue) located in the interlayer space (guest water molecules were omitted for clarity). M. G. Kanatzidis, *Chem. Sci.*, **2016**, 7, 4804 © Royal Society of Chemistry.

forms layered hydrogen metal sulfide compound (LHMS-1) with general formula $\text{H}_{2x}\text{Mn}_x\text{Sn}_{3-x}\text{S}_6$ ($x=0.11-0.25$).²⁴ LHMS-1 has achieved almost 100% Hg^{2+} removal under extremely acidic solutions which can be useful for removing Hg^{2+} from acid wastewater.

Materials based on the $\text{Sn}_3\text{S}_7^{2-}$ network.

J. B. Praise and coworkers reported the first compound based on $\text{Sn}_3\text{S}_7^{2-}$, $(\text{TMA})_2(\text{Sn}_3\text{S}_7) \cdot \text{H}_2\text{O}$ (TMA^+ =tetramethylammonium ion).²⁵ Figure 7 shows microporous framework consisting of edge-sharing Sn_3S_4 semi cubes connected by twelve SnS_5 trigonal bipyramids, where TMA^+ and guest water species present between the layers can be exchanged with Ag^+ . Recently, FJSM-SnS, $(\text{Me}_2\text{NH}_2)_{4/3}(\text{Me}_3\text{NH})_{2/3}\text{Sn}_3\text{S}_7 \cdot 1.25\text{H}_2\text{O}$ reported by X. H. Qi *et. al.* has proven to be effective ion-exchanger for Cs^+ and Sr^{2+} .²⁶

KTS materials.

Tin sulfide layered material, $\text{K}_2\text{Sn}_4\text{S}_9$ (KTS-1) consists of $\text{Sn}_4\text{S}_9^{2-}$ cluster connected through S^{2-}

bridges to form the layered structure perforated with large holes and the interlayer space is filled with highly disordered cations (see figure 8).²⁷ K^+ ion of KTS-1 has been exchanged with Cs^+ and heavy metal ions like Hg^{2+} , Pb^{2+} and Cd^{2+} . KTS-3 ($\text{K}_{2x}\text{Sn}_{4-x}\text{S}_{8-x}$) with SnS_6 octahedra are connected with SnS_4 units and the interlayer space is filled with disordered K^+ ions. KTS-3 has been found as an excellent ion-exchanger for Cs^+ , Sr^{2+} and UO_2^{2+} .²⁸

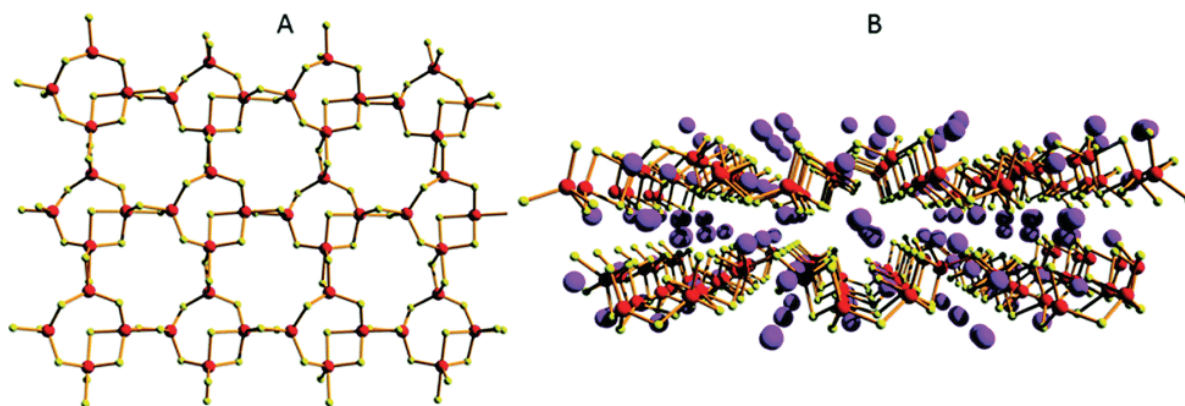


Figure 8. (a) Part of the $\text{Sn}_4\text{S}_9^{2-}$ layer (Sn, red; S, yellow). (b) The arrangement of two adjacent layers with the cations (Cs^+ , pink) filling the interlayer space. M. G. Kanatzidis, *Chem. Sci.*, **2016**, 7, 4804 © Royal Society of Chemistry.

Layered sulfides with trivalent metal ions in their framework.

Layered sulfide materials with trivalent ions like In^{3+} or Ga^{3+} tends to prefer tetrahedral

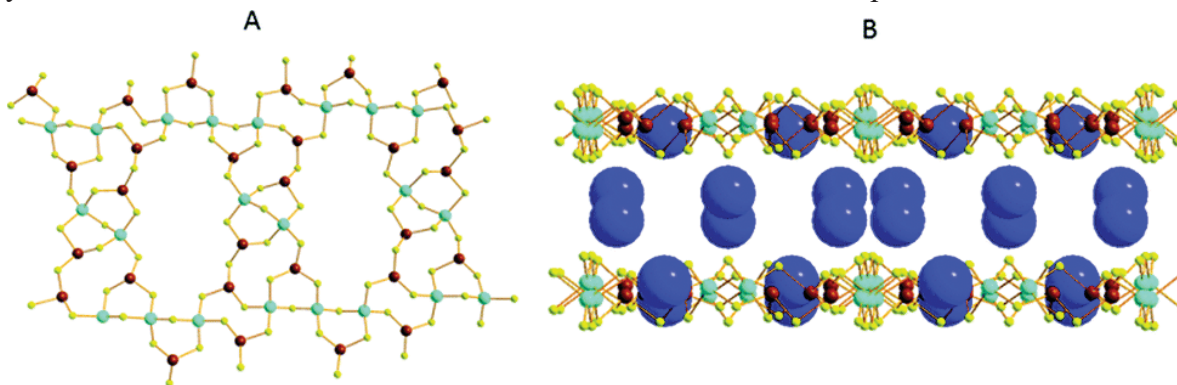


Figure 9 (a) Part of the $[\text{In}_5\text{Sb}_6\text{S}_{19}]^{5-}$ layer viewed down the b -axis. (b) Packing of the layers with the N atoms of dipropylammonium cations showing as large balls (C and H atoms were omitted for clarity). In, cyan; Sb, brown; N, blue; S, yellow. M. G. Kanatzidis, *Chem. Sci.*, **2016**, 7, 4804 © Royal Society of Chemistry.

coordination and Sb^{3+} adopts trigonal pyramidal coordination geometry. InSbS

$[(\text{CH}_3\text{CH}_2\text{CH}_2)_2\text{NH}_2]_5\text{In}_5\text{Sb}_6\text{S}_{19} \cdot 1.45\text{H}_2\text{O}$) composed of corner shared InS_4 tetrahedral, bridged by SbS_3 trigonal pyramidal units and Sb_2S_6 dimers with large holes which can accommodate organic counter ions (see figure 9). Facile ion-exchange for Cs^+ and Rb^+ have been explored by N. Ding and M. G. Kanatzidis.²⁹ GaSbS-1 ($[\text{CH}_2\text{NH}_2]_2\text{Ga}_2\text{Sb}_2\text{S}_7 \cdot \text{H}_2\text{O}$) comprises of two corner-shared GaS_4 tetrahedra which are bridged by two SbS_3 trigonal pyramidal units forming open window of size $11.36 \times 4.28 \text{ \AA}^2$. Dimethyl ammonium cations, present in the interlayer space by the interaction of N-H with S^{2-} via hydrogen bonding, can be exchanged with Cs^+ leading to the closing of the windows and the size changes to $11.85 \times 3.69 \text{ \AA}^2$. This mechanism is similar to insect capturing by the Venus flytrap plant.³⁰

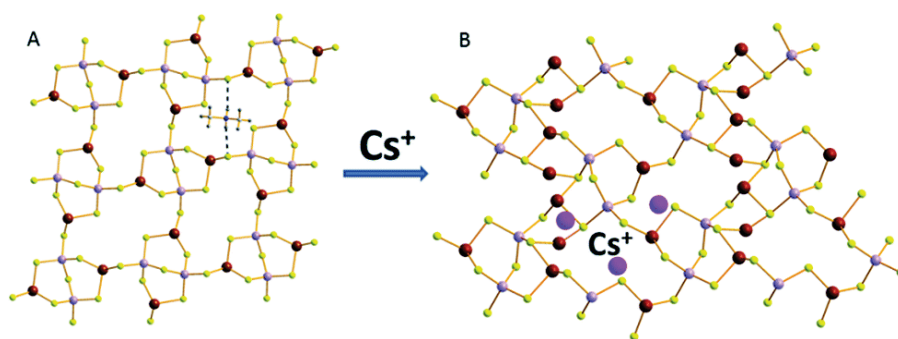


Figure 10 (a) Part of the layer of GaSbS-1 . The dashed lines represent hydrogen bonding interactions between the dimethylammonium ions and the layer. (b) Part of the layer of GaSbS-2 and some of the interlayer Cs^+ ions. Ga, purple; Sb, brown; S, yellow; Cs, pink. M. G. Kanatzidis, *Chem. Sci.*, **2016**, 7, 4804 © Royal Society of Chemistry.

Polysulfide and MoS_4^{2-} intercalated layered double hydroxides.

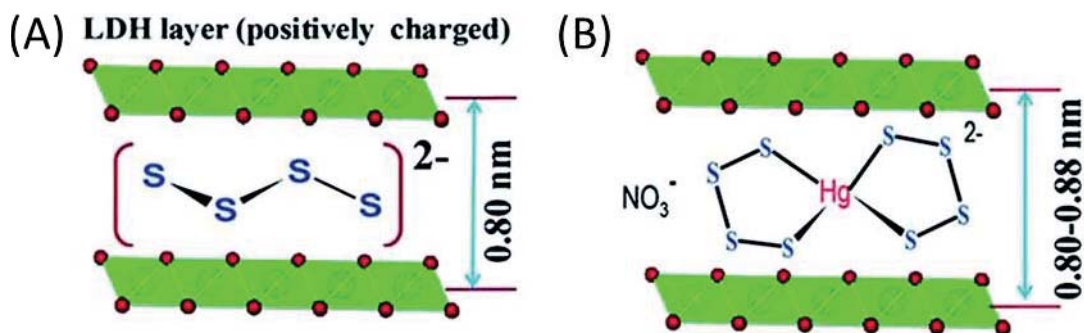


Figure 11 (a) Arrangement of $[\text{S}_4]^{2-}$ groups in the interlayer space of the LDH material and (b) Proposed binding of metal ions with the polysulfide unit. Metal, green; O, red. M. J. Manos, M. G.

Kanatzidis, *Chem. Sci.*, **2016**,7, 4804 © Royal Society of Chemistry.

Recently, S. Ma *et al.* designed a new type of layered double hydroxides (LDHs) intercalated by polysulfide $[S_x]^{2-}$ groups (Figure 11a). They can be ion-exchanged with series of metal ions, such as Ni^{2+} , Co^{2+} , Cu^{2+} , Cd^{2+} , Hg^{2+} , Pb^{2+} , Zn^{2+} , UO_2^{2+} and Ag^+ .^{31, 32} The mechanism of metal ion-exchange is dependent on the metal ion:LDH (S_x) molar ratio. The $[S_x]^{2-}$ groups act as a second host for the incoming ions, shown in Figure 11b.

1.2.3 Metal chalcophosphates.

Transition metal chalcophosphate MPX_3 ($M = Mg, V, Mn, Fe, Co, Ni, Zn, Pd,$ and Cd ; $X = S, Se$) are semiconducting two-dimensional material. Several phases of MPS_3 were first reported by Friedel.³³ First transition metal series adopts the $FePS_3$ structure that is based on cubic close-packed anion array with alternate layers of vacant cationic sites. Within the layer, the cationic sites are occupied by M^{2+} cations and P_2 pairs, as shown in Figure 12.

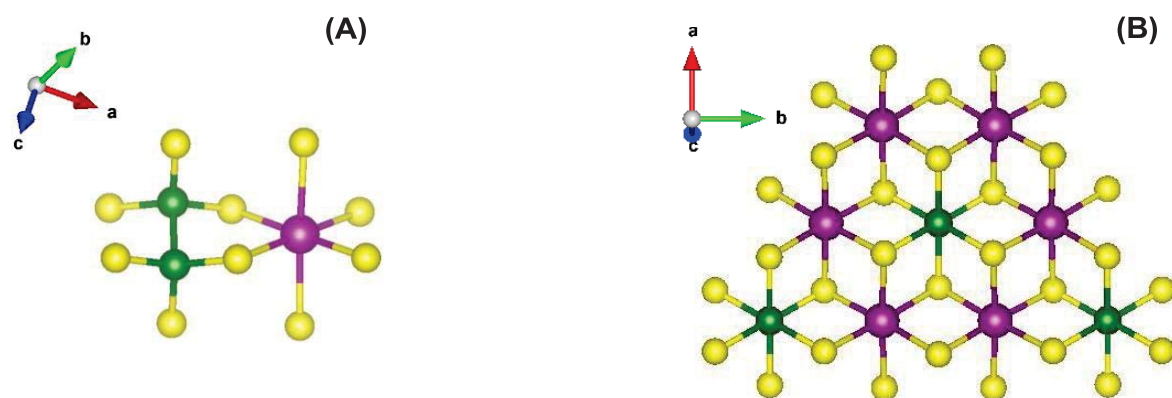


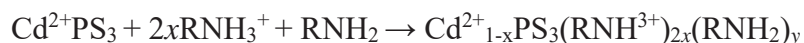
Figure 12. (a) MPS_3 structure showing the connection of P_2S_6 and MS_6 octahedra and (b) ordered arrangement within a single layer. Violet, green and yellow are metal, phosphorous and sulfur atoms.

Each P_2S_6 octahedron is surrounded by six MS_6 octahedra and each MS_6 octahedron has 3 each of MS_6 and P_2S_6 neighbors. The general composition can be written as $M_{2/3}(P_2)_{1/3}S_2$ to emphasize the structural relationship to the dichalcogenides.^{5, 6} The host lattice of MPS_3 is either semiconductor

or insulator and the transition metal compounds have magnetic properties characteristic of high-spin octahedral cations. At lower temperatures, the antiferromagnetic order is observed but the susceptibility maxima are broad, indicative of the strong two-dimensional nature of the magnetic interactions.

1.2.3.1 Molecular intercalations.

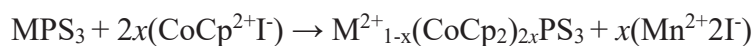
Organic molecules intercalate in transition metal thiophosphates. MgPS_3 , MnPS_3 , CdPS_3 and ZnPS_3 react with n-alkylamines to give rise to intercalation compounds. Pyridine also intercalates in MnPS_3 and expands the layer by 5.9 Å but it fails to intercalate in FePS_3 :



Intercalation of N-methylated pyridospiropyran cations SP-R^+ (R= Me, Ph) into MnPS_3 exhibit photochromism due to spiropyran-merocyanin transformation as intercalation stabilizes the merocyanin form.³⁴

1.2.3.2 Intercalations of organometallic molecules.

Clement *et al.* have reported intercalations of organometallic molecules like $\text{Co}(\eta\text{-C}_5\text{H}_5)_2$ and $[\text{Cr}(\eta\text{-C}_6\text{H}_6)_2]$ with lamellar compounds MPS_3 , (M = Mn, Zn, Fe, or Ni) which form intercalates of general stoichiometry $\text{MPS}_3[\text{Co}(\eta\text{-C}_5\text{H}_5)_2]^x$ and $\text{MPS}_3[\text{Cr}(\eta\text{-C}_6\text{H}_6)_2]^x$. The organometallic molecule transfers its electron to the conduction band of the host lattice and is subsequently intercalated as a cation, causing a substantial lattice expansion. Molecules like bi-pyridine have also been intercalated in MnPS_3 to form $\text{Mn}_{0.86}\text{PS}_3(\text{bipy})_{0.56}$.³⁵ The general reaction for intercalation by cation transfer with cobaltocene iodide is given as



The infrared spectra of the intercalation compounds show the bands expected for the metallocene

cation and the absorption of the host lattices is altered. In the pure hosts, the dominant feature is a strong absorption at 560-570 cm^{-1} , which has been assigned to an asymmetric P-S stretching mode. In the cobaltocene intercalates of MnPS_3 , CdPS_3 , and FePS_3 , this band splits into two lines, whereas in NiPS_3 it splits into three lines.³⁶ This indicates that some distortion of the $\text{P}_2\text{S}_6^{4-}$ octahedron has taken place. A cationic iron (III) complex $[\text{Fe}^{3+}(\text{5-OMe-sal}_2\text{trien})]^+$ have been inserted into MnPS_3 host lattice which undergoes spin crossover and shows magnetism.³⁷ A family of macrocyclic complexes $[\text{M}_2\text{LnCl}_2]$ where M: Cu^{2+} or Zn^{2+} ; Ln: macrocyclic ligand derived from 2-hydroxy-5-methyl-1,3-benzenedicarbaldehyde and different aliphatic diamines and o-phenylenediamine have also been synthesized by intercalating in the interlamellar space by a microwave assisted cationic exchange reaction.³⁸

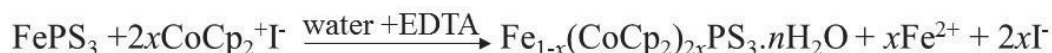
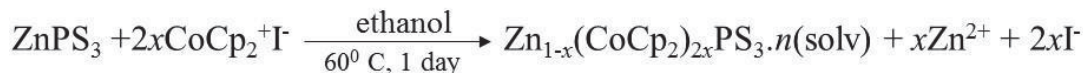
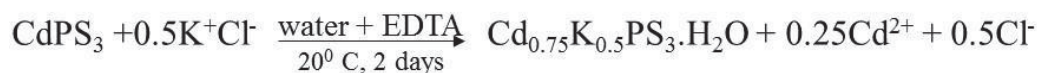
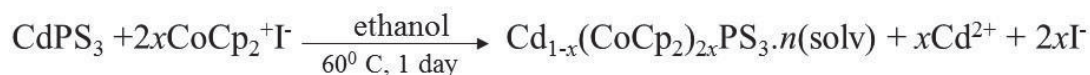
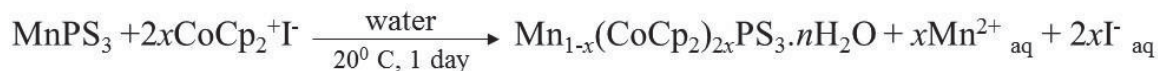
1.2.3.3 Cationic substitution-intercalation.

Clement and Green showed that many ionic salts (G^+X^-) can be intercalated in a polar medium and at room temperature according to:



with $\text{G} = (\text{C}_2\text{H}_5)_4\text{N}^+$, $\text{Co}(\eta\text{-C}_5\text{H}_2)^+$, pyH^+ and $\text{X} = \text{Cl}^-$, I^-

Substitution is easily achieved in the case of MnPS_3 , CdPS_3 , and ZnPS_3 as M^{2+} ions are not stabilized by ligand field. It is difficult for more stabilized Fe^{2+} ($t^4_{2g}e^2_g$) to undergo substitution.



Hence, basic pH and strong complexing agent (EDTA) are needed to reach sizeable substitution.

1.2.3.4 Ion-exchange in MPS_3

In the cation-exchange process, the electrical charge of the cationic guest species entering the host lattice is counterbalanced by the loss of intralayer M^{2+} ions. An important feature of the ion exchange chemistry in MPS_3 class is that it yields intercalates which are generally air stable, well crystallized.

The K^+ ions of a $\text{K}_{2x}\text{Mn}_{1-x}\text{PS}_3$ pre-intercalate are exchanged with the tetrafluoroborate salt $(\text{TTF})_3(\text{BF}_4)_2$ in acetonitrile medium. The compound obtained under this conditions was formulated as $\text{Mn}_{0.83}\text{PS}_3 \cdot (\text{TTF})_{0.42}\text{K}_{0.10}(\text{solv})_y$. Polyethylene oxide, $(\text{C}_2\text{H}_4\text{O})_n$ [PEO], a polymer has also been intercalated in MnPS_3 . Intercalation of potentially reactive transition- metal complexes like $\text{Cr}(\text{en})_3\text{Cl}_3$, $\text{Ru}(\text{bpy})_3\text{Cl}_3$ and cyclopentadienylcarbnyl(diphos)iron monocation leads to dramatic modification in magnetic properties. New hetero-metallic materials, $\text{Cu}_{0.2}\text{Mn}_{0.8}\text{PS}_3 \cdot 0.25\text{H}_2\text{O}$, $\text{Co}_{0.2}\text{Mn}_{0.8}\text{PS}_3 \cdot 0.25\text{H}_2\text{O}$, $\text{Ni}_{0.2}\text{Mn}_{0.8}\text{PS}_3 \cdot 0.25\text{H}_2\text{O}$ and $\text{Zn}_{0.2}\text{Mn}_{0.8}\text{PS}_3 \cdot 0.25\text{H}_2\text{O}$, with an ordered distribution of the secondary metal ions have also been synthesized and shows improved magnetic properties.^{39, 40} Cationic complexes $[\text{M}(\text{salen})]^+$ ($\text{M}=\text{Mn}^{3+}, \text{Fe}^{3+}, \text{Co}^{3+}$; salen=N,N-ethylene-bis(salicylal- dimine)) also accommodates themselves in the space between the layers of MPS_3 .⁴¹ Intercalation compound, $\text{Mn}_{0.84}\text{PS}_3(\text{phen})_{0.64}$ (phen=1,10-phenanthroline) exhibits bulk spontaneous magnetization below 36K.⁴² Polymer-inorganic intercalation nano-composite based on a C_{60} -containing poly-(ethylene oxide) (C_{60} -PEO) into layered MnPS_3 have shown a magnetic phase transition from paramagnetism to ferrimagnetism at about 40 K.⁴³ Interestingly, aminoacid intercalates, $\text{Mn}_{0.83}\text{PS}_3(\text{His})_{0.34}$, $\text{Mn}_{0.83}\text{PS}_3(\text{Lys})_{0.35}$ and $\text{Mn}_{0.88}\text{PS}_3(\text{Arg})_{0.25}$ are the first example of a magnetic bioorganic/inorganic

material synthesized by inserting a biomolecule into a layered inorganic host.⁴⁴

1.2.4 Summary

In this chapter, I have discussed Intercalated layered inorganic solids are new class of ion-exchangers, which seem highly promising for environmental remediation applications. Clays, alkali-intercalated metal sulfides like Li_xMoS_2 , KMS-1, KMS-2, KTS-1, layered double hydroxides, protonated acid metal sulfide like LHMS-1, layered sulfides with trivalent metal ions in the framework, etc. have been studied extensively to capture heavy metals like Pb^{2+} , Cd^{2+} , Hg^{2+} , Ni^{2+} , Co^{2+} and radioactive species like Sr^{2+} , Cs^+ , UO_2^{2+} . In the following chapters (Part 3), I will be discussing highly selective and efficient removal efficiency of KMPS-1 towards Cd (II) (Chapter -1) and Co, Al-LDH towards AsO_4^{3-} and SeO_4^{2-} (chapter-2) even up to ppb level with a very fast kinetics and broad pH range.

1.2.5 References.

1. Rao, C.; Ramakrishna Matte, H.; Maitra, U., Graphene analogues of inorganic layered materials. *Angew. Chem. Int. Ed.* **2013**, *52* (50), 13162-13185.
2. Wallace, P. R., The band theory of graphite. *Phys. Rev. Lett.* **1947**, *71* (9), 622.
3. Keyes, R. W., The electrical properties of black phosphorus. *Phys. Rev. Lett.* **1953**, *92* (3), 580.
4. Chhowalla, M.; Shin, H. S.; Eda, G.; Li, L.-J.; Loh, K. P.; Zhang, H., The chemistry of two-dimensional layered transition metal dichalcogenide nanosheets. *Nat. Chem.* **2013**, *5* (4), 263-275.
5. Whittingham, M. S., *Intercalation chemistry: an introduction*. Academic Press New York: 1982.
6. Rao, C. N. R.; Gopalakrishnan, J., *New directions in solid state chemistry*. Cambridge University Press: 1997.
7. Rao, C. N. R.; Biswas, K., *Essentials of inorganic materials synthesis*. John Wiley & Sons: 2015.
8. Jacobson, A. J.; Nazar, L. F., Intercalation chemistry. *Encyclopedia of Inorganic Chemistry* **2006**.
9. Clearfield, A., Role of ion exchange in solid-state chemistry. *Chem. Rev.* **1988**, *88* (1), 125-148.
10. Barrer, R. M., *Zeolites and clay minerals as sorbents and molecular sieves*. 1978.
11. Liebau, F., *Structural chemistry of silicates: structure, bonding, and classification*. Springer Science & Business Media: 2012.
12. Kojima, Y.; Usuki, A.; Kawasumi, M.; Okada, A.; Fukushima, Y.; Kurauchi, T.; Kamigaito, O., Mechanical properties of nylon 6-clay hybrid. *J. Mater. Res.* **1993**, *8* (5), 1185-1189.
13. Krishnamoorti, R., Vaia, and EP Giannelis. *Chem. Mater* **1996**, *8*, 1728.
14. Lan, T.; Pinnavaia, T. J., Clay-reinforced epoxy nanocomposites. *Chem. Mater.* **1994**, *6* (12), 2216-2219.
15. Pinnavaia, T. J.; Tzou, M.-S.; Landau, S. D.; Raythatha, R. H., On the pillaring and delamination of smectite clay catalysts by polyoxo cations of aluminum. *J. Mol. Catal.* **1984**, *27* (1-2), 195-212.
16. Khan, A. I.; O'Hare, D., Intercalation chemistry of layered double hydroxides: recent

- developments and applications. *J. Mater. Chem.* **2002**, *12* (11), 3191-3198.
17. Allmann, R. v., Doppelschichtstrukturen mit brucitähnlichen Schichtionen $[\text{Me (II)}_{1-x}\text{Me (III)}_x(\text{OH})_2]^{x+}$. *Chimia* **1970**, *24*, 99-108.
 18. Boehm, H. P.; Steinle, J.; Vieweger, C., $[\text{Zn}_2\text{Cr}(\text{OH})_6]_x \cdot 2\text{H}_2\text{O}$, New layer compounds capable of anion exchange and intracrystalline swelling. *Angew. Chem. Int. Ed.* **1977**, *16* (4), 265-266.
 19. Rouxel, J., Recent Progress in Intercalation Chemistry: Alkali Metal in Chalcogenide Hosts. *Rev. Inorg. Chem* **1979**, *1*, 245-279.
 20. England, W.; Goodenough, J.; Wiseman, P., Ion-exchange reactions of mixed oxides. *J. Solid State Chem.* **1983**, *49* (3), 289-299.
 21. Mertz, J. L.; Fard, Z. H.; Malliakas, C. D.; Manos, M. J.; Kanatzidis, M. G., Selective Removal of Cs^+ , Sr^{2+} , and Ni^{2+} by $\text{K}_{2x}\text{Mg}_x\text{Sn}_{3-x}\text{S}_6$ ($x=0.5-1$)(KMS-2) Relevant to Nuclear Waste Remediation. *Chem. Mater.* **2013**, *25* (10), 2116-2127.
 22. Manos, M. J.; Kanatzidis, M. G., Highly efficient and rapid Cs^+ uptake by the layered metal sulfide $\text{K}_{2x}\text{Mn}_x\text{Sn}_{3-x}\text{S}_6$ (KMS-1). *J. Am. Chem. Soc.* **2009**, *131* (18), 6599-6607.
 23. Manos, M. J.; Kanatzidis, M. G., Sequestration of heavy metals from water with layered metal sulfides. *Chem. Eur. J.* **2009**, *15* (19), 4779-4784.
 24. Manos, M. J.; Petkov, V. G.; Kanatzidis, M. G., $\text{H}_{2x}\text{Mn}_x\text{Sn}_{3-x}\text{S}_6$ ($x=0.11-0.25$): A Novel Reusable Sorbent for Highly Specific Mercury Capture Under Extreme pH Conditions. *Adv. Funct. Mater.* **2009**, *19* (7), 1087-1092.
 25. Parise, J. B.; Ko, Y.; Rijssenbeek, J.; Nellis, D. M.; Tan, K.; Koch, S., Novel layered sulfides of tin: synthesis, structural characterization and ion exchange properties of TMA-SnS-1, $\text{Sn}_3\text{S}_7 \cdot (\text{NMe}_4)_2 \cdot \text{H}_2\text{O}$. *Journal of the Chemical Society, Chemical Communications* **1994**, (4), 527-527.
 26. Qi, X.-H.; Du, K.-Z.; Feng, M.-L.; Li, J.-R.; Du, C.-F.; Zhang, B.; Huang, X.-Y., A two-dimensionally microporous thiostannate with superior Cs^+ and Sr^{2+} ion-exchange property. *J. Mat. Chem. A* **2015**, *3* (10), 5665-5673.
 27. Marking, G. A.; Evain, M.; Petricek, V.; Kanatzidis, M. G., New Layered Compounds through Polysulfide Flux Synthesis; $\text{A}_2\text{Sn}_4\text{S}_9$ (A= K, Rb, Cs) Present a New Form of the $[\text{Sn}_4\text{S}_9]^{2-}$ Network. *J. Solid State Chem.* **1998**, *141* (1), 17-28.
 28. Sarma, D.; Malliakas, C. D.; Subrahmanyam, K.; Islam, S. M.; Kanatzidis, M. G., $\text{K}_{2x}\text{Sn}_{4-x}\text{S}_{8-x}$ ($x=0.65-1$): a new metal sulfide for rapid and selective removal of Cs^+ , Sr^{2+} and UO_2^{2+} ions. *Chem. Sci.* **2016**, *7* (2), 1121-1132.
 29. Ding, N.; Kanatzidis, M. G., Permeable Layers with Large Windows in $[(\text{CH}_3\text{CH}_2\text{CH}_2)_2\text{NH}_2]_5\text{In}_5\text{Sb}_6\text{S}_{19} \cdot 1.45\text{H}_2\text{O}$: High Ion-Exchange Capacity, Size Discrimination, and Selectivity for Cs Ions. *Chem. Mater.* **2007**, *19* (16), 3867-3869.

30. Ding, N.; Kanatzidis, M. G., Selective incarceration of caesium ions by Venus flytrap action of a flexible framework sulfide. *Nat. Chem.* **2010**, *2* (3), 187-191.
31. Ma, S.; Chen, Q.; Li, H.; Wang, P.; Islam, S. M.; Gu, Q.; Yang, X.; Kanatzidis, M. G., Highly selective and efficient heavy metal capture with polysulfide intercalated layered double hydroxides. *J. Mater. Chem. A* **2014**, *2* (26), 10280-10289.
32. Ma, L.; Wang, Q.; Islam, S. M.; Liu, Y.; Ma, S.; Kanatzidis, M. G., Highly selective and efficient removal of heavy metals by layered double hydroxide intercalated with the MoS_4^{2-} ion. *J. Am. Chem. Soc.* **2016**, *138* (8), 2858-2866.
33. Brec, R., Review on structural and chemical properties of transition metal phosphorus trisulfides MPS₃. In *Intercalation in Layered Materials*, Springer: 1986; pp 93-124.
34. Bénard, S.; Léaustic, A.; Rivière, E.; Yu, P.; Clément, R., Interplay between Magnetism and Photochromism in Spiropyran– MnPS₃ Intercalation Compounds. *Chem. Mater.* **2001**, *13* (10), 3709-3716.
35. Qin, J.; Yang, C.; Yakushi, K.; Nakazawa, Y.; Ichimura, K., Synthesis and properties of a new ferromagnetic 2, 2'-bipyridine-MnPS₃ intercalation compound. *Solid State Commun.* **1996**, *100* (6), 427-431.
36. Sourisseau, C.; Forgerit, J.; Mathey, Y., Vibrational study of the $[\text{P}_2\text{S}_4^{-6}]$ anion, of some MPS₃ layered compounds (M= Fe, Co, Ni), and of their intercalates with $[\text{Co}(\eta^5\text{-C}_5\text{H}_5)^{+2}]$ cations. *J. Solid State Chem.* **1983**, *49* (2), 134-149.
37. Floquet, S.; Salunke, S.; Boillot, M.-L.; Clément, R.; Varret, F.; Boukheddaden, K.; Rivière, E., The spin transition of an iron (III) complex intercalated in a MnPS₃ layered magnet. Occurrence of a hysteresis effect on removal of lattice solvent. *Chem. Mater.* **2002**, *14* (10), 4164-4171.
38. Fuentealba, P.; Serón, L.; Sánchez, C.; Manzur, J.; Paredes-Garcia, V.; Pizarro, N.; Cepeda, M.; Venegas-Yazigi, D.; Spodine, E., Macrocyclic ZnII and CuII complexes as guests of the hybrid composites based on the layered MnPS₃ phase. Comparison of spectroscopic properties. *J. Coord. Chem.* **2014**, *67* (23-24), 3894-3908.
39. Clement, R., Intercalation of potentially reactive transition-metal complexes in the lamellar manganese phosphide sulfide host lattice. *J. Am. Chem. Soc.* **1981**, *103* (23), 6998-7000.
40. Oriakhi, C. O.; Lerner, M. M., Rapid and quantitative displacement of poly (ethylene oxide) from MnPS₃ and other layered hosts. *Chem. Mater.* **1996**, *8* (8), 2016-2022.
41. Zhang, X.; Zhou, H.; Su, X.; Chen, X.; Yang, C.; Qin, J.; Inokuchi, M., Synthesis, characterization and magnetic properties of transition metal salen complexes intercalated into layered MnPS₃. *J. Alloys Compd.* **2007**, *432* (1-2), 247-252.
42. Yang, C.; Chen, X.; Qin, J.; Yakushi, K.; Nakazawa, Y.; Ichimura, K., Synthesis, characterization, and magnetic properties of intercalation compound of 1, 10-phenanthroline

- with layered MnPS₃. *J. Solid State Chem.* **2000**, *150* (2), 281-285.
43. Chen, X.; Li, Z.; Zhou, H.; Wang, T.; Qin, J.; Inokuchi, M., The intercalation of C60-containing PEO into layered MnPS₃. *Polymer* **2007**, *48* (11), 3256-3261.
44. Zhou, H.; Su, X.; Zhang, X.; Chen, X.; Yang, C.; Qin, J.; Inokuchi, M., Intercalation of amino acids into layered MnPS₃: Synthesis, characterization and magnetic properties. *Mater. Res. Bull.* **2006**, *41* (11), 2161-2167.

PART 2

**Enhanced Thermoelectric
Performance in GeTe Based
Materials.**

Chapter 2.1

**Low Thermal Conductivity and
High Seebeck Coefficient
Leads to High Thermoelectric
Performance in Pseudoternary
 $\text{Ge}_{1-2x}\text{Pb}_x\text{Sn}_x\text{Te}$**

Chapter 2.1

Low Thermal Conductivity and High Seebeck Coefficient Leads to High Thermoelectric Performance in Pseudoternary $\text{Ge}_{1-2x}\text{Pb}_x\text{Sn}_x\text{Te}$

Summary

Thermoelectric (TE) energy conversion demands high performance crystalline inorganic solids that exhibit ultralow thermal conductivity, high mechanical stability, and good TE device properties. Recently, germanium telluride (GeTe) based material has recently attracted significant attention in TE power generation in mid temperatures, but pristine GeTe possesses significantly higher lattice thermal conductivity (κ_L) compared to that of its theoretical minimum (κ_{\min}) of ~ 0.3 W/mK. In this chapter, we have demonstrated the reduction of κ_L of ball milled and sps processed $\text{Ge}_{1-2x}\text{Pb}_x\text{Sn}_x\text{Te}$ very near to its κ_{\min} . Initially, the addition of equimolar PbTe and SnTe in the GeTe reduces the κ_L by effective phonon scattering owing to excess point defects and rich microstructures. In the second step, introduction of Sb doping leads additional phonon scattering centers and optimizes the p-type carrier concentration and finally, ball milled and sps processed 11 mol% Sb-doped $\text{Ge}_{0.95}\text{Pb}_{0.025}\text{Sn}_{0.025}\text{Te}$ exhibits ultralow κ_L of ~ 0.60 W/m.K at 300 K. Subsequently, ball milled 11 mol% Sb-doped $\text{Ge}_{0.95}\text{Pb}_{0.025}\text{Sn}_{0.025}\text{Te}$ exhibits high TE figure of merit (zT) of ~ 2.1 at 723 K. Further, we have achieved a high output power, ~ 240 mW for the temperature difference of 434 K, in single leg TE device based on 11 mol% Sb-doped ball milled $\text{Ge}_{0.95}\text{Pb}_{0.025}\text{Sn}_{0.025}\text{Te}$.

2.1.1 Introduction.

IV-VI metal chalcogenides are the most promising candidates for thermoelectric power generation in the mid-temperature (600-900 K) operational range.^{1, 2-4} Recently, germanium telluride (GeTe) from IV-VI family emerged as a potential candidate due to its unique properties.⁵⁻⁷ GeTe crystallizes in a rhombohedral (α phase, R3m) structure (r-GeTe) at room temperature and rock salt cubic (β phase, Fm-3m) structure (c-GeTe) at high temperature (> 700 K). It undergoes a ferroelectric structural 2nd order phase transition from α phase to β phase at ~ 700 K due to the slight displacement of the Ge atoms originating from shear distortion of the lattice along [111] crystallographic direction.⁸ Pristine GeTe contains intrinsic germanium vacancies, which leads to the high p type carrier density ($\sim 10^{21}$ /cm³) resulting in a very high σ of ~ 8500 S/cm, low S of ~ 34 μ V/K and high κ_T of ~ 8 W/m.K at 300 K.^{9, 10} Thus, the TE properties of pristine GeTe are rather poor and maximum zT of ~ 0.8 is achieved at 723 K. Although in the last couple of years, we have seen a drastic advancement in the thermoelectric performance of GeTe accounted by the development of several novel methodologies and fabric plan techniques.^{7, 11}

Pristine GeTe exhibits κ_L of ~ 2.5 W/m.K at room temperature, whereas the theoretical minimum of κ_L is 0.3 W/m.K, indicating enormous plausibility of decreasing the κ_L of GeTe.¹² Solid solution alloying leads to decrease in κ_L as it creates point defects which scatters the phonon and in this context pseudoternary system is far ahead than the pseudobinary system as demonstrated in the recently published works like (PbTe)_{1-2x}(PbSe)_x(PbS)_x,¹³ (SnTe)_{1-2x}(SnSe)_x(SnS)_x,¹⁴ (GeTe)_{1-2x}(GeSe)_x(GeS)_x,¹⁵ and (GeTe)_{1-2x}(SnSe)_x(SnS)_x,¹⁶ this is because of the entropy driven enhanced disorder, large mass and lattice strain fluctuations, and the presence of extensive lattice distortions. with this stimulation, we think to do the exclusively cationic site alloying at Ge site of GeTe by Sn and Pb. Both SnTe and PbTe exhibits cubic rock salt structure and act as a donar dopant to GeTe system, which can further facilitate to optimize the p-type carrier density in GeTe. Besides Sn²⁺ exhibits Rashba spin splitting in GeTe, leading to band convergence

and resulting high power factor.¹⁷ Although while investigating such a complex pseudoternary system like $\text{Ge}_{1-2x}\text{Pb}_x\text{Sn}_x\text{Te}$, (GPST), few questions arise like (a) Is GPST form a solid solution, or it behaves as a phase separated system? (b) how are the lattice thermal conductivity and overall thermoelectric performance affected by the above parameters?

Herein, we have demonstrated excellent thermoelectric performance in pseudoternary $\text{Ge}_{1-2x}\text{Pb}_x\text{Sn}_x\text{Te}$ doping with Sb achieved by three step strategies. Firstly, SnTe and PbTe (0.025 mol% each) alloying create point defects in GeTe system, leading to the reduction of κ_L due to phonon scattering. In the second stage, Sb alloying in GPST again leads to a decrease in κ_L due to enhanced phonon scattering and optimized the p -type carrier concentration. In the final step, Ball milling and SPS were performed on the optimized $(\text{Ge}_{0.89}\text{Sb}_{0.11}\text{Te})_{0.95}(\text{PbTe})_{0.025}(\text{SnTe})_{0.025}$ (GPST_{0.025}-Sb-0.11) sample, which shows very low κ_L of 0.6 W/m.K (close to κ_{min} value of 0.3 W/m.K) and very high Seebeck coefficient of 280 $\mu\text{V/K}$ at 723 K. As a result, a high zT of 2.1 is achieved in $(\text{Ge}_{0.89}\text{Sb}_{0.11}\text{Te})_{0.95}(\text{PbTe})_{0.025}(\text{SnTe})_{0.025}$ at 723 K, which is thermally stable over the cycling and motivated by high thermoelectric figure of merit, we have studied the power conversion characteristics of the fabricated single leg device of ball milled $(\text{Ge}_{0.89}\text{Sb}_{0.11}\text{Te})_{0.95}(\text{PbTe})_{0.025}(\text{SnTe})_{0.025}$ sample and the device shows a high $P_{\text{max}} \sim 240$ mW at $\Delta T = 434$ K, which make the system as an efficient mid temperature power generation material.

2.1.2. Methods.

Reagents. Germanium (Alfa Aesar, 99.99+ %), Tin (Alfa Aesar, 99.99+ %) Tellurium (Alfa Aesar, 99.999+ %), Lead (Alfa Aesar, 99.99+ %) and Antimony (Alfa Aesar, 99.999+ %) were used for synthesis without further purification.

Synthesis. First, polycrystalline ingots (~ 6 g) of $(\text{GeTe})_{1-2x}(\text{PbTe})_x(\text{SnTe})_x$ were synthesized by mixing stoichiometric amounts of high purity starting materials of Ge, Te, Pb and Sn in quartz ampoule. The tubes were sealed under vacuum (10^{-6} Torr) and were slowly heated to 1223 K over

a period of 10 h, then kept for 6 h, and cooled slowly to room temperature over 10 h. Sb doped GPST_{0.025} ($x = 0.025$) were also synthesized by following similar procedure. Then 10.6 % and 11 % Sb doped sample were ball-milled into fine powders and consolidated by spark plasma sintering (SPS211-LX, Dr. Sinter Lab). The sintering was conducted with a pressure of 50 MPa at 450°C for 5 min under vacuum.

Powder X-ray Diffraction. Powder X-ray diffraction for all of the samples was recorded using a Cu K α ($\lambda = 1.5406 \text{ \AA}$) radiation on a Rigaku diffractometer.

Electrical Transport. Electrical conductivity and Seebeck coefficients were measured simultaneously under He atmosphere from room temperature to 723 K on a ULVAC-RIKO ZEM-3 instrument system. The typical sample for measurement had a parallelepiped shape with the dimensions of $\sim 2 \times 2 \times 8 \text{ mm}^3$.

Thermal Conductivity. Thermal diffusivity, D , was directly measured in the range 300–723 K by using laser flash diffusivity method in a Netzsch LFA-457. Coins with 10 mm diameter and 2 mm thickness were used in all of the measurements. Temperature dependent heat capacity, C_p , was derived using standard sample (pyroceram) in LFA457, which is in good agreement with Dulong Petit C_p value. The total thermal conductivity, κ_{total} , was calculated using the formula $\kappa_{\text{total}} = D \cdot C_p \cdot \rho$, where ρ is the density of the sample, measured using the sample dimension and mass.

2.1.3. Results and discussion.

Figure 1a reflects the PXRD pattern of GPST, which was synthesized by seal tube reaction under vacuum condition in high temperature (synthesis part). PXRD pattern could be pointed based on the Rhombohedral phase of GeTe & above $x \geq 0.015$, we found weak diffraction peak of Ge as well. With the increase in the Sn and Pb concentration, peak shifted to lower angle as there was an increase in the lattice parameter as size of Sn (118 pm) & Pb (119 pm) are higher than that of Ge (87 pm).

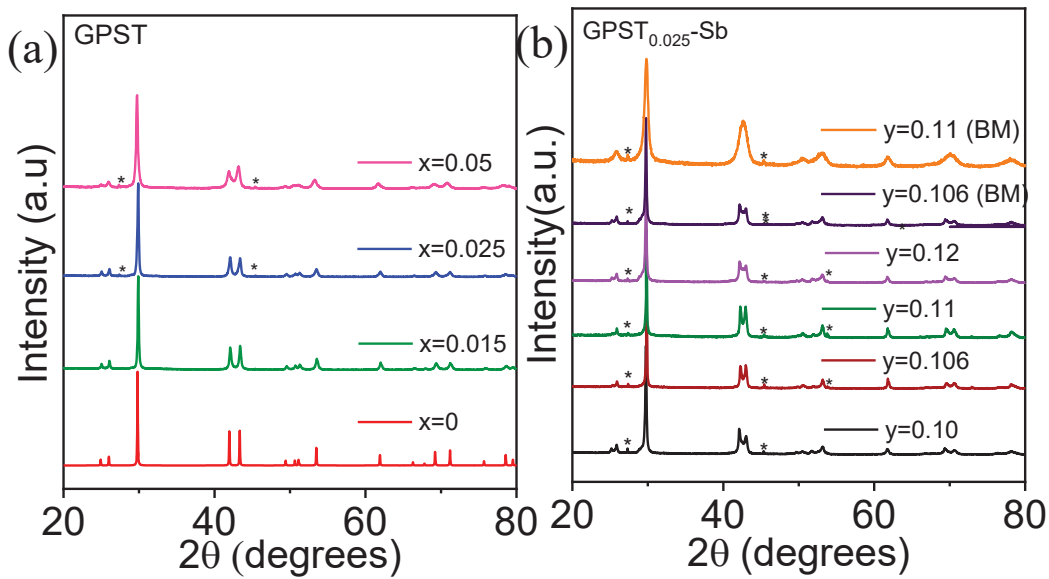


Figure 1. Powder X-ray diffraction pattern of (a) GPST ($x = 0 - 0.05$) samples (b). Ingot & ball milled GPST_{0.025}-Sb ($y = 0.10-0.12$) samples. (*) Sign signifies the presence of Ge impurity

To probe the microstructure composition and to analyze the surface of the material, Field emission scanning electron microscopy (FESEM) in Back scattered imaging (BSE) mode and Energy Dispersive Spectroscopy (EDS) were performed on the sample GPST_{0.025}. Figure 2a, b represents different magnified BSE-FESEM images of the polished surface of GPST_{0.025}. We observed microprecipitate of Ge of 2-20 μm size in the GeTe matrix, which was further verified by color mapping (Figure 2c-f) & EDS line spectra along the precipitate (Figure 2g-h). To check the nanoscale architecture, High resolution transmission electron microscopy (HRTEM) was also

performed as shown in Figure 3, where we found no such nanoprecipitate, indicating that below $x = 0.05$, system basically forms solid solution, rich with point defects.

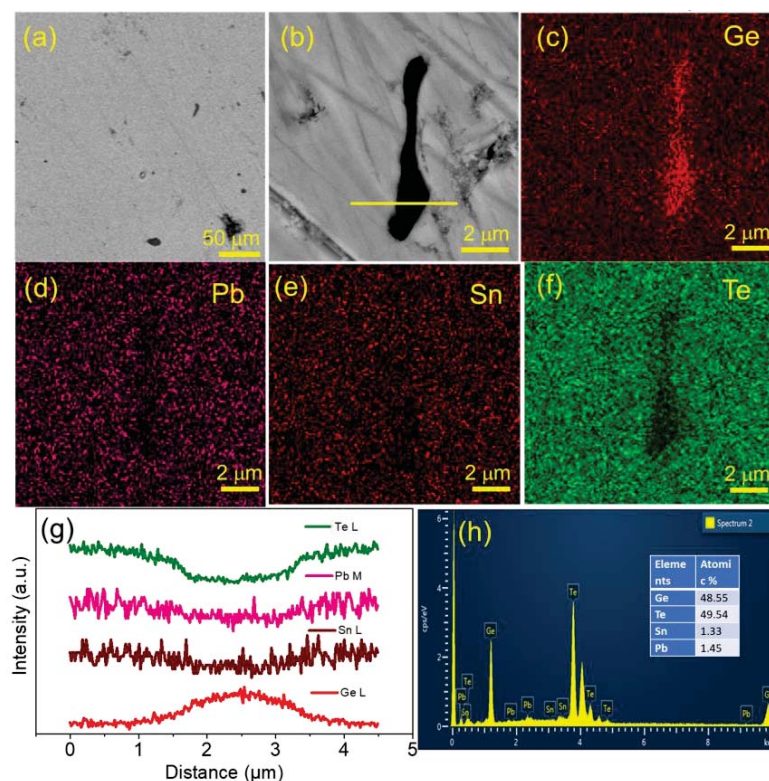


Figure 2. (a), (b) Back scattered FESEM images of $\text{GPST}_{0.025}$ different magnification from polished and rough surfaces. (c)-(f) Color mapping of the elements in the matrix and precipitate (g) EDS line scanning along the precipitate. (h) EDAX performed on matrix and precipitate respectively.

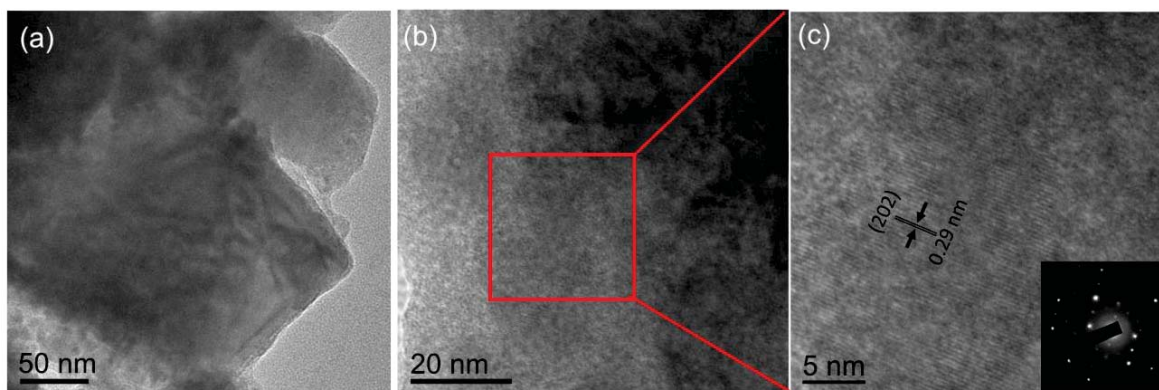


Figure 3. (a), (b) & (c) Low magnification TEM and HRTEM images of $\text{GPST}_{0.025}$

Temperature dependent thermoelectric properties of ingot $(\text{GeTe})_{1-2x}(\text{PbTe})_x(\text{SnTe})_x$ samples are shown in the Figure 4. Figure 4a shows the temperature dependent electrical conductivity

(σ) of GPST where the decreasing nature of σ with temperature resembles the degenerate semiconductor behaviour. With increase in the concentration of Sn & Pb, σ decreases, which can be attributed to decrease in carrier density as well as carrier mobility, which was verified by room temperature hall measurement (Table 1). Positive hall coefficient indicates that the majority carrier is hole. Seebeck coefficient of all the samples remained almost same along with pristine GeTe of ~ 35 $\mu\text{V/K}$ at room temperature (Figure 4b).

Temperature dependent thermal transport properties data of GPST ($x=0-0.05$) are illustrated in Figure 4c, d. κ_T decreases with increase in Sn and Pb content in GeTe. As example,

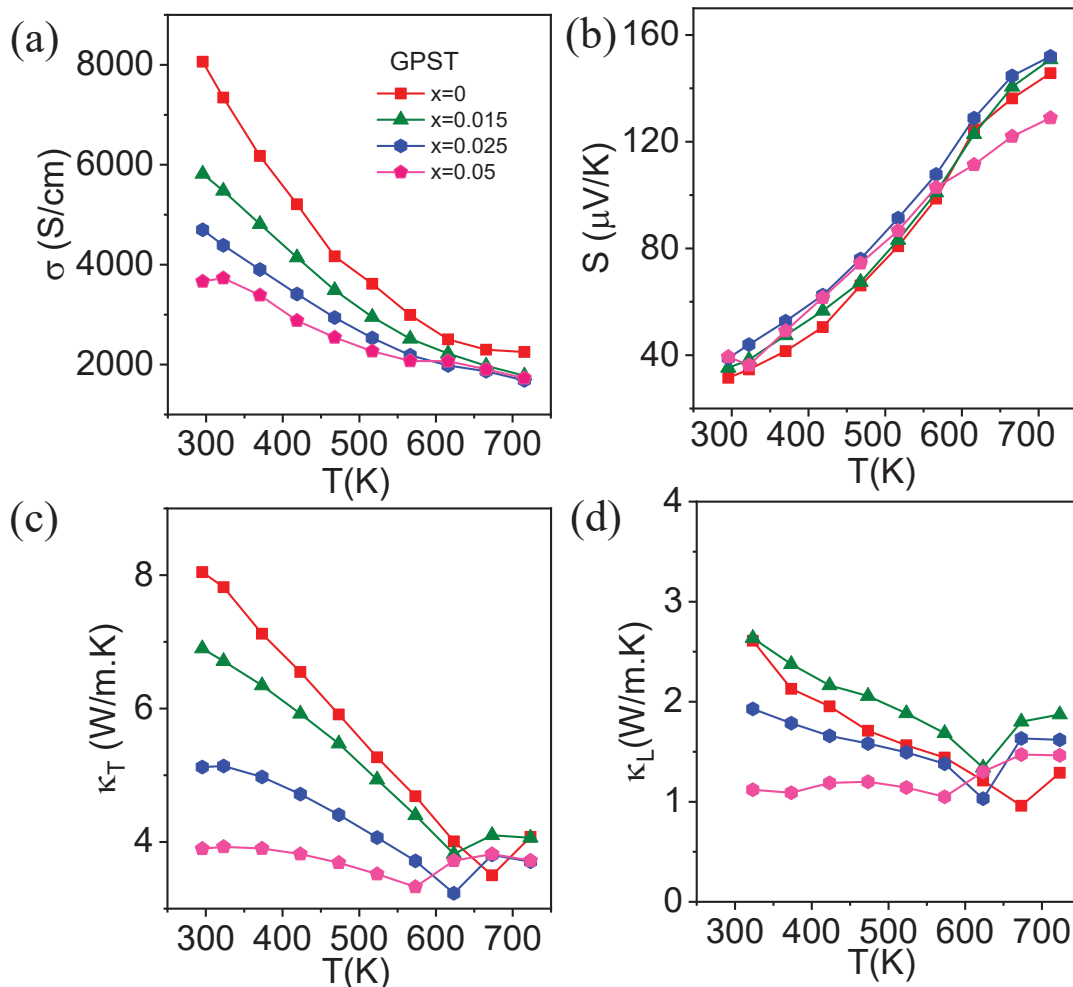


Figure 4. Temperature dependent (a) electrical conductivity (σ), (b) Seebeck coefficients (S), (c) total thermal conductivity (κ) and (d) lattice thermal conductivity (κ_{lat}) of GPST ($x = 0 - 0.05$) samples.

Pristine GeTe shows κ_T of ~ 8 W/mK, whereas for GPST_{0.025}, it, decreases to ~ 5.1 W/mK at room temperature. Lattice thermal conductivity (κ_L) was calculated by subtracting electrical thermal

Table 1: Carrier concentration and mobility values of GPST (x = 0 - 0.05) samples

Sample	Carrier Conc.($\times 10^{20}$)/cm ³	Mobility (cm ² /Vs)
GeTe	8.6	58.5
GPST _{0.015}	6.5	55.9
GPST _{0.025}	6.1	48.1
GPST _{0.05}	5.4	42.4

conductivity (κ_e), which was determined by using the law $\kappa_{el} = L\sigma T$, known as Wiedemann-Franz's law & where L is the Lorentz number, from total thermal conductivity (κ_T). L of all the samples were calculated by Seebeck vs temperature fitting.¹² Pristine GeTe shows κ_L of ~ 2.5 W/mK, which decreases to ~ 1.9 W/mK for GPST_{0.025} at room temperature & 1.6 W/mK at 723K, the cause of reduction in κ_L is mainly due to point defect and large mass fluctuations, as the micron size Ge precipitate would not be able to scatter the phonons effectively.¹⁸ The obtained lattice thermal conductivity of GPST_{0.025} sample (~ 1.9 W/mK) is much higher than κ_{min} of pristine GeTe, thus it is further leaving enormous scope for the reduction of κ_L to enhance the thermoelectric figure of merit (zT) values. Therefore, in the 2nd step, we have doped Sb in the optimized GPST_{0.025} sample as aliovalent Sb (III) doping at the Ge site effectively suppress the P-type carrier density & Sb doping increases the degeneracy ($N_v=12$) as the addition of Sb promotes the system to be more cubic nature at room temperature thereby increasing the Seebeck.¹⁹ We recorded Powder XRD patterns of GPST_{0.025}Sb (y = 0.10-0.12) samples at room temperature (Figure 1b), where also weak Ge diffraction peak was observed. The two peaks (024) and (220) which correspond to rhombohedral

GeTe, tends to merge with increasing the Sb concentration, indicates the augmented cubic nature in the system.

Temperature dependent electrical conductivity (σ) of Sb doped $\text{GPST}_{0.025}$ samples are shown

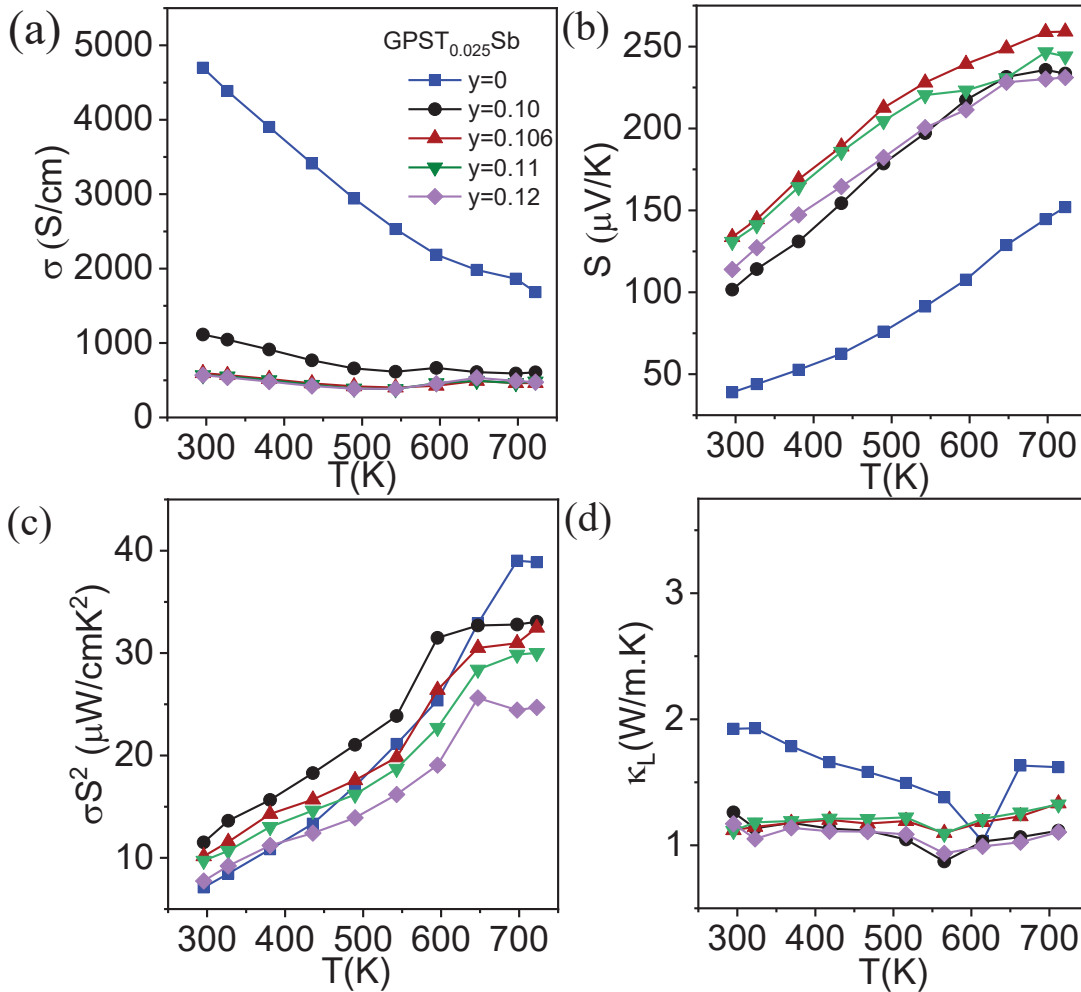


Figure 5. Temperature dependent (a) electrical conductivity (σ), (b) Seebeck coefficients (S), (c) power factor (σS^2) and (d) lattice thermal conductivity (κ_{lat}) of $\text{GPST}_{0.025}\text{-Sb}$ ($y = 0.10 - 0.12$) samples.

in Figure 5a. σ decreases with increasing Sb concentration, this is because of reduction in the p-type carrier density (Table 2). Typically, σ reduces from ~ 4800 S/cm for $\text{GPST}_{0.025}$ to ~ 600 S/cm for $\text{GPST}_{0.025}\text{-Sb-11}$ sample at room temperature. Seebeck coefficient, S , as a function of temperature for $\text{GPST}_{0.025}\text{-Sb}$ ($y = 0.10 - 0.12$) samples are unveiled in Figure 4b. $\text{GPST}_{0.025}\text{-Sb}$ ($y = 0.10 - 0.12$)

samples show comparatively higher Seebeck coefficients than undoped GPST sample over the whole temperature range.

Table 2: Carrier concentration and mobility values of Ingot & ball milled GPST_{0.025}Sb (y = 0.10-0.12) samples.

Samples GPST _{0.025} -Sb	Carrier Conc.($\times 10^{19}$)/cm ³
y = 0.10	4.27
y = 0.106	2.06
y = 0.106 (BM)	0.91
y = 0.11	1.96
y = 0.11 (BM)	0.73
y = 0.12	2.03

Typically, Seebeck value for GPST_{0.025}Sb-0.11 sample is $\sim 128 \mu\text{V/K}$ at room temperature which further increases to $230 \mu\text{V/K}$ at 723 K. This increase of Seebeck coefficient values with increasing the Sb concentration could be attributed to reduction of p-type carrier concentration.²⁰ Temperature dependent power factor (σS^2) for GPST_{0.025}Sb (y = 0.10 - 0.12) samples are shown in Figure 4c. GPST_{0.025} shows σS^2 of $\sim 8 \mu\text{W/cmK}^2$ at room temperature and $\sim 38 \mu\text{W/cmK}^2$ at 450° C, whereas GPST_{0.025}Sb-0.11 shows power factor of $10 \mu\text{W/cmK}^2$ at room temperature which reaches to $\sim 30 \mu\text{W/cmK}^2$ at 723K.

Figure. 6 shows temperature dependent total thermal conductivity (κ_T) of GPST_{0.025}Sb (y = 0.10- 0.12) samples. A significant reduction in κ_T is achieved by Sb doping in GPST_{0.025}. κ_T value of GPST_{0.025} is $\sim 5.1 \text{ W/mK}$ which is suppressed to $\sim 1.5 \text{ W/mK}$ in GPST_{0.025}Sb-0.11 at room temperature. κ_T of all samples shows an anomaly at 573 K, which is due to structural phase transition of GeTe. Lattice thermal conductivity (κ_L) of all the samples are obtained by subtracting the κ_e from

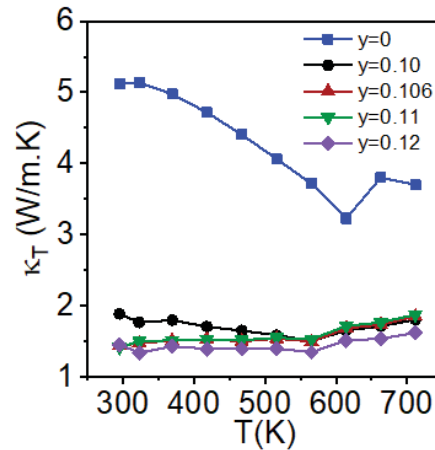


Figure 6. Temperature dependent total thermal conductivity (κ_T) of GPST_{0.025}Sb ($y = 0.10 - 0.12$) samples.

κ_T (Figure 5d). Among all the samples, GPST_{0.025}Sb-0.11 shows $\kappa_L \sim 1.1$ W/m.K at room temperature.

As there is still room to decrease the total as well as lattice thermal conductivity, we did ball milling on 10.6% and 11% Sb doped GPST_{0.025} samples. Room temperature PXRD pattern of the ball milled samples are also shown in Figure 1b. As shown in the figure, (024) and (220) peaks seem to merge to a single peak for ball milled GPST_{0.025}Sb-0.106 and GPST_{0.025}Sb-0.11 samples, indicating a cubic like structure. This can be attributed due to decrease in the crystallite size which causes the peak broadening.

BSE-FESEM of ball milled GPST_{0.025}Sb-0.11 was performed to analyze the surface morphology and microstructure composition. Figure 7a, b shows the FESEM micrograph of

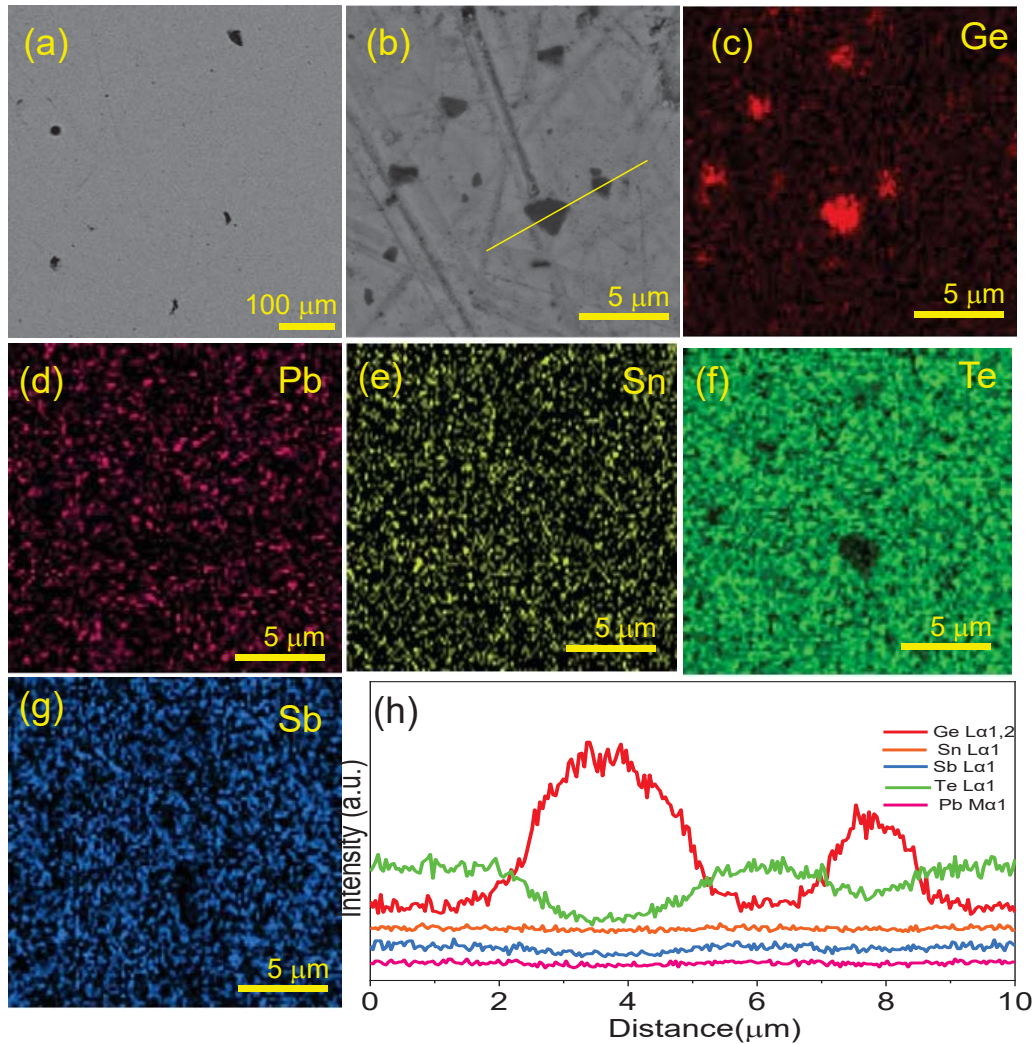


Figure 7. (a) & (b) Back scattered FESEM image of different magnification from the polished surface of ball milled GPST_{0.025}Sb-0.11 sample. (c)-(g) Color mapping of the elements in the matrix and precipitate (h), (i) EDAX line scanning along the precipitate.

different magnification. We found micro precipitate of Ge (~5-10 μm) in the matrix, which can be further confirmed by color mapping (Figure 7c - g), and EDS line scanning (Figure 7h) along the precipitate which appears as a dark contrast. To probe the nanoscale architecture, we did TEM

analysis (Figure. 8) of the ball milled $\text{GPST}_{0.025}\text{Sb-0.11}$ sample where we found the presence of Ge nanoprecipitate, as the size of the precipitate is in the same order with the

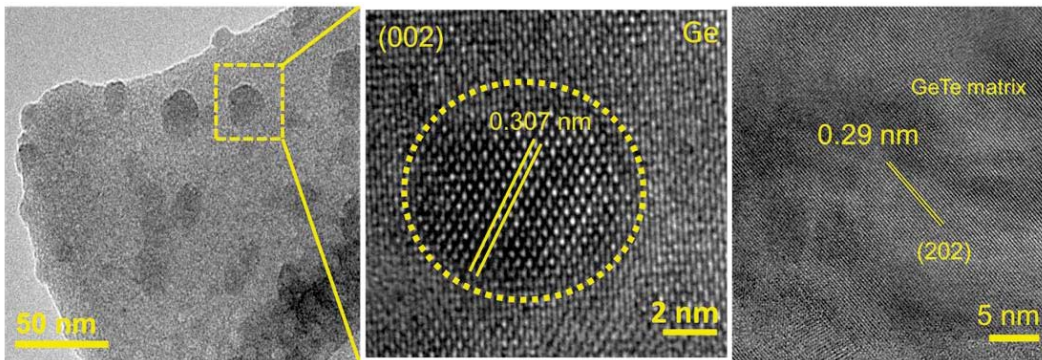


Figure 8. Low magnification TEM and HRTEM images of ball milled $\text{GPST}_{0.025}\text{Sb-0.11}$ sample.

mean free path of phonon, so they would like to contribute in effective phonon scattering and thereby decreasing κ_L .

Temperature dependent electrical conductivity curves for both ingot and ball milled samples of 10.6 % and 11 % Sb doped $\text{GPST}_{0.025}$ are shown in Figure. 9a. In the ball milled samples, electrical conductivity decreases drastically because of significant decrease in carrier concentration. $\text{GPST}_{0.025}\text{Sb-0.11}$ has σ of 580 S/cm at 300 K, which reaches to ~ 425 S/cm at 723 K, whereas in ball milled $\text{GPST}_{0.025}\text{Sb-0.11}$ σ of ~ 200 S/cm at 300 K, which increases to ~ 420 S/cm at 723 K. This increase after transition temperature can be attributed to very low band gap of the system and bipolar conduction at high temperature.

Temperature dependent Seebeck coefficients (S) of the ingot & ball milled 10.6 % and 11 % Sb doped $\text{GPST}_{0.025}$ samples are shown in Figure. 9b. Seebeck coefficients of the ball milled samples increases drastically at room temperature due the huge reduction in the carrier concentration, as for example ingot $\text{GPST}_{0.025}\text{Sb-0.11}$ shows S of ~ 128 $\mu\text{V/K}$, whereas ball milled one shows S of ~ 210 $\mu\text{V/K}$ at room temperature. We also calculated the power factor also; it came around 32 $\mu\text{W/cmK}^2$ at 723 K for the ball milled $\text{GPST}_{0.025}\text{Sb-0.11}$.

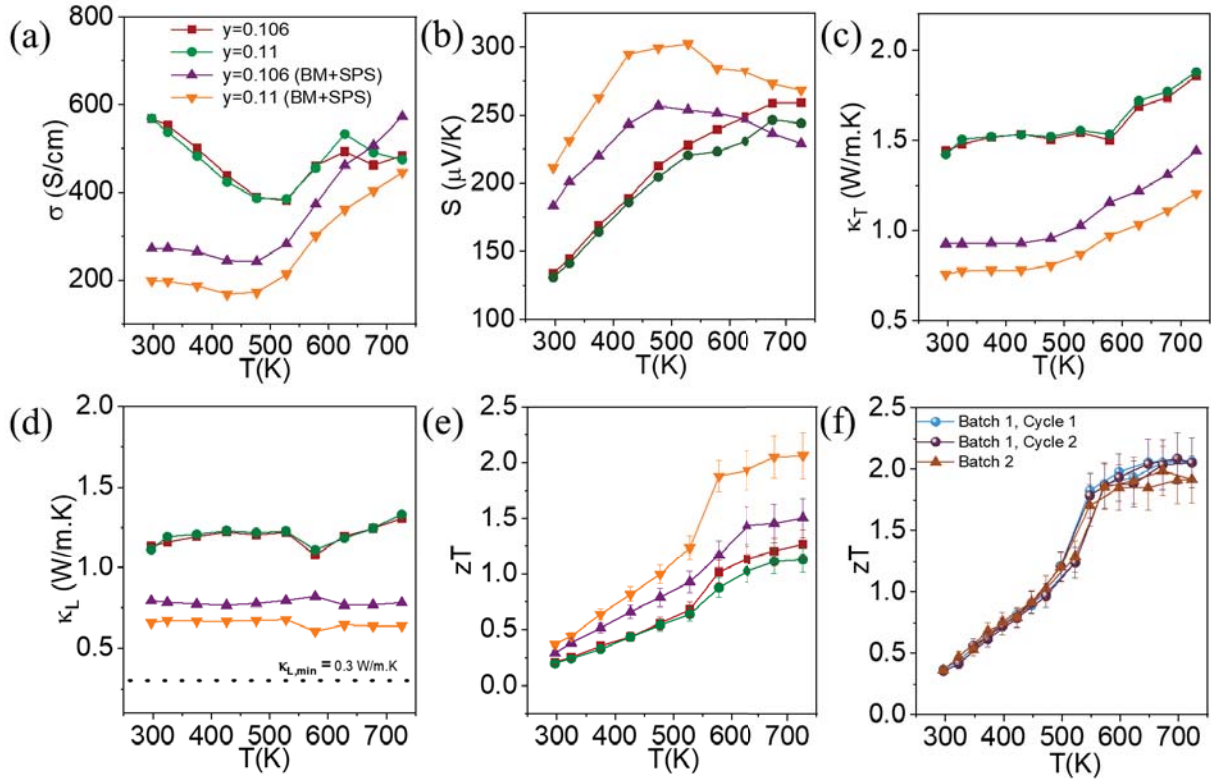


Figure 9. Temperature dependent (a) electrical conductivity (σ) and (b) Seebeck coefficient (S) (c) Total thermal conductivity (κ_T) (d) Lattice thermal conductivity (κ_L) (e) Thermoelectric figure of merit (zT) of ingot and ball milled GPST_{0.025}Sb ($y = 0.106, 0.11$) samples. (f) zT of ball milled GPST_{0.025}Sb-0.11 is reversible and reproducible over temperature cycle and batch.

κ_T as a function of temperature for ball milled GPST_{0.025}Sb ($y = 0.106$ & 0.11) samples are presented in Figure. 9c. Significant reduction in κ_T is obtained by Sb alloying in ball milled GPST_{0.025}Sb-0.11. The room temperature κ_T of ingot GPST_{0.025}Sb-0.11 is $\sim 1.4 \text{ W/mK}$, which further reduces to $\sim 0.8 \text{ W/mK}$ in ball milled sample. Figure. 9d represents the κ_L for ball milled samples. As shown in the figure ball milling in GPST_{0.025}Sb-0.11 decreases the κ_L from 1.2 W/mK to $0. \text{ W/mK}$ at 300K and reaches to $\sim 0.6 \text{ W/mK}$ at 723 K which is very close to theoretical minimum limit of 0.31 W/mK and this reduction in lattice thermal conductivity can be attributed due to mainly effective acoustic phonon scattering by Ge nanoprecipitate as observed in the TEM analysis (Figure.8).

Temperature dependent thermoelectric figure of merit (ZT) of ingot GPST_{0.025}Sb ($y=0.106, 0.11$) samples are presented in Figure. 9e. Ingot samples of 10.6% and 11% Sb doped GPST_{0.025}

exhibit zT of ~ 1.25 & 1.1 respectively at 723 K. Moreover, ball milled $\text{GPST}_{0.025}\text{Sb-0.106}$ and $\text{GPST}_{0.025}\text{Sb-0.11}$ sample exhibit significantly high ZT of ~ 1.8 & 2.1 at 723 K respectively as shown in Figure. 9e.

This enhancement of ZT of ball milled sample $\text{GPST}_{0.025}\text{Sb-0.11}$ is attributed to the significant reduction of lattice thermal conductivity and total thermal conductivity and enhancement of seebeck coefficient compared to pristine GeTe . ZT of ball milled $\text{GPST}_{0.025}\text{Sb-0.11}$ shows reversibility and reproducibility after two heating-cooling cycle and after making one other batch also (Figure.9e, 9f).

Motivated by high zT , we have studied the power conversion characteristics of the fabricated single leg device of ball milled $\text{GPST}_{0.025}\text{Sb-0.11}$ sample using Fe powder as diffusion barrier and Cu strip as contact layers. Figure.11a shows the variation of open circuit voltage (V_0) as a function of temperature difference (ΔT). V_0 increases with increase in ΔT as due to the increase in the seebeck coefficient as reaches a maximum value of 96mV at 434K . The output power (P_0) of the device as a function of measured current (I_{meas}) at a particular ΔT is shown in Figure 11b. The output power increases with increasing ΔT and reaches to maximum power (P_{max}) when the

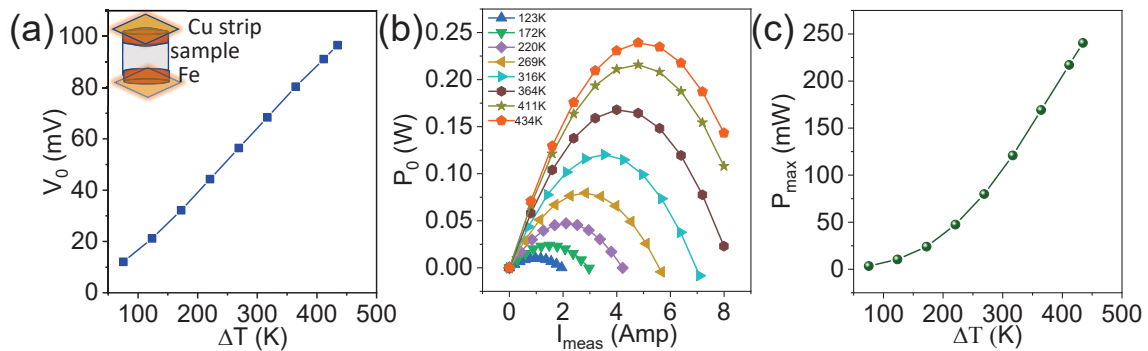


Figure 11. (a) Open circuit voltage (V_0) of single leg ball milled $\text{GPST}_{0.025}\text{Sb-0.11}$ as a function of ΔT , Cold side twmp: 298K , (b) Output power (P_0) as a function of measured current (I_{meas}) at different ΔT , (c) maximum obtainable power as a function of ΔT for single leg ball milled $\text{GPST}_{0.025}\text{Sb-0.11}$.

external resistance matches with the internal resistance of the ball milled GPST_{0.025}Sb-0.11 thermoelement. Figure 11c shows P_{\max} as a function of ΔT and the device shows a high $P_{\max} \sim 240\text{mW}$ at $\Delta T=434\text{ K}$, which make the system as an efficient mid temperature power generation material.

2.1.4. Conclusions.

We have achieved low thermal conductivity and high seebeck coefficient resulting very high thermoelectric figure of merit (~ 2.1 at 723K) in ball milled Sb doped pseudoternary $\text{Ge}_{1-2x}\text{Pb}_x\text{Sn}_x\text{Te}$ (GPST) system through three step approach. To reduce the complexity of the composition, we have limited our study to GeTe system with equimolar composition of PbTe and SnTe. A 11 mol % Sb doped ball milled $(\text{Ge}_{0.89}\text{Te})_{0.95}(\text{PbTe})_{0.025}(\text{SnTe})_{0.025}$ (GPST_{0.025}) exhibits a very low lattice thermal conductivity $\sim 0.6\text{ w/mK}$ at room temperature where phonons scattering mainly occurs due to presence of Ge nano precipitate as well as for lattice strain and mass fluctuations in the pseudoternary $\text{Ge}_{1-2x}\text{Pb}_x\text{Sn}_x\text{Te}$ system. We also achieved a high output power of $\sim 240\text{mW}$ at $\Delta T=434\text{ K}$ in a single leg device, making it as a potential mid temperature power generation material.

2.1.5. References.

1. Biswas, K.; He, J.; Blum, I. D.; Wu, C.-I.; Hogan, T. P.; Seidman, D. N.; Dravid, V. P.; Kanatzidis, M. G., High-performance bulk thermoelectrics with all-scale hierarchical architectures. *Nature* **2012**, *489* (7416), 414-418.
2. Hsu, K. F.; Loo, S.; Guo, F.; Chen, W.; Dyck, J. S.; Uher, C.; Hogan, T.; Polychroniadis, E.; Kanatzidis, M. G., Cubic AgPbmSbTe_{2+m}: bulk thermoelectric materials with high figure of merit. *Science* **2004**, *303* (5659), 818-821.
3. Zheng, Y.; Zhang, Q.; Su, X.; Xie, H.; Shu, S.; Chen, T.; Tan, G.; Yan, Y.; Tang, X.; Uher, C., Mechanically robust BiSbTe alloys with superior thermoelectric performance: a case study of stable hierarchical nanostructured thermoelectric materials. *Adv. Energy Mater.* **2015**, *5* (5), 1401391.
4. Johnsen, S.; He, J.; Androulakis, J.; Dravid, V. P.; Todorov, I.; Chung, D. Y.; Kanatzidis, M. G., Nanostructures boost the thermoelectric performance of PbS. *J. Am. Chem. Soc.* **2011**, *133* (10), 3460-3470.
5. Perumal, S.; Roychowdhury, S.; Biswas, K., High performance thermoelectric materials and devices based on GeTe. *J. Mater. Chem. C* **2016**, *4* (32), 7520-7536.
6. Liu, W. D.; Wang, D. Z.; Liu, Q.; Zhou, W.; Shao, Z.; Chen, Z. G., High-performance GeTe-based thermoelectrics: from materials to devices. *Adv. Energy Mater.* **2020**, *10* (19), 2000367.
7. Roychowdhury, S.; Samanta, M.; Perumal, S.; Biswas, K., Germanium chalcogenide thermoelectrics: electronic structure modulation and low lattice thermal conductivity. *Chem. Mater.* **2018**, *30* (17), 5799-5813.
8. Polking, M. J.; Han, M.-G.; Yourdkhani, A.; Petkov, V.; Kisielowski, C. F.; Volkov, V. V.; Zhu, Y.; Caruntu, G.; Alivisatos, A. P.; Ramesh, R., Ferroelectric order in individual nanometre-scale crystals. *Nat. Mater.* **2012**, *11* (8), 700-709.
9. Christakudi, T. A.; Plachkova, S. K.; Christakudis, G. C., Thermoelectric power of (GeTe)_{1-x}(Bi₂Te₃)_x solid solutions (0 ≤ x ≤ 0.05) in the temperature interval 80 to 350 K. *physica status solidi (a)* **1995**, *147* (1), 211-220.
10. Levin, E.; Besser, M.; Hanus, R., Electronic and thermal transport in GeTe: A versatile base for thermoelectric materials. *Journal of Applied Physics* **2013**, *114* (8), 083713
11. Li, J.; Zhang, X.; Chen, Z.; Lin, S.; Li, W.; Shen, J.; Witting, I. T.; Faghaninia, A.; Chen, Y.; Jain, A., Low-symmetry rhombohedral GeTe thermoelectrics. *Joule* **2018**, *2* (5), 976-987.
12. Samanta, M.; Roychowdhury, S.; Ghatak, J.; Perumal, S.; Biswas, K., Ultrahigh average thermoelectric figure of merit, low lattice thermal conductivity and enhanced microhardness in nanostructured (GeTe)_x(AgSbSe₂)_{100-x}. *Chem. Eur. J.* **2017**, *23* (31), 7438-7443.

13. Korkosz, R. J.; Chasapis, T. C.; Lo, S.-h.; Doak, J. W.; Kim, Y. J.; Wu, C.-I.; Hatzikraniotis, E.; Hogan, T. P.; Seidman, D. N.; Wolverton, C., High ZT in p-Type $(\text{PbTe})_{1-2x}(\text{PbSe})_x(\text{PbS})_x$ thermoelectric materials. *J. Am. Chem. Soc.* **2014**, *136* (8), 3225-3237.
14. Roychowdhury, S.; Biswas, R. K.; Dutta, M.; Pati, S. K.; Biswas, K., Phonon Localization and Entropy-Driven Point Defects Lead to Ultralow Thermal Conductivity and Enhanced Thermoelectric Performance in $(\text{SnTe})_{1-2x}(\text{SnSe})_x(\text{SnS})_x$. *ACS Energy Lett.* **2019**, *4* (7), 1658-1662.
15. Samanta, M.; Biswas, K., Low thermal conductivity and high thermoelectric performance in $(\text{GeTe})_{1-2x}(\text{GeSe})_x(\text{GeS})_x$: competition between solid solution and phase separation. *J. Am. Chem. Soc.* **2017**, *139* (27), 9382-9391.
16. Acharyya, P.; Roychowdhury, S.; Samanta, M.; Biswas, K., Ultralow Thermal Conductivity, Enhanced Mechanical Stability, and High Thermoelectric Performance in $(\text{GeTe})_{1-2x}(\text{SnSe})_x(\text{SnS})_x$. *J. Am. Chem. Soc.* **2020**, *142* (48), 20502-20508.
17. Hong, M.; Lyv, W.; Li, M.; Xu, S.; Sun, Q.; Zou, J.; Chen, Z. G., Rashba Effect Maximizes Thermoelectric Performance of GeTe Derivatives. *Joule* **2020**, *4*, 2030.
18. Lee, S.; Esfarjani, K.; Luo, T.; Zhou, J.; Tian, Z.; Chen, G., Resonant bonding leads to low lattice thermal conductivity. *Nat. Commun.* **2014**, *5* (1), 1-8.
19. Perumal, S.; Roychowdhury, S.; Negi, D. S.; Datta, R.; Biswas, K., High thermoelectric performance and enhanced mechanical stability of p-type $\text{Ge}_{1-x}\text{Sb}_x\text{Te}$. *Chem. Mater.* **2015**, *27* (20), 7171-7178
20. Wu, D.; Zhao, L.-D.; Hao, S.; Jiang, Q.; Zheng, F.; Doak, J. W.; Wu, H.; Chi, H.; Gelbstein, Y.; Uher, C., Origin of the high performance in GeTe-based thermoelectric materials upon Bi_2Te_3 doping. *J. Am. Chem. Soc.* **2014**, *136* (32), 11412-11419.

Chapter 2.2

Complementary co-doping of Sn and Bi Leads to Enhanced Thermoelectric Figure of Merit in GeTe

Chapter 2.2

Complementary co-doping of Sn and Bi Leads to Enhanced Thermoelectric Figure of Merit in GeTe

Summary

Thermoelectric material has emerged with great importance for energy harvesting technology due to its ability of converting waste heat to electrical energy. For long time Pb-based solid state materials have proven as champion thermoelectric materials for thermoelectric power generation. Recently, Pb-free GeTe derivatives have drawn great attention but higher lattice thermal conductivity (κ_L) of pristine GeTe limits its large-scale application. The optimization of thermoelectric figure of merit (zT) is essential to improve its low Seebeck coefficient (S) and to diminish its high thermal conductivity (κ_T). In this work our aim is to amplify the zT value by co-doping Sn and Bi in GeTe system. In this chapter, we have demonstrated the reduction of κ_L of ball milled and SPS processed $Ge_{0.91}Sn_{0.03}Bi_{0.06}Te$ very near to its κ_{min} . Initially, the addition of 3 mol % Sn and 6 mol % Bi in the GeTe reduces the κ_L by optimizing the p type carrier concentration and effective phonon scattering owing to excess point defects. In the second step, ball milled and SPS were performed on the optimized $Ge_{0.91}Sn_{0.03}Bi_{0.06}Te$, resulting very low κ_L of 0.57 W/m.K at exhibiting high TE figure of merit (zT) of ~ 1.9 at 623 K.

2.2.1. Introduction.

Group IV-VI metal telluride (GeTe, SnTe, and PbTe) are promising TE materials in the mid-temperature range (600-900 K). Among them PbTe exhibits high TE efficiency but the toxicity of Pb limits their large-scale application and mass market utilization. In recent years, GeTe a Pb-free chalcogenides, an alternative of PbTe (although known from 1960s, for instance TAGS-x) exhibits superb TE performance and has emerged as a potential candidate for thermoelectric power generation application.^{1, 2} GeTe undergoes phase transition from low temperature rhombohedral (α -GeTe) phase to high temperature more symmetrical cubic (β -GeTe) phase at 700 K.³ Pristine GeTe exhibits excess p-type carrier density (10^{20} cm^{-3}) because of the existence of intrinsic Ge vacancies which gives a high σ value ($\sim 8062 \text{ S/cm}$), low S ($31.5 \mu\text{V/K}$) and high thermal conductivity ($\sim 7.8 \text{ W/m.K}$) at room temperature.³ As a result, GeTe exhibits very poor TE performance at room temperature and maximum zT is ~ 0.89 at 723 K. Consequently, the fundamental requirement to achieve high TE performance is to boost the Seebeck coefficient and reduce the κ_L . The Seebeck coefficient can be improved via valance band convergence, slight symmetry reduction, Rashba effect, and formation of resonance level near fermi level.⁴⁻⁶ Whereas lattice contribution in κ can be suppressed via solid solution point defect, nano structuring which can effectively scatter the heat carrying acoustic phonon modes.^{2, 7}

The iso-valent doping in Ge site in GeTe are effective to improve the TE performance. Recent studies show that doping iso-valent transition metals like Cd, Mg, Mn, Zn, Pb, etc. ions in GeTe systems leads to the high TE performances mostly due to band alignment.^{5, 8-11} For instance, Zhi-Gang Chen group in 2020 reported Rashba Spin Splitting in GeTe based materials doped with Sn^{2+} which leads to band convergence and a high power factor.¹² Besides, Sn(II) acts as a donar dopant to GeTe system, resulting optimization of the p type carrier concentration in GeTe. On the other hand, Substitution of Bi in GeTe system is well known for low lattice thermal conductivity of $\sim 1 \text{ W/m.K}$. due to enhanced phonon scattering by solid solution point defects for $\text{Bi} < 6 \%$.^{13, 14} Even, for $> 10 \text{ mol\%}$ Bi concentration, κ_L decreases significantly due to formation of Bi_2Te_3 nano precipitates¹⁴ Therefore Sn and Bi show complimentary effect for enhancement of thermoelectric performance of GeTe. Thus, co-doping GeTe with Sn and Bi may synergistically improve the overall thermoelectric performance due to their complimentary effects. Furthermore, for practical applicatory purposes, it is also important to fabricate a device for room temperature power generation application.

Herein, we demonstrate a significantly high thermoelectric performance in Bi and Sn co-doped GeTe, ascribed to distinct but complementary roles of Sn and Bi in terms of modulating the electronic structure and scattering of heat-carrying phonons via two step strategies. Firstly, Sn (3, 5, 8 mol%) alloying create point defects in GeTe system, leading to the reduction of κ_L due to phonon scattering. In the second stage, Bi alloying in $\text{Ge}_{1-x}\text{Sn}_x\text{Te}$ again leads to a decrease in κ_L due to enhanced phonon scattering and optimized the p -type carrier concentration. Finally, to further decrease the κ_L of the optimized $\text{Ge}_{0.91}\text{Sn}_{0.03}\text{Bi}_{0.06}\text{Te}$, ingot sample was processed by Ball milling (BM) and Spark plasma sintering (SPS). This leads to significant reduction of κ_L to 0.57 W/m.K at 523K due to excess solid solution point defects. Consequently, high zT of ~ 1.9 is achieved at 623 K. for ball milled and SPS processed $\text{Ge}_{0.91}\text{Sn}_{0.03}\text{Bi}_{0.06}\text{Te}$, which is reversible and reproducible over two heating-cooling cycle and new batch also.

2.2.2. Methods.

Reagents: For the synthesis highly pure germanium (Ge, Strategic Metal Investments Ltd., 99.999%), bismuth (Bi, SRL chemical, 99.5%), tin (Sn, 99.9%, Sigma-Aldrich) and tellurium (Te, Strategic Metal Investments Ltd., 99.99%) were used without any additional purifications.

Synthesis: Starting elements of Ge, Bi, Sn and Te in stoichiometric proportions were taken for the preparation of high-quality polycrystalline sample $\text{Ge}_{1-x-y}\text{Bi}_y\text{Sn}_x\text{Te}$ ($x = 0.03, 0.05, 0.07$ $y = 0.04, 0.06, 0.08$). At first, appropriate amount of starting materials were weighted and taken in carbon coated quartz tubes. The tubes were sealed under high vacuum (10^{-5} Torr) and placed in the furnace. Then these tubes were slowly heated up to 950 °C over 12 hr., dwelled at 6 hr., and finally cooled down to the room temperature over 12 h. After that the ingot samples were collected, cut into coins (10 mm x 2.5 mm) and bars (~ 2 mm x 2 mm x 8 mm) and polished for thermal and electrical transport property measurements.

Powder X-ray diffraction (PXRD): The samples were finely grinded and room temperature PXRD data was performed on Rigaku smart Lab SE diffractometer using Cu $K\alpha$ radiation ($\lambda = 1.5406$ Å).

Band Gap: The optical band gap of all the powdered samples were measured using the diffuse reflectance mode in an FT-IR Bruker IFS 66 V/S spectrometer in the Near-IR range.

Absorption (α/S) values were calculated by using Kubelka-Munk equation: $\alpha/S = (1-R)^2/(2R)$, where α , S and R are the absorption, scattering coefficient and reflectance respectively.

Field emission scanning electron microscopy (FESEM): ZEISS Gemini field Emission Scanning Electron Microscope was used for imaging, energy dispersive X-ray analysis and elemental colour mapping.

Electrical transport properties: ULVAC-RIKO ZEM-3 instrument was used to measure electrical conductivity (σ) and Seebeck coefficient (S) simultaneously under He-atmosphere in the temperature range from 290-723 K. For the measurement rectangular bar samples of dimension 8 mm \times 2 mm \times 2mm were used.

Thermal transport properties: Netzsch LFA-457 instrument was used for the measurement of thermal diffusivity (D) between the temperature range from 290 K to 723 K applying laser flash diffusivity technique. For that purpose, a coin shaped pellets with 10 mm diameter and 2.5 mm thickness were used. Temperature dependent heat capacity of GeTe was derived using pyroceram as standard sample in LFA-457. The estimation of total thermal conductivity was done using the relation $k = D \times C_p \times \rho$; where ρ is the density and C_p is the heat capacity of pristine GeTe. Density of all the samples used is greater than 96%.

Hall measurement: The hall measurement of all the samples were done in home build set up under varying magnetic field of 0.0 – 1.0 T in 90 mA current at room temperature.

2.2.3. Results and discussion.

Synthesis of $\text{Ge}_{1-x-y}\text{Bi}_y\text{Sn}_x\text{Te}$ ($x = 0.03, 0.05, 0.08$ $y = 0.04, 0.06, 0.08$). samples were performed by using vacuum seal tube reaction and their crystal structures were initially elucidated by using PXRD. All the peaks present in the PXRD pattern (Figure 1a) could be matched with the PXRD pattern of rhombohedral structure ($\alpha\text{-GeTe}$, space group $R3m$) without any detection of impurity peak of Sn and Bi. After Sn doping the the highest intense peak at $2\theta = 29.88^\circ$ shifts towards the lower angle as shown in figure 1a (insight) compared to pristine GeTe because of the substitution of smaller Ge^{2+} (ionic radius: 87 pm) ion by larger Sn^{2+} (ionic radius: 118 pm) ion. The highly intense PXRD peak of all Sn and Bi co-doped GeTe composites also shifted to the lower angle with increase in the concentration of Bi suggesting that small Ge atom is replaced by larger Sn and Bi atom (Figure 1b). Figure 1c shows the change of electronic absorption spectra of $\text{Ge}_{1-x}\text{Sn}_x\text{Te}$ ($x = 0.03, 0.05, 0.08$) with respect to energy (E_g).

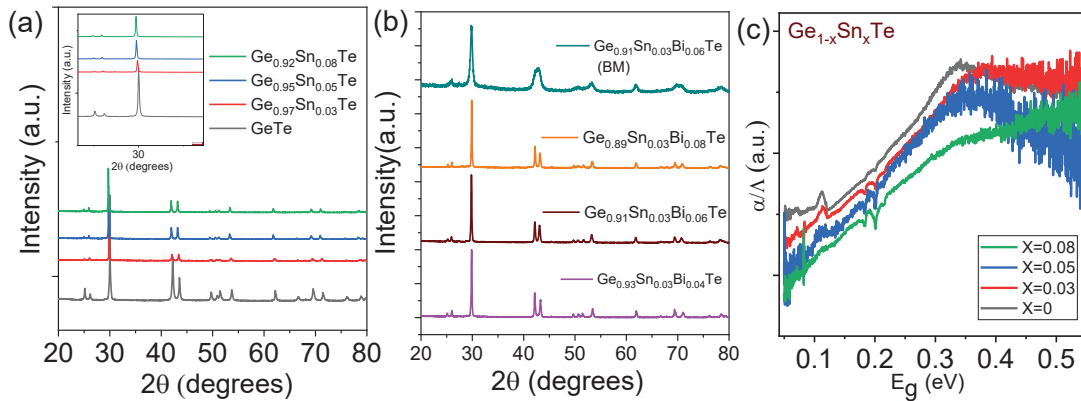


Figure 1. (a) PXRD pattern of $\text{Ge}_{1-x}\text{Sn}_x\text{Te}$ ($x = 0.03, 0.05, 0.08$) samples. (b) Powder XRD pattern of $\text{Ge}_{1-x-y}\text{Sn}_x\text{Bi}_y\text{Te}$ ($x = 0.03$; $y = 0.04$ to 0.08). (d) Electronic absorption spectra of $\text{Ge}_{1-x}\text{Sn}_x\text{Te}$ samples ($x = 0.03, 0.05, 0.08$).

In pristine GeTe the less electronegative Ge (2.01, Pauling scale) orbital contributes the conduction band minima whereas the more electronegative Te (2.1, Pauling scale) orbital constitutes valance band maxima. After doping of Sn into the GeTe system due to less electronegativity of Sn (1.96, Pauling scale) opening of band gap occurs, resulting gradual increase in band gap. Figure 2a represents the temperature dependent electrical conductivity (σ) of

$\text{Ge}_{1-x}\text{Sn}_x\text{Te}$ ($x = 0$ to 0.08) The electrical conductivity of all GeTe composite decreases with increasing temperature, signifying the degenerate semiconducting nature.¹⁵ Pristine GeTe

exhibits σ value ~ 8062 S/cm at 298 K whereas the value reduces to ~ 2137 S/cm at 709 K (Figure 2a). In case of Sn doping significant reduction in electrical conductivity (~ 5800 S/cm at room temperature for 3% Sn doped GeTe) occurs, which can be attributed to decrease in carrier concentration. Again, in Sn and Bi co-doped GeTe samples show considerably reduction in electrical conductivity value (Figure 2d).

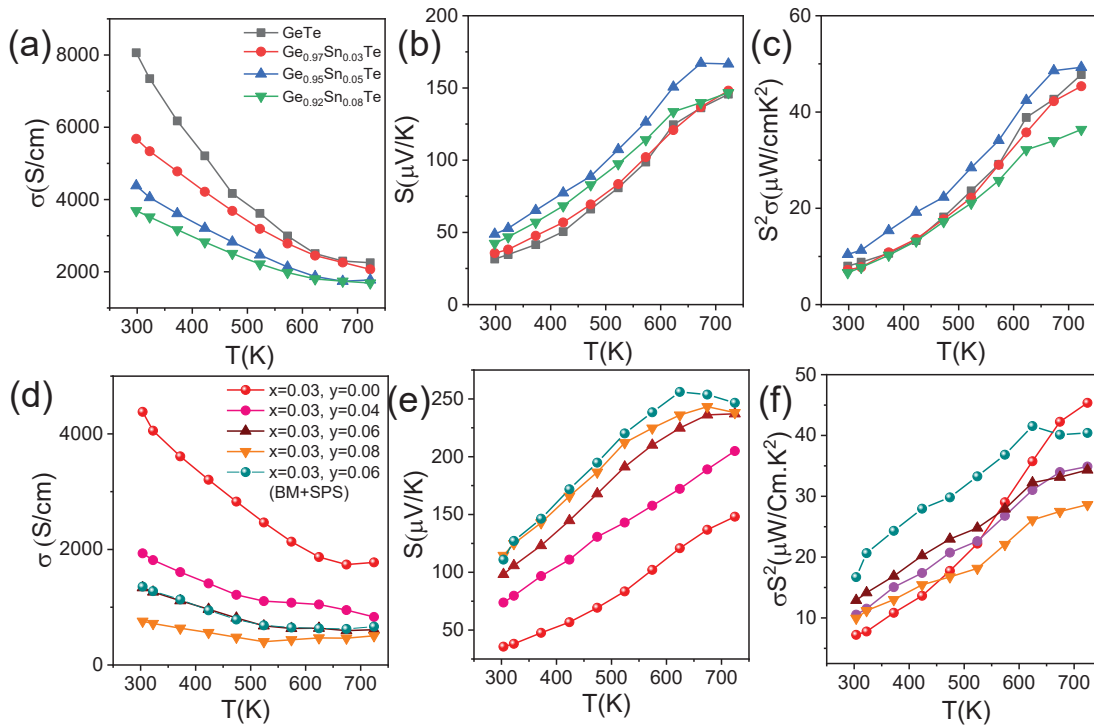


Figure 2. Temperature dependent (a) electrical conductivity (σ), (b) Seebeck coefficient (S), and (c) power factor (σS^2) of Ge_{1-x}Sn_xTe ($x = 0$ to 0.08) samples. Temperature dependent (d) electrical conductivity (σ) (e) Seebeck coefficient (S) and (f) power factor (σS^2) of Ge_{1-x-y}Sn_xBi_yTe ($x = 0.03$; $y = 0.04$ to 0.08)

This is due to the donor dopant nature of Bi³⁺ at Ge sites. The temperature dependent σ value was reduced from ~ 8062 S/cm in GeTe to ~ 1330 S/cm in Ge_{0.91}Bi_{0.06}Sn_{0.03}Te at room temperature. The decrease of σ value may occur due to the reduction of carrier concentration which is supported by the hall measurement data. The p-type carrier density (n) decreases from $8.6 \times 10^{20}/\text{cm}^3$ in pristine GeTe to $3.12 \times 10^{19}/\text{cm}^3$, $2.18 \times 10^{19}/\text{cm}^3$, $1.69 \times 10^{19}/\text{cm}^3$ in Ge_{0.93}Bi_{0.04}Sn_{0.03}Te, Ge_{0.91}Bi_{0.06}Sn_{0.03}Te and Ge_{0.89}Bi_{0.08}Sn_{0.03}Te respectively. The suppression of hole carrier concentration (n) is mainly due to the presence of excess electron in the system obtained from the replacement of Ge²⁺ by Bi³⁺. In addition to that, ball mill and SPS processed Ge_{0.91}Bi_{0.06}Sn_{0.03}Te sample exhibits σ of ~ 1356 S/cm same as that of the ingot one.

The Seebeck coefficient (S) of $\text{Ge}_{1-x-y}\text{Bi}_y\text{Sn}_x\text{Te}$ ($x = 0, 0.03$ and $y = 0.04$ to 0.08) composites increase with increase in temperature, as represented in Figure 2b and 2e. The S value of pristine GeTe rises from $\sim 32 \mu\text{V/K}$ at 298 K to $\sim 153 \mu\text{V/K}$ at 723 K . The positive value of S of all the samples indicates that the p-type carrier density is present in GeTe alloy materials, supporting by Hall coefficient data also. 5 mol% of Sn doping in GeTe shows that the S increases from $\sim 50 \mu\text{V/K}$ at 298 K to $\sim 165 \mu\text{V/K}$ at 720 K (Figure 2b). Upon Bi doping in Sn doped GeTe system the S value further increases. The S value of $\text{Ge}_{0.97}\text{Sn}_{0.03}\text{Te}$ is $\sim 36 \mu\text{V/K}$ at 298 K which increases with increase in the concentration of Bi such as $\sim 74 \mu\text{V/K}$, $\sim 98 \mu\text{V/K}$, and $\sim 114 \mu\text{V/K}$ for $\text{Ge}_{0.93}\text{Bi}_{0.04}\text{Sn}_{0.03}\text{Te}$, $\text{Ge}_{0.91}\text{Bi}_{0.06}\text{Sn}_{0.03}\text{Te}$, and $\text{Ge}_{0.89}\text{Bi}_{0.08}\text{Sn}_{0.03}\text{Te}$ respectively at 300 K ,

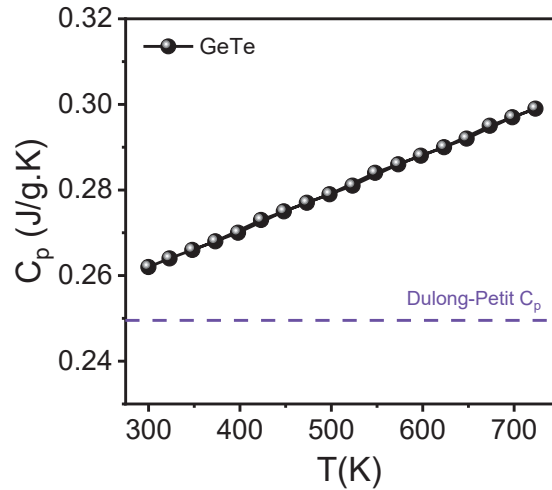


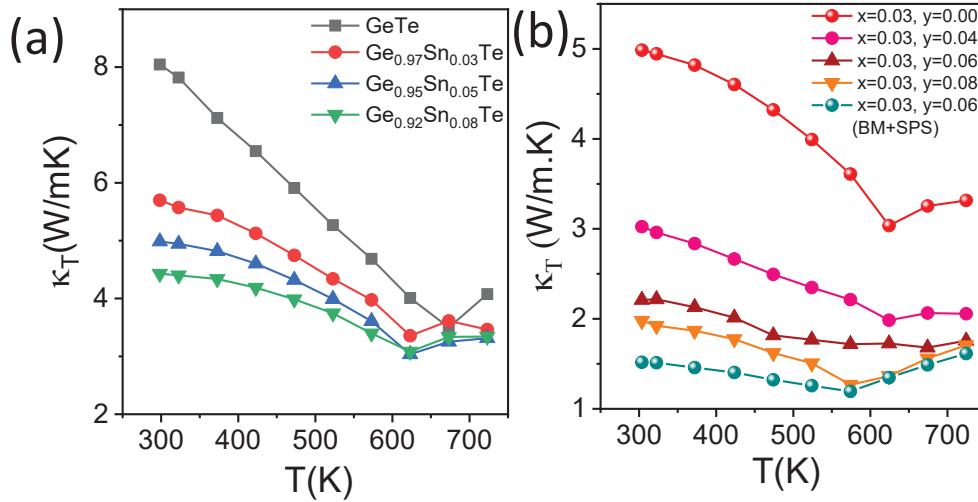
Figure 3. Temperature-dependent specific heat capacity of GeTe.

whereas, in the ball milled and SPS processed $\text{Ge}_{0.91}\text{Bi}_{0.06}\text{Sn}_{0.03}\text{Te}$, S value increases from $\sim 111 \mu\text{V/K}$ at room temperature to $\sim 246 \mu\text{V/K}$ at 723 K . In case of Bi doping, the enhancement of S occurs due to the suppression of carrier concentration. A higher concentration of Bi doping shows the bipolar conduction in Seebeck data at higher temperature.

Figure 2c and 2f show that the power factor (σS^2) value increases with the temperature. Typically, undoped GeTe shows σS^2 of $\sim 8 \mu\text{W/cm. K}^2$ at room temperature and reaches to $\sim 49 \mu\text{W/cm. K}^2$ at 723 K . Whereas, for 5 mol% Sn doped GeTe alloy the power factor tends to increase from $\sim 10 \mu\text{W/cm. K}^2$ at 298 K and reaches a maximum value of $\sim 50 \mu\text{W/cm. K}^2$ at 723 K . The σS^2 value of Sn doped GeTe samples increases with increase in Bi concentration at room temperature. Sn and Bi co-doped GeTe samples reveal a power factor $11 \mu\text{W/cm. K}^2$, $13 \mu\text{W/cm. K}^2$, and $10 \mu\text{W/cm. K}^2$ at 300 K in $\text{Ge}_{0.93}\text{Bi}_{0.04}\text{Sn}_{0.03}\text{Te}$, $\text{Ge}_{0.91}\text{Bi}_{0.06}\text{Sn}_{0.03}\text{Te}$, and

$\text{Ge}_{0.89}\text{Bi}_{0.08}\text{Sn}_{0.03}\text{Te}$ respectively, while ball milled $\text{Ge}_{0.91}\text{Bi}_{0.06}\text{Sn}_{0.03}\text{Te}$ sample exhibits a very high-power factor of $\sim 40 \mu\text{W}/\text{cm} \cdot \text{K}^2$ of at 723K, which is solely attributed to the enhanced seebeck coefficient of that sample.

Diffusivity (D) decreases significantly for $\text{Ge}_{1-x}\text{Sn}_x\text{Te}$ ($x = 0$ to 0.08) $\text{Ge}_{1-x-y}\text{Bi}_y\text{Sn}_x\text{Te}$ ($x = 0.03$ and $y = 0.04$ to 0.08) compounds and consequently the κ_T value also decreases. From Figure 4a and 4b the decrease of total thermal conductivity (κ_T) upon rising temperature was



observed **Figure 4**. Temperature dependent total thermal conductivity (κ_T) of (a) $\text{Ge}_{1-x}\text{Sn}_x\text{Te}$ ($x = 0$ to 0.08). (b) $\text{Ge}_{1-x-y}\text{Sn}_x\text{Bi}_y\text{Te}$ ($x = 0.03$; $y = 0.04$ to 0.08) samples.

due to Umklapp scattering which is a typical behavior of crystalline materials. The (κ_T) value of pristine GeTe is 7.9 W/m.K at 298K and which reduces to 3.9 W/m.K at 723 K. In case of Sn doped GeTe the reduction of total thermal conductivity occurs mainly due to solid solution point defects which decreases lattice thermal conductivity by increasing phonon scattering.

The pristine GeTe exhibits κ_T value 7.9 W/m.K at 298 K whereas the 3 mol % Sn doped GeTe shows κ_T of 4.9 W/m.K at 298 K. Sn and Bi co-doped GeTe composites further display the lowering of κ_T value due the further increase of point defects concentration. For the composition $\text{Ge}_{0.91}\text{Bi}_{0.06}\text{Sn}_{0.03}\text{Te}$ the κ_T value starts from 2.25 W/m.K at 298 K and reaches to a lowest value of 1.7 W/m.K at 723 K, whereas, in the ball milled sample, further reduction of κ_T occurs at room temperature as shown in figure 4b.

The temperature dependence electrical thermal conductivity (κ_e) of $\text{Ge}_{1-x}\text{Sn}_x\text{Te}$ ($x = 0$

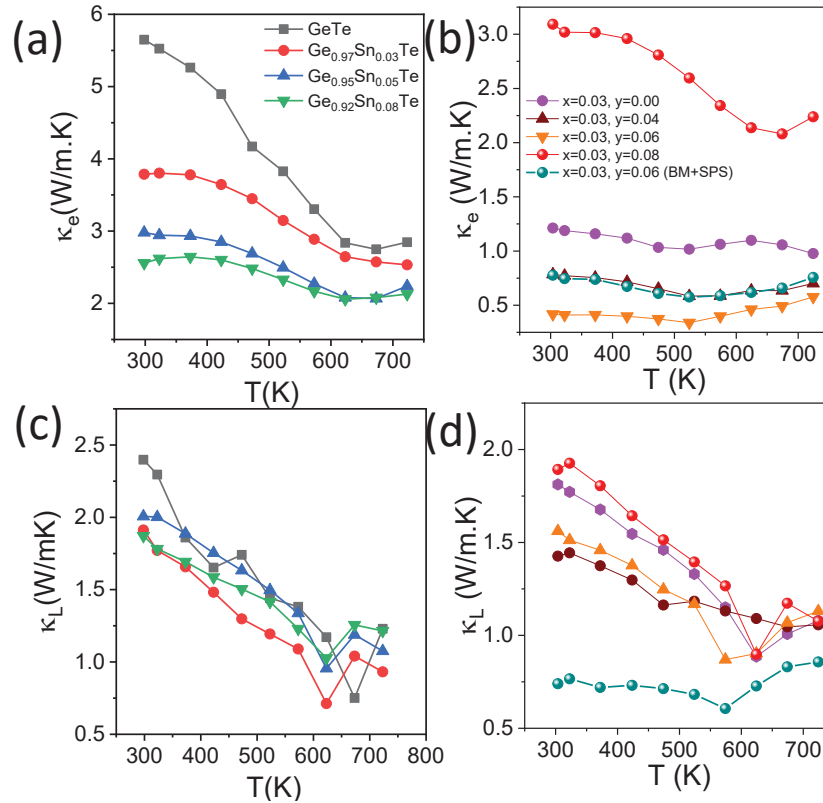


Figure 5. Temperature dependent electrical thermal conductivity (κ_e) of (a) $\text{Ge}_{1-x}\text{Sn}_x\text{Te}$ ($x = 0$ to 0.08), and (b) $\text{Ge}_{1-x-y}\text{Bi}_y\text{Sn}_x\text{Te}$ ($x = 0.03$ and $y = 0.04$ to 0.08) Temperature dependent lattice thermal conductivity (κ_L) of (c) $\text{Ge}_{1-x}\text{Sn}_x\text{Te}$ ($x = 0$ to 0.08), and (d) $\text{Ge}_{1-x-y}\text{Bi}_y\text{Sn}_x\text{Te}$ ($x = 0.03$ and $y = 0.04$ to 0.08)

to 0.08) and $\text{Ge}_{1-x-y}\text{Bi}_y\text{Sn}_x\text{Te}$ ($x = 0.03$ and $y = 0.04$ to 0.08) samples are shown in Figure 5a and 5b. The κ_e is calculated from Wiedemann-Franz law ($\kappa_{\text{ele}} = L\sigma T$), where L is the Lorenz factor. The κ_e value of GeTe is 5.6 W/m.K at 298 K. Sn and Bi co-doping in GeTe diminish the hole concentration thus decreases the contribution of κ_e to total thermal conductivity. Both the ingot and ball milled $\text{Ge}_{0.91}\text{Bi}_{0.06}\text{Sn}_{0.03}\text{Te}$ composites illustrate the κ_e value of ~ 0.7 W/m.K at 300 K as similar to electrical conductivity data. The lattice thermal conductivity (κ_L) is obtained by subtracting the electrical thermal conductivity (κ_e) from total thermal conductivity (κ_T). The κ_L value of pristine GeTe remains 2. W/m.K at 298 K and decreases with increasing temperature (Figure 5c). Above 660 K lattice thermal conductivity again tends to increase. This is mainly due to the orientation of soft optical phonon modes near the phase transition temperature which permits the scattering of heat carrying acoustic phonon.

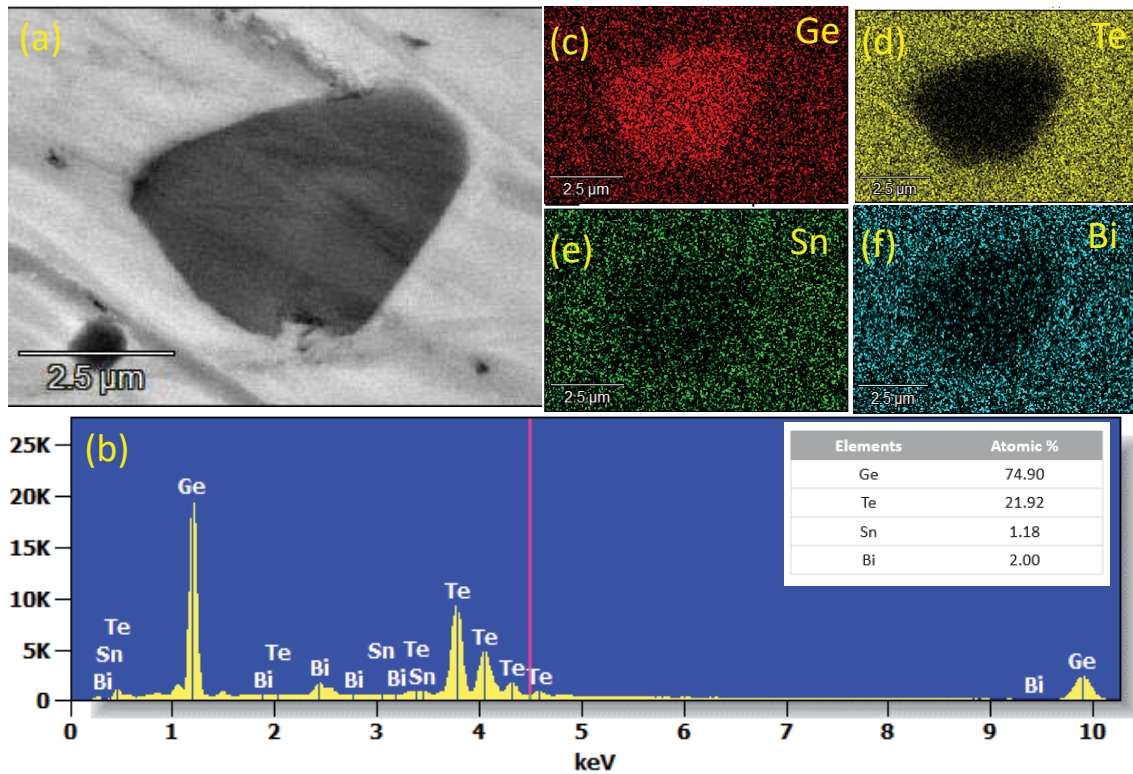


Figure 6. (a) FESEM image of ball milled $\text{Ge}_{0.91}\text{Bi}_{0.06}\text{Sn}_{0.03}\text{Te}$ with corresponding EDX spectra in (b). (c), (d), (e) and (f) displays EDX elemental colour mapping for Ge, Te, Sn, and Bi atoms, respectively for the area in (a).

Addition of 6 mol% of Bi in $\text{Ge}_{0.97}\text{Sn}_{0.03}\text{Te}$ reduces the κ_L value to ~ 1.5 W/m.K at 296 K (Figure 5d). This large reduction may be mainly ascribed to the phonon scattering obtained from solid solution point defects. Ball milled and SPS processed $\text{Ge}_{0.91}\text{Bi}_{0.06}\text{Sn}_{0.03}\text{Te}$ shows further reduction in κ_L from 0.73 W/m.K at room temperature to 0.85 W/m.K at 723K and it shows a minimum value of 0.57 W/m.K at 523K, which is very close to the theoretical minimum value of 0.3 W/m.K.

To investigate the origin of low lattice thermal conductivity and surface morphology, we have performed Transmission Electron Microscopy (TEM) and field emission scanning electron microscopy (FESEM) with energy-dispersive X-ray spectroscopy (EDAX) on ball milled and SPS processed $\text{Ge}_{0.91}\text{Bi}_{0.06}\text{Sn}_{0.03}\text{Te}$ (Figure 6a and 6b). Color mapping of the Figure 6a shows the presence of micro precipitate of Ge with ~ 5 μm size in the GeTe matrix (Figure 6c). These results indicate that the system is basically a solid solution, rich with point-defects, whereas no nanoprecipitate was observed in HRTEM, which clearly indicates that the origin

of low lattice thermal conductivity in the ball milled sample is solid solution point defects and Ge rich micro precipitates.

Figure 7a and 7b describe the variation of dimensionless thermoelectric figure of merit (zT) with the temperature. Pristine GeTe has zT of ~ 0.89 at 723 K. For only 3 mol % Sn doped system the maximum value of $zT \sim 1$ was achieved at 723 K and for 6 mol % Bi doped GeTe, zT comes around ~ 1.24 at 723K.¹⁴ Although for $\text{Ge}_{0.91}\text{Bi}_{0.06}\text{Sn}_{0.03}\text{Te}$ we have got zT of ~ 1.4 at

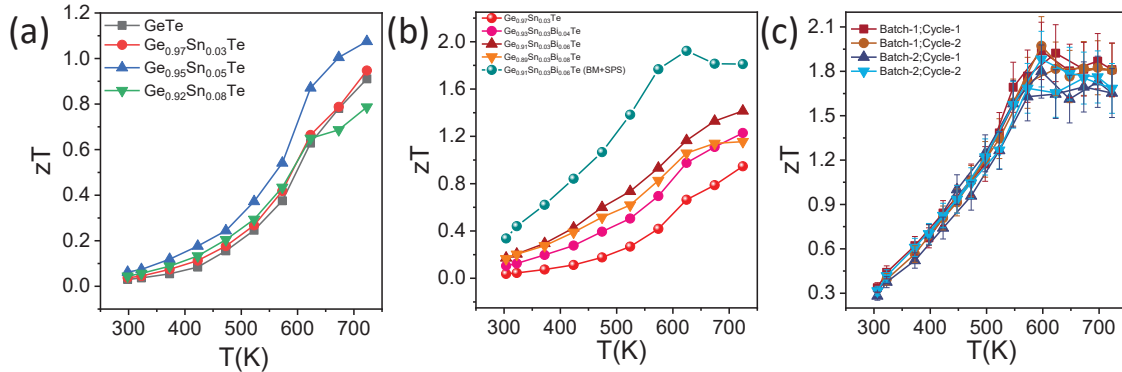


Figure 7. Temperature dependent thermoelectric figure of merit (zT) of (a) $\text{Ge}_{1-x}\text{Sn}_x\text{Te}$ ($x = 0$ to 0.08), and (b) $\text{Ge}_{1-x-y}\text{Bi}_y\text{Sn}_x\text{Te}$ ($x = 0.03$ and $y = 0.04$ to 0.08) samples. (c) zT of ball milled and SPS processed $\text{Ge}_{0.91}\text{Bi}_{0.06}\text{Sn}_{0.03}\text{Te}$ is reversible and reproducible

723 K and in the ball milled and SPS processed $\text{Ge}_{0.91}\text{Bi}_{0.06}\text{Sn}_{0.03}\text{Te}$, we have found high zT of ~ 1.9 at 623K, which is 113% higher than that of pristine GeTe and this huge increment can be attributed to the enhancement of power factor and significant reduction of the lattice thermal conductivity in the ball milled sample because of enhanced phonon scattering due to excess solid solution point defects. The zT of ball milled and SPS processed $\text{Ge}_{0.91}\text{Bi}_{0.06}\text{Sn}_{0.03}\text{Te}$ sample shows reversibility and temperature stability after two heating-cooling cycle and reproducibility in another batch also as shown in Figure. 7c.

2.2.4. Conclusion and future outlook.

We have successfully synthesized Sn and Bi co-doped GeTe sample which provides high thermoelectric performance by reducing thermal conductivity mainly due to solid solution point defects scattering. We have achieved a high zT of ~ 1.9 at ~ 623 K for ball milled and SPS processed $\text{Ge}_{0.91}\text{Bi}_{0.06}\text{Sn}_{0.03}\text{Te}$ composite which is $\sim 113\%$ higher than the pristine GeTe, which shows good reversibility and reproducibility also. In future, we will prepare single leg device

of the high zT material to check actual thermoelectric conversion efficiency and maximum power output for applications.

2.2.5. References.

1. Perumal, S.; Roychowdhury, S.; Biswas, K., High performance thermoelectric materials and devices based on GeTe. *J. Mater. Chem. C* **2016**, *4*, 7520.
2. Samanta, M.; Biswas, K., Low Thermal Conductivity and High Thermoelectric Performance in $(\text{GeTe})_{1-2x}(\text{GeSe})_x(\text{GeS})_x$: Competition between Solid Solution and Phase Separation. *J. Am. Chem. Soc.* **2017**, *139* (27), 9382-9391.
3. Perumal, S.; Roychowdhury, S.; Negi, D. S.; Datta, R.; Biswas, K., High Thermoelectric Performance and Enhanced Mechanical Stability of p-type $\text{Ge}_{1-x}\text{Sb}_x\text{Te}$. *Chem. Mater.* **2015**, *27* (20), 7171.
4. Zheng, Z.; Su, X.; Deng, R.; Stoumpos, C.; Xie, H.; Liu, W.; Yan, Y.; Hao, S.; Uher, C.; Wolverton, C.; Kanatzidis, M. G.; Tang, X., Rhombohedral to Cubic Conversion of GeTe via MnTe Alloying Leads to Ultralow Thermal Conductivity, Electronic Band Convergence, and High Thermoelectric Performance. *J. Am. Chem. Soc.* **2018**, *140*, 2673.
5. Hong, M.; Lyv, W.; Li, M.; Xu, S.; Sun, Q.; Zou, J.; Chen, Z. G., Rashba Effect Maximizes Thermoelectric Performance of GeTe Derivatives. *Joule* **2020**, *4*, 2030.
6. Perumal, S.; Samanta, M.; Ghosh, T.; Shenoy, U. S.; Bohra, A. K.; Bhattacharya, S.; Singh, A.; Waghmare, U. V.; Biswas, K., Realization of High Thermoelectric Figure of Merit in GeTe by Complementary Co-doping of Bi and In. *Joule* **2019**, *3*, 2565.
7. Roychowdhury, S.; Ghosh, T.; Arora, R.; Samanta, M.; Xie, L.; Singh, N. K.; Soni, A.; He, J.; Waghmare, U. V.; Biswas, K., Enhanced atomic ordering leads to high thermoelectric performance in AgSbTe_2 . *Science* **2021**, *371* (6530), 722.
8. Nshimiyimana, E.; Hao, S.; Su, X.; Zhang, C.; Liu, W.; Yan, Y.; Uher, C.; Wolverton, C.; Kanatzidis, M. G.; Tang, X., Discordant nature of Cd in GeTe enhances phonon scattering and improves band convergence for high thermoelectric performance. *J. Mater. Chem. A* **2020**, *8* (3), 1193-1204.
9. Xing, T.; Zhu, C.; Song, Q.; Huang, H.; Xiao, J.; Ren, D.; Shi, M.; Qiu, P.; Shi, X.; Xu, F.; Chen, L., Ultralow Lattice Thermal Conductivity and Superhigh Thermoelectric Figure-of-Merit in (Mg, Bi) Co-Doped GeTe. *Adv. Mater.* **2021**, *33* (17), 2008773.
10. Kumar, A.; Bhumla, P.; Parashchuk, T.; Baran, S.; Bhattacharya, S.; Wojciechowski, K. T., Engineering Electronic Structure and Lattice Dynamics to Achieve Enhanced Thermoelectric Performance of Mn-Sb Co-Doped GeTe. *Chem. Mater.* **2021**, *33* (10), 3611-3620.
11. Guo, Z.; Zhang, Q.; Wang, H.; Tan, X.; Shi, F.; Xiong, C.; Man, N.; Hu, H.; Liu, G.; Jiang, J., Bi-Zn codoping in GeTe synergistically enhances band convergence and phonon scattering for high thermoelectric performance. *J. Mater. Chem. A* **2020**, *8* (41), 21642-21648.

12. Hong, M.; Lyv, W.; Li, M.; Xu, S.; Sun, Q.; Zou, J.; Chen, Z.-G., Rashba effect maximizes thermoelectric performance of GeTe derivatives. *Joule* **2020**, *4* (9), 2030-2043.
13. Perumal, S.; Bellare, P.; Shenoy, U. S.; Waghmare, U. V.; Biswas, K., Low thermal conductivity and high thermoelectric performance in Sb and Bi codoped GeTe: complementary effect of band convergence and nanostructuring. *Chem. Mater.* **2017**, *29* (24), 10426-10435.
14. Perumal, S.; Roychowdhury, S.; Biswas, K., Reduction of thermal conductivity through nanostructuring enhances the thermoelectric figure of merit in Ge_{1-x}Bi_xTe. *Inorg. Chem. Front.* **2016**, *3* (1), 125-132.
15. Tan, G.; Zhao, L.-D.; Kanatzidis, M. G., Rationally designing high-performance bulk thermoelectric materials. *Chem. Rev.* **2016**, *116* (19), 12123-12149.

PART 3

**Selective and Efficient Removal of
Heavy Metals from Water by
Inorganic Layered Materials**

Chapter 3.1

Efficient Sequestration of Cd (II) from Water up to ppb Level by Layered Metal Chalcophosphate

Efficient Sequestration of Cd (II) from Water upto ppb Level by Layered Metal Chalcophosphate

Summary

Sequestration of heavy metal ions from water is an important issue in chemistry and environmental science. In this chapter, we have discussed the detailed Cd^{2+} adsorption and ion exchange kinetics in a potassium intercalated layered metal thiophosphate, $K_{0.48}Mn_{0.76}PS_3 \cdot H_2O$ (K-MPS-1). KMPS-1 is capable of efficient removal of Cd^{2+} (>99 %) from very dilute concentration (1-1100 ppb). K-MPS-1 can selectively capture Cd^{2+} even in presence of other monovalent and divalent cations such as Na^+ , Ca^{2+} , Mg^{2+} with high separation factor. K-MPS-1 can operate within a broad pH range of 1.8-11 effectively with high distribution co-efficient (K_d^{Cd}) of $\sim 10^4$ mL/g, following pseudo second order kinetics. Initially, K^+ intercalation in $MnPS_3$ (MPS-1) increases the interlayer spacing and subsequently creates a Mn^{2+} vacancy to maintain charge neutrality and destroy the center of symmetry of P_2S_6 unit. Finally, Cd^{2+} kicks out K^+ ions from the interlayer and sits into Mn^{2+} vacant sites in MPS-1 which further helps to regain the center of symmetry of the structure. K-MPS-1 has achieved Cd^{2+} removal capacity of 402.35 mg/g following Langmuir-Freundlich adsorption model. K-MPS-1 is effective to capture Cd^{2+} far below the mark of tolerance level (5 ppb, USA- EPA) of drinking water.

3.1.1. Introduction

Water is unarguably one of the most important and inevitable natural resources, but world population has reached to almost 7.9 billion, where there is just 3.5% of fresh water. Water is getting polluted by industrial hazardous, pathogens, radio nucleotides, heavy and toxic metals like Zn^{2+} , Cd^{2+} , Tl^+ , Hg^{2+} etc and those have detrimental and adverse effect on human health, plants and aquatic organisms due to bioaccumulation, toxicity and non-biodegradability.^{1,2} Cd (II) is one of such toxic, hazardous non-essential elements that naturally occur as a pollutant in the environment discharged by mainly agricultural and industrial wastes. According to epidemiological data, prolonged environmental exposure of Cd makes it act like a carcinogen affecting several parts of the human body like mostly breast, lung, prostate kidney, pancreas even the skeletal system also³Therefore before discharging Cd (II) into water streams, effective and efficient removal of Cd (II) from wastewater has become an emergent issue.

A large variety of materials has been tested for the removal of heavy and toxic metal ions like Pb^{2+} , Hg^{2+} from wastewater. The conventional methods which include membrane separation, ion exchange, chemical precipitation, flocculation is not up to the mark for removing the heavy metals in trace ppb level.⁴ One of the most cost-effective methods widely implemented for water purification is using natural adsorbent like clay, zeolites, mesoporous silica, activated charcoal, polymers, biomaterials, but they also lack strong binding affinity with metal ions, high selectivity, pH, and temperature stability.⁵⁻⁷Therefore, designing effective adsorbents for capturing the heavy metal ions has become the top precedence for the researchers for eco-governance.

Functionalizing certain inorganic layered compounds with sulfide group can make them a good heavy metal ions adsorbent as besides having porosity and high surface area, they have stronger binding affinity towards chalcogenides due to soft lewis acid-base interactions.^{8, 9}

Consequently, 3D layered metal thiophosphates have been emerged as a promising material for sequestration of heavy metals. For instance, layered metal sulfides like $K_{2x}Mn_xSn_{3-x}S_6$, $H_{2x}Mn_xSn_{3-x}S_6$, $K_{2x}Mg_xSn_{3-x}S_6$, $K_{2x}Sn_{4-x}S_{8-x}$, show high removal efficiency towards heavy metal ions.¹⁰⁻¹² Our group also has shown $K_{0.48}Mn_{0.76}PS_3 \cdot H_2O$ (KMPS-1) exhibits >90% removal of Pb^{2+} and Cs^+ in a wide pH range from water.^{13, 14}

Herein, we have demonstrated the high Cd (II) capture ability of KMPS-1 even in the presence of Pb (II) in water, and it can capture Cd (II) from trace 1 ppb. Cd sorption follows Langmuir–Freundlich adsorption isotherm with an exceptionally high maximum adsorption capacity value of 402.35 mg/g, which is relatively much higher compared to other reported adsorbents. The adsorption process reaches equilibrium within 20 mins following pseudo second order kinetics with an adsorption coefficient of 10^4 mL/g and the material (KMPS) can be regenerated again by treating Cd-MPS with saturated KCl solution, hence the re-use and recycling capability makes KMPS a promising sequestrant of Cd (II). adsorption.

3.1.2. Experimental section

Reagents. Manganese (Mn, Alfa Aesar 99.95 %), Red phosphorous (P, Alfa Aesar 98.9 %), sulphur (S, Alfa Aesar 99.999 %), Cadmium chloride, monohydrate ($CdCl_2 \cdot H_2O$), Sigma Aldrich 99.999%), and potassium chloride (KCl, Alfa Aesar 99.5 %) were used for synthesis without further purification.

Synthesis. $MnPS_3$ (MPS-1) was prepared by mixing appropriate ratio of elements Mn, P, S followed by sealing under vacuum (10^{-5} Torr) in quartz tube. The tube was slowly heated to 723 K over 12 h, then heated up to 923 K in 2 h, soaked for 144 h, and subsequently cooled to room temperature in 8h. Deep green color reported MPS-1 was obtained.⁴⁰ 1 g MPS-1 was Stirred with 50 mL 2M KCl aq. solution for 24 h at room temperature and the light green $K_{0.48}Mn_{0.76}PS_3 \cdot H_2O$

(K-MPS-1) was separated by centrifugation⁴¹⁻⁴², washed with water and ethanol and checked the phase purity by XRD.

Powder X-ray diffraction. Powder X-ray diffraction for all of the samples were recorded using a Cu K α ($\lambda = 1.5406 \text{ \AA}$) radiation on a Rigaku diffractometer.

ICP-AES. Actual concentration of the lead containing solutions (1-1000 ppm) were measured by ICP-AES. ICP-AES measurements were carried out using Perkin-Elmer Optima 7000DV instrument. Cd standard (1000mg/L, Sigma-Aldrich), Mn standard (1000mg/L, Sigma-Aldrich) and multi-element standard (Ca 2000 mg/L, Na 1000 mg/L, and Mg 400 mg/L, Sigma-Aldrich) were used to determine the concentration of various cations.

ICP-MS. Element concentrations in ppb level (1-1000 ppb) were measured using a quadrupole inductively coupled plasma- mass spectrometer (ICP-MS, Thermo Scientific X- Series II) at CEaS, IISc equipped with Nickel sample and skimmer cones. Samples were introduced using a 100 ml/min PFA nebulizer connected to a peristaltic pump running at 30 rpm into an ESI-PC3 Peltier cooled spray chamber. A CETAC ASX-520 auto-sampler was used. Uptake time for samples and standards was 60 seconds while the rinse time (in 2% HNO₃) was 90 seconds.

3.1.3 Results and discussion

Dark green colour MnPS_3 (MPS-1) and light green powder KMnPS_3 (KMPS-1) were accomplished via two step reaction reported before^{13, 15}. By ICP-AES and EDAX analysis, the composition $\text{K}_{0.48}\text{Mn}_{0.76}\text{PS}_3 \cdot \text{H}_2\text{O}$ was confirmed. Powder XRD patterns recorded at room temperature for MnPS_3 , KMPS-1 and Cd-MPS-1 are shown in fig 1.

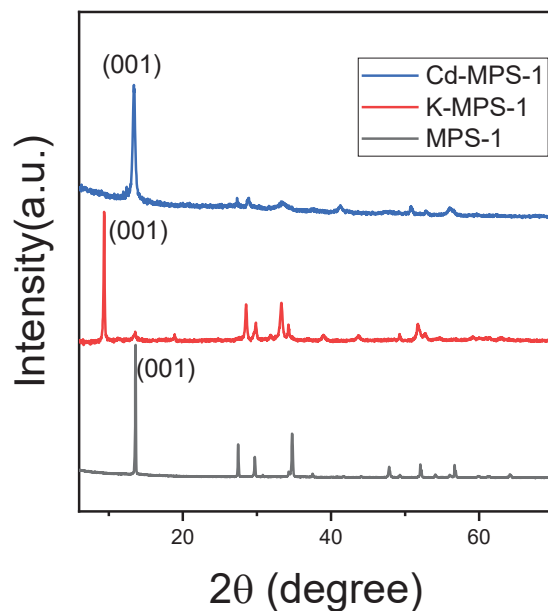
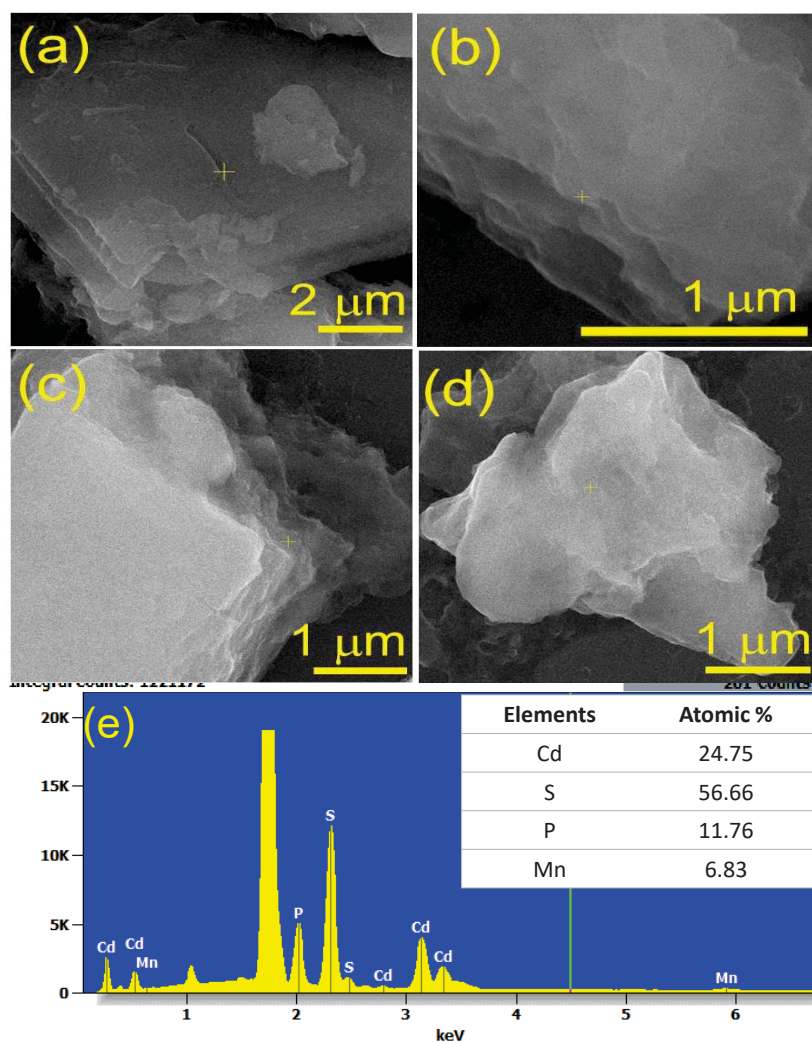


Figure 1. Powder XRD pattern of MPS-1, KMPS-1 & Cd-MPS-1

K^+ intercalation in MPS-1 increases the inter-layer spacing from 6.45 to 9.42 Å, retaining the monoclinic layered crystal structure. After Cd^{2+} sorption, the inter-layer spacing is decreased back to 6.6 Å, which is similar to pristine MPS-1 (Table-1).

Table 1. Interlayer spacing of MPS-1, K-MPS-1 and Cd-MPS-1.

Material	Interlayer spacing(\AA)
MPS-1	6.45
K-MPS-1	9.42
Cd-MPS-1	6.60

**Figure 2.** FESEM images of (a, b) KMPS-1, (c, d) Cd-MPS-1, (e) EDX spectra of Cd-MPS-1

SEM and EDAX analysis demonstrate a significant amount of Cd adsorption by KMPS-1. Layered structure of KMPS-1 is clearly visible in fig 2a, b. The Cd adsorption retains its layered structure

with an enhancement in surface roughness. EDAX spectra and color mapping show no peak for K in Cd-MPS-1, indicating complete ion exchange of K by Cd (II).

IR and Raman spectra further verifies the formation of MPS-1, K-intercalated MPS-1 and Cd-MPS. (fig. 3) In IR spectra (fig.3a), two sharp peak at 445 cm^{-1} and 565 cm^{-1} in pristine MPS-1 refers to P-P bond stretching and P-S asymmetric stretching of PS_3 unit respectively.¹⁶ During K^+ intercalation, 565 cm^{-1} peak splits into 604 and 550 cm^{-1} , which is due to maintain the charge

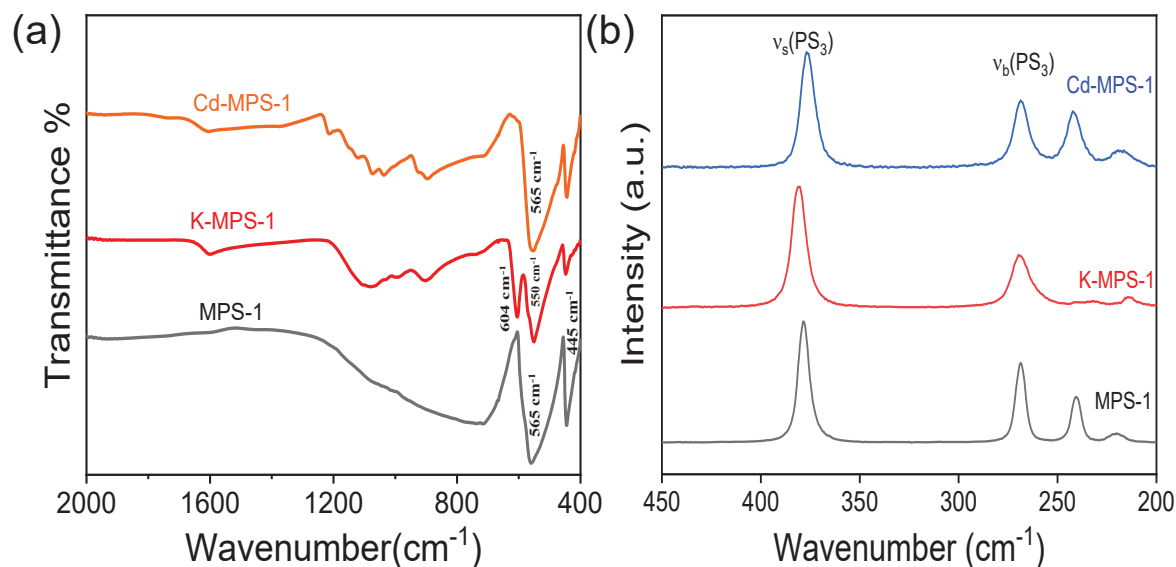


Figure 3. (a) Infrared spectra (b) Raman spectra of the MPS-1, KMPS-1 & Cd-MPS-1

balance, some Mn^{2+} comes out from the gallery creating Mn vacancy in the system and thereby distorts the inversion symmetry. of the PS_3 group. Although, when Cd capture occurs by KMPS-1, the sharp peak reappears at 565 cm^{-1} , this may be due to Cd adsorption happens not only by ion ex-change with K^+ but also by occupying the Mn vacancy site, which restore the inversion symmetry of PS_3 group.

Raman spectra (fig.3b) provides more information about the binding mode of Cd in KMPS. In pristine MPS the most intense band at 386 cm^{-1} signifies the PS_3 stretching mode ($\nu_{\text{ps}3}$), whereas

the other three bands at 275 cm⁻¹, 247 cm⁻¹ and 227 cm⁻¹ correspond to degenerate bending modes, translational mode (T_{xy}) and rotational mode (R_{xy}) of PS₃ unit respectively.¹⁷ K⁺ intercalation creates an intra-layer Mn²⁺ vacancy and decreases the P-S bond length, which leads to a red shift in the P-S stretching frequency by 2 cm⁻¹ K-MPS-1. After Cd²⁺ sorption, this P-S stretching is blue shifted to 384 cm⁻¹ due to fill up of Mn²⁺ vacancies (fig. 3b). This is attributed to the slight increase in P-S bond length in Cd-MPS- 1 with respect to P-S bond length in MPS-1.

Adsorption studies

The Cd (II) uptake experiment of KMPS-1 in solutions of different concentrations (from ppb to ppm) was performed by batch method at room temperature. (*V:m* = 1000 mL/g, pH ~ 6.5, Milli-Q water). Cd (II) concentration in aqueous solution for both before and after adsorption were measured by ICP analysis. The affinity of KMPS-1 towards Cd (II) can be expressed in terms of distribution coefficient (K_d). Value of K_d in the range of 10⁴-10⁵ mL/g are considered to be an exceptional adsorbent. KMPS-1 shows K_d for Cd (II) in the order of 10⁴ mL/g.

The distribution co-efficient (K_d) are calculated by using equation (1)

$$k_d = \left(\frac{V}{m}\right) \frac{(C_0 - c_e)}{c_e} \quad (1)$$

Where C₀ is the initial concentration and C_e is the equilibrium concentration of Cd (II). in ppm.

The observed experimental data were best fitted (R²= 0.995) using Langmuir-Freundlich model (fig. 4.) expressed as below:

$$q = q_m \frac{(bc_e)^{1/n}}{1+(bc_e)^{1/n}} \quad (2)$$

where *q* (mg/g) is the amount of the cation sorbed at equilibrium concentration C_e (ppm), *q_m* is the maximum sorption capacity of the adsorbent, C₀ is the initial concentration, *b* (L/mg) is the

Langmuir-Freundlich constant assigned to the affinity of the ions towards the adsorbents. $1/n$ is a measure of the intensity of adsorption where n is a constant.

The value of Langmuir-Freundlich constant $n = 0.07$ was found, follows the Langmuir Freundlich adsorption model with a maximum adsorption capacity (q_m) of ~ 402.35 mg/g. This result indicates that the exchangeable Cd^{2+} ions form multilayer layer assuming that sorption occurs on a structurally heterogeneous adsorbent. The high value of q_m shows strong binding affinity of KMPS-1 towards Cd (II) and this exceptionally high value outprefer the other leading materials as shown in Table 2.

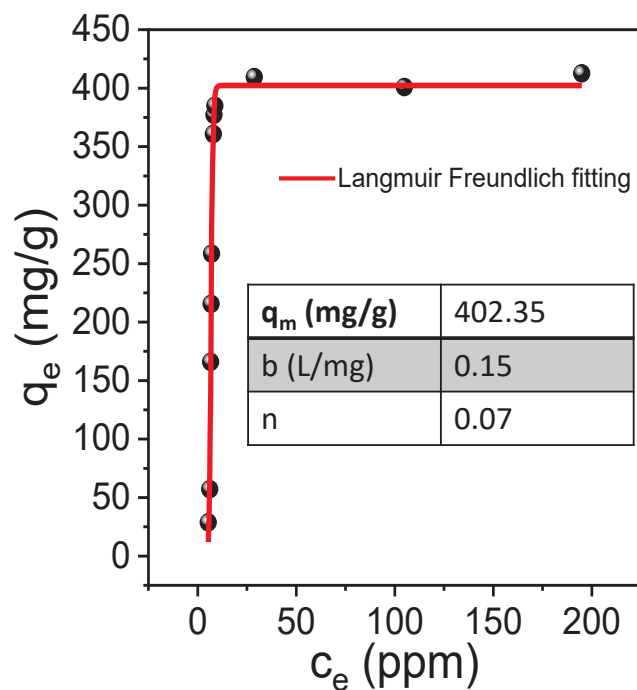


Figure 4. Sorption isotherm for the sorption of Cd^{2+} in K-MPS-1 (pH ~ 6.5 , RT, $m = 0.010$ g, $V = 10$ mL) The solid (red line) represents the fitting of the data with Langmuir- Freundlich model (fitting data for Cd^{2+} : $b = 0.15$ Lmg $^{-1}$, $n = 0.07$, $R^2 = 0.995$).

The observed Cd (II) exchange capacity (1.96 mmole/g) is almost three times higher than the theoretical exchange capacity (0.65 mmole/g) indicating Cd (II) occupies Mn^{2+} vacancy sites as well as surface of KMPS-1 to form the multilayer and this Thus, the adsorption sites for Cd^{2+} ions

are fixed in between the layers due to electrostatic interaction between the S^{2-} ions and interlayer Cd^{2+} .

Table 2. Comparison of Adsorption capacity of various adsorbents for Cd (II)^{9, 18-25}

Adsorbents	q_m (mg/g)	Reference
KMPS-1	402.3	This Work
SAMMS	97	18
Mg-MTMS	210	19
SOL-AD-IV	222	20
KMS-1	377	9
$Fe_3O_4/FeMoS_4/Mg, Al-LDH$	140.50	21
KTS-3	372	22
$LiMoS_2$	53	23
FAPTO	193.3	24
$K_x[Bi_{4-x}Mn_xS_6]$ (x = 1.28)	221.2	25

Kinetics studies

Kinetics of the ion exchange of layered K-MPS-1 is also explored. The sorption for Cd^{2+} reaches equilibrium within ~20 mins (Figure 5c.) and the rate of Cd^{2+} sorption is calculated by using two different rate equations: pseudo-first order [Eq. (3)] and pseudo-second order [Eq. (4)] as stated by the equation below:

$$\ln(q_e - q_t) = \ln q_e - k_1 t \quad (3)$$

$$\frac{t}{q_t} = \frac{1}{k_2 q_e^2} + \frac{t}{q_e} \quad (4)$$

where q_e (mg/g) is the amount of Cd^{2+} adsorbed per unit mass of adsorbent at equilibrium, q_t is Cd^{2+} ions adsorbed at time t , k_1 and k_2 (g/mg min^{-1}) are the rate constants of pseudo-first order and pseudo-second-order adsorption interactions. The value of k_1 and k_2 are estimated by plotting $\ln(q_e - q_t)$ vs. t and t/q_t vs t plot by using Eq. (3) and (4), respectively.

Table 3. Kinetics data of Cd^{2+} sorption using K-MPS-1.

Time(min)	Final Conc.(C_f)	% Removal	q (mg/g)	$K_d \times 10^4(\text{mL/g})$
20	3.30	97.35	121.49	3.68
65	2.74	97.80	122.05	4.44
190	2.49	97.99	122.30	4.89
370	2.40	98.07	122.39	5.09
480	1.61	98.70	123.18	7.61
660	1.32	98.93	123.47	9.29
1320	0.83	99.33	123.96	14.9
1560	0.49	99.60	124.30	25.06

Initial Concentration(c_0)= 124.8 ppm. $V/m = 1000 \text{ mL/g}$

Table 4. Kinetic parameters for sorption of Cd^{2+} by K-MPS-1 with two different models.

Order	Adsorbate	R^2	$q_e(\text{exp.})$	$q_e(\text{cal.})$	$K(\text{g/mg/min})$
Pseudo 1 st Order	Cd^{2+}	0.43343	124.9	88.64	1.77×10^{-3}
Pseudo 2 nd order	Cd^{2+}	0.99999	124.9	124.37	2.62×10^{-3}

The values of rate constants (k) and correlation coefficient (R^2) revealed the feasibility of kinetic path of Cd^{2+} sorption (Table.3). Hence, the goodness of fit R^2 (0.999) implies (Table.4), the sorption of Cd^{2+} on K-MPS-1 follows pseudo second- order kinetics.

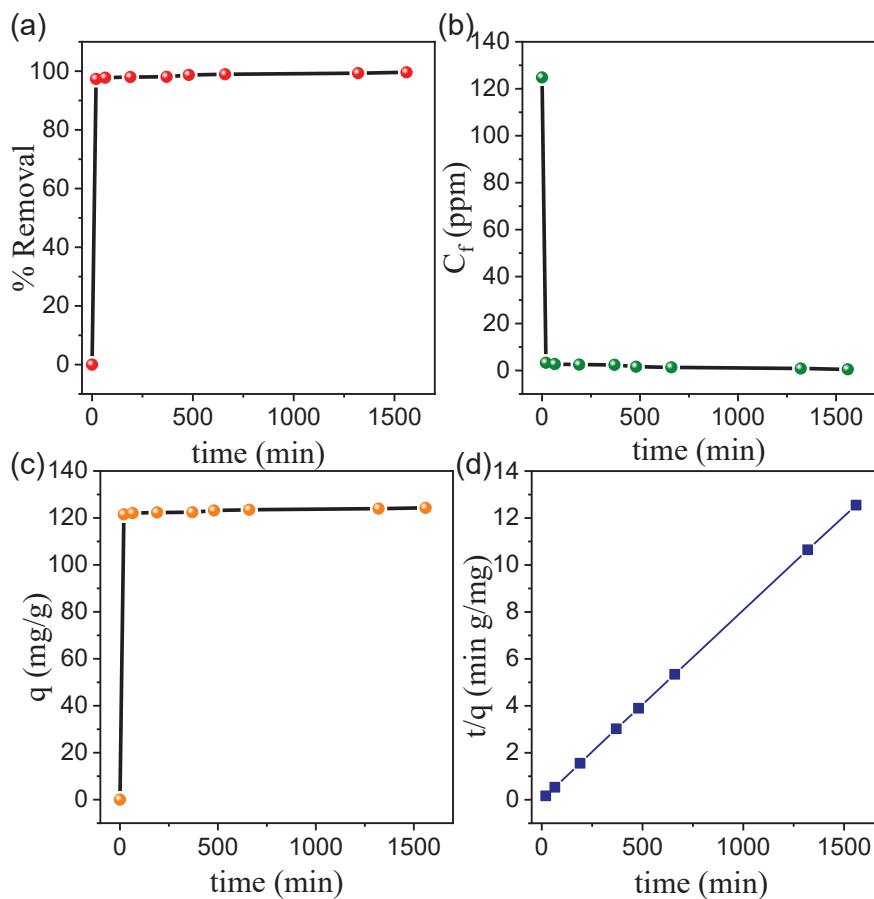


Figure 5. Sorption kinetics curve for Cd^{2+} : a) removal % of Cd^{2+} as a function of contact time b) ion concentration change with contact time c) sorption capacity (q_t) with contact time and d) pseudo-second-order kinetic plots for Cd^{2+} sorption.

Desorption studies

Irreversibility of Cd^{2+} sorption in K-MPS-1 is proved by the ICP analysis during desorption obtained by stirring Cd-MPS-1 with saturated KCl solution (Table.5). Generally, the Cd contamination is in very low concentration level (ppb) in water. At such a low concentration, K-MPS-1 can take an ample amount of Pb ~ 402.35 mg/g for long time usage.

Table 5. Desorption studies of Cd-MPS-1 by using saturated KCl.

C_0 (ppm)	C_e (ppm)	Removed %	Adsorbed on KMPS	Cd (II) released	Released %
318.1	6.951	97.8	311.15	0.651	0.2
443.4	31.52	92.9	411.88	0.561	0.1
m = 0.010 g, V = 10 mL, KCl solution					

Competitive ion-exchange and selectivity studies

The affinity and selectivity of the material are expected to be unaffected in presence of other monovalent and divalent cations. Thus, we have performed sorption studies using a solution containing a mixture of Pb^{2+} , Cd^{2+} , Na^+ , Ca^{2+} and Mg^{2+} . K-MPS-1 is capable of discriminating Cd^{2+} ions selectively (Table.6 and 7). This happens due to strong affinity of soft lewis acidic Cd (II) and soft lewis basic S^{2-} according to HSAB principle.

Table 6. Summary of the competitive ion-exchange (with Pb^{2+} in mixture solution) data of K-MPS-1

Exchange cations	Initial Conc.(ppm)	Final Conc.(ppm)	% Removal	q(mg/g)	K_d (mL/g) $\times 10^4$
Cd^{2+}	19.42	0.46	97.40	18.96	4.09
Pb^{2+}	16.82	6.20	63.13	10.61	0.17
Mg^{2+}	2.02	1.57	22.40	0.45	0.03
Ca^{2+}	8.17	5.71	30.00	2.46	0.04
Na^+	10.79	9.92	8.01	0.86	0.03

Table 7. Summary of the competitive ion-exchange (without Pb^{2+} in mixture solution) data of K-MPS-1

Exchange cations	Initial Conc.(ppm)	Final Conc.(ppm)	% Removal	q(mg/g)	$K_d(\text{mL/g}) \times 10^4$
Cd^{2+}	17.14	0.78	95.00	16.36	2.09
Mg^{2+}	2.02	1.74	13.00	0.28	0.02
Ca^{2+}	7.92	5.76	27.30	2.17	0.04
Na^+	10.80	10.13	6.20	0.67	0.01

The affinity and selectivity order of cations, determined by comparison of K_d value are to be in the order: $\text{Cd}^{2+} \gg \text{Pb}^{2+} > \text{Ca}^{2+} \approx \text{Mg}^{2+} \approx \text{Na}^+$.

Adsorption studies in different pH

The interaction between the K-MPS-1 and Cd^{2+} is persistent in a broad pH range 2-11 and interaction strength is unaltered with a K_d of the order of $\sim 10^3$ to 10^4 mL/g in the 2-11 pH range (fig.6b). PXRD analysis shows that the K-MPS-1 is stable within a pH range 2-11 (fig 6c.) which indeed indicates the structure and composition is stable in such broad pH range. A maximum K_d^{Cd} value of $8.20 \times 10^4 \text{ mL g}^{-1}$ with the highest Cd^{2+} removal capacity of 98.79% is observed at pH 8.5. Hence, KMPS-1 proves to retain the Cd removal capacity in a broad pH range.

Mechanism of Cd (II) adsorption in KMPS-1

Structural changes in K-MPS-1 sample after the Cd (II) adsorption have been suggested by the XRD data, FTIR-Raman data and by the FESEM studies. Based on the above observations, the complexation chemistry of Cd (II) by K-MPS-1, are summarized qualitatively as follows:

Initially, intercalation of K^+ in MPS-1, results in increase in the interlamellar spacing as

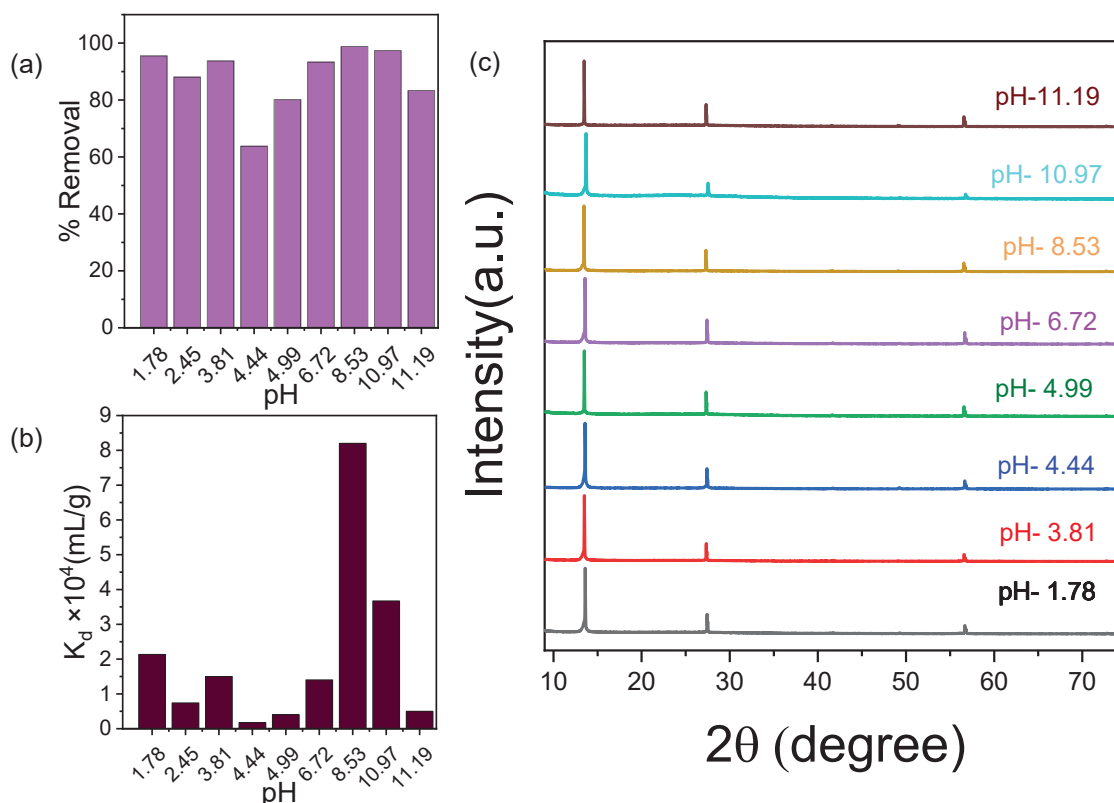


Figure 6. (a) Removal % and (b) Distribution coefficient value of Cd^{2+} at different pH (c) PXRD patterns of Cd sorbed KMPS-1 at different pH.

shown in XRD plot, which generates Mn^{2+} vacancy for maintaining the overall charge balance, resulting self-oxidation of Mn^{2+} to Mn^{3+} in K-MPS-1, which can be verified by XPS data as shown in fig.7 (a, b). During Cd adsorption process, Cd (II) goes into the Mn^{2+} vacancy site (IR and Raman data) and kick out the intercalated K^+ from the interlayer spacing, resulting decrease in d_{basal} . The high adsorption capacity value of ~ 402.35 mg/g also indicates that the Cd (II)

adsorption takes place not only in the Mn²⁺ vacancy sites, but also in the interlayer spacing and

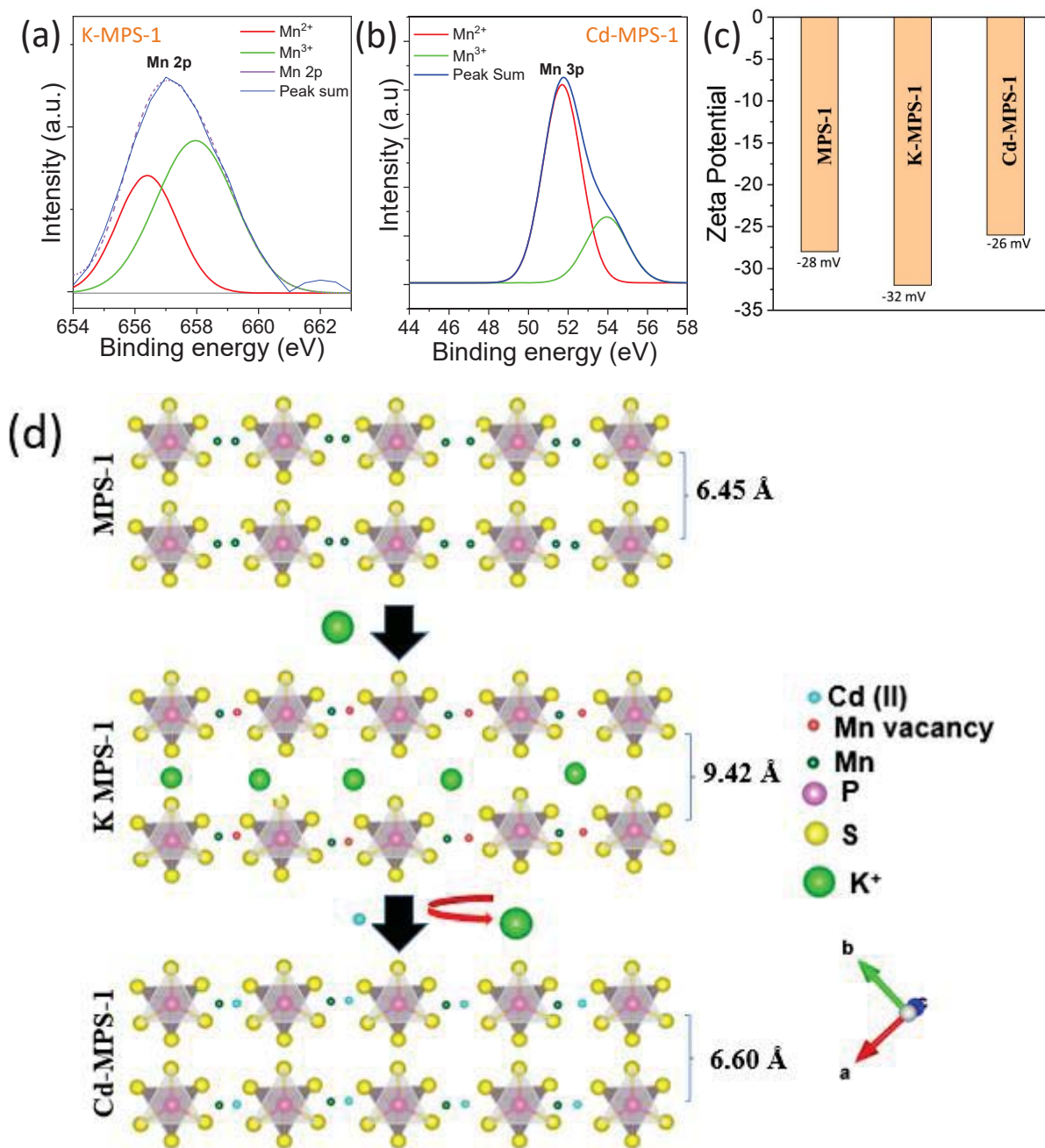


Figure 7. (a) Mn 2p peak in the XPS spectrum of K-MPS-1, (b) Mn 3p peak of Cd-MPS-1 in XPS spectrum, (c) Zeta potential of MPS-1, K-MPS-1 and Cd-MPS at room temperature. (d) Schematic representation of Cd(II) ion exchange by K-MPS-1.

on the surface of the K-MPS-1 also, which can be further verified by the zeta potential study as shown in fig. 7c. where during K^+ intercalation, it results in producing excess negative charge on surface S atoms but that diminishes after Cd adsorption in Cd-MPS-1. In summary, qualitative Cd (II) adsorption mechanism of K-MPS-1 can be visualized by schematic representation as shown in fig.7d.

Low concentration (ppb level) Cd capture

Cd^{2+} sorption studies were carried out in low ppb range from 1 ppb to 1102 ppb. We have observed ~100% removal of cadmium from water in this range. Table.8 shows that K-MPS-1 effectively

Table 8. Removal of Cd^{2+} at lower ppb level

Initial Conc.(ppb)	Final Conc.(ppb)	% Removal
1	0	100.00
2	0	100.00
7	0	100
51	1	98.03
77	1	98.70
143	1	99.30
424	4	99.05
528	3	99.43
788	0	100
1102	14	98.72

removes Cd from trace level. While, according to USA-EPA, the maximum limit of Cd (II) in drinking water is 5 ppb, our material K-MPS-1 can adsorb Cd (II) from very trace 1 ppb level efficiently.

3.1.4. Conclusion

In summary, Cd²⁺ sorption and ion-exchange kinetics of K-MPS-1 were studied in detail. K-MPS-1 removes Cd²⁺ with a remarkably high capacity (402.35 mg/g) following Langmuir-Freundlich model. It has high distribution co-efficient of $\sim 10^4$ mL g⁻¹ for Cd²⁺ which follows pseudo-second order kinetics, indicates the sorption is chemisorption. K-MPS-1 demonstrates efficient Cd removal (~ 100 %) from the dilute concentration of aqueous Cd²⁺ solutions (1-1100 ppb). K-MPS-1 exhibits high selectivity towards Cd²⁺ in presence of other hindering hard cations such as Na⁺, Ca²⁺, Mg²⁺ due to strong soft acid-soft base Cd-S interactions, according to the HSAB principle. K-MPS-1 can operate even in broad pH range of 1.8-11, Further, the present study can be extended to remove toxic heavy metals (Hg and As) from wastewater by using K-MPS-1.

3.1.5. References.

1. Romanovskiy, V. N.; Smirnov, I. V.; Babain, V. A.; Todd, T. A.; Herbst, R. S.; Law, J. D.; Brewer, K. N., The universal solvent extraction (UNEX) process. I. Development of the UNEX process solvent for the separation of cesium, strontium, and the actinides from acidic radioactive waste. *Solvent Extr. Ion Exch.* **2001**, *19* (1), 1-21.
2. Liu, X.; Chen, G.-R.; Lee, D.-J.; Kawamoto, T.; Tanaka, H.; Chen, M.-L.; Luo, Y.-K., Adsorption removal of cesium from drinking waters: A mini review on use of biosorbents and other adsorbents. *Bioresour. Technol.* **2014**, *160*, 142-149.
3. Shannon, M. A.; Bohn, P. W.; Elimelech, M.; Georgiadis, J. G.; Marinas, B. J.; Mayes, A. M., Science and technology for water purification in the coming decades. *Nanoscience and technology: a collection of reviews from nature Journals* **2010**, 337-346.
4. Tonini, D. R.; Gauvin, D. A.; Soffel, R. W.; Freeman, W. P., Achieving low mercury concentrations in chlor-alkali wastewaters. *Environ. Prog.* **2003**, *22* (3), 167-173.
5. Benhammou, A.; Yaacoubi, A.; Nibou, L.; Tanouti, B., Adsorption of metal ions onto Moroccan stevensite: kinetic and isotherm studies. *J. Colloid Interface Sci.* **2005**, *282* (2), 320-326.
6. El Mouzdahir, Y.; Elmchaouri, A.; Mahboub, R.; ElAnssari, A.; Gil, A.; Korili, S.; Vicente, M., Interaction of stevensite with Cd^{2+} and Pb^{2+} in aqueous dispersions. *Appl. Clay Sci.* **2007**, *35* (1-2), 47-58.
7. Zhao, X.; Jia, Q.; Song, N.; Zhou, W.; Li, Y., Adsorption of Pb (II) from an aqueous solution by titanium dioxide/carbon nanotube nanocomposites: kinetics, thermodynamics, and isotherms. *Journal of Chemical & Engineering Data* **2010**, *55* (10), 4428-4433.
8. Manos, M. J.; Ding, N.; Kanatzidis, M. G., Layered metal sulfides: exceptionally selective agents for radioactive strontium removal. *Proc. Natl. Acad. Sci* **2008**, *105* (10), 3696-3699.
9. Manos, M. J.; Kanatzidis, M. G., Sequestration of heavy metals from water with layered metal sulfides. *Chem. Eur. J.* **2009**, *15* (19), 4779-4784.
10. Manos, M. J.; Kanatzidis, M. G., Layered metal sulfides capture uranium from seawater. *J. Am. Chem. Soc.* **2012**, *134* (39), 16441-16446.
11. Manos, M. J.; Kanatzidis, M. G., Highly efficient and rapid Cs^+ uptake by the layered metal sulfide $\text{K}_{2x}\text{Mn}_x\text{Sn}_{3-x}\text{S}_6$ (KMS-1). *J. Am. Chem. Soc.* **2009**, *131* (18), 6599-6607.

12. Sarma, D.; Malliakas, C. D.; Subrahmanyam, K.; Islam, S. M.; Kanatzidis, M. G., $K_{2x}Sn_{4-x}S_{8-x}$ ($x=0.65-1$): a new metal sulfide for rapid and selective removal of Cs^+ , Sr^{2+} and UO_2^{2+} ions. *Chem. sci.* **2016**, 7 (2), 1121-1132.
13. Rathore, E.; Pal, P.; Biswas, K., Layered metal chalcophosphate (K-MPS-1) for efficient, selective, and ppb level sequestration of Pb from water. *J. Phys. Chem. C.* **2017**, 121 (14), 7959-7966.
14. Rathore, E.; Pal, P.; Biswas, K., Reversible and Efficient Sequestration of Cesium from Water by the Layered Metal Thiophosphate $K_{0.48}Mn_{0.76}PS_3 \cdot H_2O$. *Chem. Eur. J.* **2017**, 23 (46), 11085-11092.
15. Clement, R., A novel route to intercalation into layered MnPS₃. *Chem. Commun.* **1980**, (14), 647-648.
16. Mathey, Y.; Clement, R.; Sourisseau, C.; Lucazeau, G., Vibrational study of layered MPX₃ compounds and of some intercalates with $Co(\eta^5-C_5H_5)^{2+}$ or $Cr(\eta^6-C_6H_6)^{2+}$. *Inorg. Chem.* **1980**, 19 (9), 2773-2779.
17. Joy, P. A.; Vasudevan, S., The intercalation reaction of pyridine with manganese thiophosphate, MnPS₃. *J. Am. Chem. Soc.* **1992**, 114 (20), 7792-7801.
18. Yantasee, W.; Lin, Y.; Fryxell, G. E.; Busche, B. J.; Birnbaum, J. C., Removal of heavy metals from aqueous solution using novel nanoengineered sorbents: self-assembled carbamoylphosphonic acids on mesoporous silica. *Sep. Sci. Technol.* **2003**, 38 (15), 3809-3825.
19. Gomez-Salazar, S.; Lee, J.; Heydweiller, J.; Tavlarides, L., Analysis of cadmium adsorption on novel organo-ceramic adsorbents with a thiol functionality. *Industrial & engineering chemistry research* **2003**, 42 (14), 3403-3412.
20. Lagadic, I. L.; Mitchell, M. K.; Payne, B. D., Highly effective adsorption of heavy metal ions by a thiol-functionalized magnesium phyllosilicate clay. *Environ. Sci. Technol.* **2001**, 35 (5), 984-990.
21. Behbahani, E. S.; Dashtian, K.; Ghaedi, M., Fe_3O_4 - $FeMoS_4$: Promise magnetite LDH-based adsorbent for simultaneous removal of Pb (II), Cd (II), and Cu (II) heavy metal ions. *J. Hazard. Mater.* **2021**, 410, 124560.
22. Sarma, D.; Islam, S. M.; Subrahmanyam, K.; Kanatzidis, M. G., Efficient and selective heavy metal sequestration from water by using layered sulfide $K_{2x}Sn_{4-x}S_{8-x}$ ($x=0.65-1$; KTS-3). *J. Mater. Chem. A* **2016**, 4 (42), 16597-16605.

23. Gusain, R.; Kumar, N.; Fosso-Kankeu, E.; Ray, S. S., Efficient removal of Pb (II) and Cd (II) from industrial mine water by a hierarchical MoS₂/SH-MWCNT nanocomposite. *ACS omega* **2019**, *4* (9), 13922-13935.
24. Wang, P.; Sun, D.; Deng, M.; Zhang, S.; Bi, Q.; Zhao, W.; Huang, F., Amorphous phosphated titanium oxide with amino and hydroxyl bifunctional groups for highly efficient heavy metal removal. *Environ. Sci. Nano* **2020**, *7* (4), 1266-1274.
25. Wang, R.; Chen, H.; Xiao, Y.; Hadar, I.; Bu, K.; Zhang, X.; Pan, J.; Gu, Y.; Guo, Z.; Huang, F., K_x[Bi_{4-x}Mn_xS₆], Design of a Highly Selective Ion Exchange Material and Direct Gap 2D Semiconductor. *J. Am. Chem. Soc.* **2019**, *141* (42), 16903-16914.

Chapter 3.2

Hierarchical Layered Double Hydroxide as a Swift and Efficient Scavenger for Toxic Anions, AsO_4^{3-} and SeO_3^{2-} from Water

Chapter 3.2

Hierarchical Layered Double Hydroxide as a Swift and Efficient Scavenger for Toxic Anions, AsO_4^{3-} and SeO_3^{2-} from Water

Summary

Rapid industrialization has led to the release of arsenate and selenite, a “Class A” human carcinogen, mutagen, and teratogen in biological systems. Current adsorbents like anionic exchange resins and metal–organic frameworks can remove harmful heavy metal oxyanions from water but are not stable in a broad pH range, suffer from selectivity, and cannot capture them from trace values below the tolerance limits. Herein, we have shown that the nature-inspired coral like layered Co, Al-LDH selectively and efficiently sequesters toxic oxoanions As(V) and Se (IV) in a very wide pH range from ~1.9 to 12.5 and with a high capacity of 129.22 mg g⁻¹ for As (V) and 130.56 mg g⁻¹ for Se (IV). The high adsorption capacity for As (V) and Se (IV) are superior to other reported adsorbents, indicating the great potential of this material for trapping these oxoanions. The adsorption equilibrium is reached within ten minutes for both of them, indicating very rapid removal of As (V) and Se (IV) from wastewater by Co, Al-LDH. The reason for rapid removal can be attributed to the weak bonding interaction between SeO_3^{2-} and AsO_4^{3-} towards brucite-like layers which promotes the efficient anion exchange.

3.2.1. Introduction

Water contamination is a significant, worldwide problem that poses serious health and environmental hazards. Arsenic is one of the most toxic chemical elements that causes serious health risks to humans. Many areas of the world including locals in India, Bangladesh, China, Spain, Canada, and elsewhere were reported to be exposed to severe arsenic contamination via the drinking water system.¹⁻³ Arsenic is introduced into aquatic environment from both natural and man-made sources. Typically, arsenic occurrence in groundwater is caused by the weathering and dissolution of arsenic-bearing rocks, minerals and ores. The problem is especially acute in India, where as many as 60 million people are at risk of chronic arsenic poisoning. As a “Class A” human carcinogen, arsenic can cause various diseases, such as cancers (skin, liver, lung, bladder), cardiovascular, neurological diseases and immune problems.⁴ To protect human health from the adverse effects of arsenic, the WHO⁵ and US-EPA⁶ set the arsenic level in drinking water as < 10 ppb. Selenium is another borderline essential nutrient element for humans and animals in trace amounts while it is extremely toxic at higher concentrations.⁷ It has the narrowest range between dietary deficiency (400 µg/day) and toxic levels (>400 µg/day). Problems of both Se toxicity and deficiency occur in different parts all over the world.⁸ In particular, the redox-sensitive radionuclide of ⁷⁹Se has a very long half-life and is chemically and radiologically toxic. Acute exposure to selenium compounds may lead to severe respiratory problems and neurological effects.⁹ In drinking water, 40 and 50 ppb have been set as the maximum acceptable concentration by the World Health Organization (WHO) and United States Environmental Protection Agency (USEPA) and in Europe and Japan the limit is 10 ppb.¹⁰ Therefore, the efficient and economical eradication of arsenic and selenium from industrial wastewater and sewage before discharging it into the water streams has become an emergent issue.

Various treatment technologies have been used for purification of water contaminated by toxic oxoanions and metal cations, including chemical precipitation, adsorption, ion-exchange, filtration and so on but they are not up to the mark for removing them in trace ppb level.¹¹ One of the most cost-effective methods widely implemented for water purification is using natural adsorbents like clay, zeolites, mesoporous silica, activated charcoal, polymers, biomaterials, Metal Organic Frameworks etc but they also lack strong binding affinity, high selectivity, pH, and temperature stability and some of them exhibit cytotoxicity, thus limiting their application.¹²

Layered double hydroxides (LDHs) and layered rare earth hydroxides (LRHs) are two kinds of important two-dimensional materials consisting of positively charged host layers and counter-anions in the interlayer space.¹³ Their excellent intercalation and anion-exchange capability allow them to play versatile roles on applications such as two-dimensional nanoreactors, sorbents and scavengers.¹⁴ The anion exchange capability (layer -OH groups and interlayer anions) of the LDH materials enable them to be used for the capture of toxic oxoanions. Very recently, our group has shown efficient uptake of dichromate anion using coral like Co, Al-LDH with a high distribution coefficient of $1.09 \times 10^6 \text{ mL g}^{-1}$ working in a wide pH range.¹⁵

Herein, we have investigated the capture ability of Co, Al-LDH for the toxic oxoanions of AsO_4^{3-} (As(V)), and SeO_3^{2-} (Se (IV)) from water. We find that LDH exhibits preferential binding and enormous selectivity for these oxoanions. The AsO_4^{3-} adsorption follows Langmuir-Freundlich adsorption isotherm exhibiting a high adsorption capacity of 129.22 mg/g and SeO_3^{2-} follows Langmuir isotherm with a q_m of 130.56 mg/g, which are relatively much higher compared to other reported adsorbents.

3.2.2. Experimental section

Synthesis. Coral-like Co, Al-LDH hollow spheres were synthesized by the hydrothermal technique.¹⁶ Typically, 9 mmol of $\text{Co}(\text{NO}_3)_2 \cdot 6\text{H}_2\text{O}$ (Sigma-Aldrich, 99.999% trace metals basis), 3 mmol of $\text{Al}(\text{NO}_3)_3 \cdot 9\text{H}_2\text{O}$ (Sigma Aldrich, 99.997% trace metals basis), 21 mmol of urea (Sigma Aldrich, ACS reagent, 99.0–100.5%), and 100 mg of NH_4F (Sigma Aldrich, $\geq 99.99\%$ trace metals basis) were dissolved in 30 mL of methanol, and the contents were stirred for 2 h. Then, the solution was moved into a 50 mL Teflon-lined autoclave and was kept at 150 °C for 10 h. Finally, the product was accumulated by washing with deionized water and ethanol.

Powder X-ray diffraction. Powder X-ray diffraction for all of the samples were recorded using a $\text{Cu K}\alpha$ ($\lambda = 1.5406 \text{ \AA}$) radiation on a Rigaku diffractometer.

Fourier transform infrared spectroscopy. FTIR spectra of powder sample was recorded using a Bruker IFS 66v/S spectrometer

Field emission scanning electron microscopy and energy dispersive spectroscopy analysis. FESEM of the synthesized and lead adsorbed materials were performed using NOVA NANO SEM 600 (FEI, Germany) operated at 15 KV. EDAX compositional analysis was performed during FESEM imaging.

ICP-AES. Actual concentration of the As and Se containing solutions (1-1000 ppm) were measured by ICP-AES. ICP-AES measurements were carried out using Perkin-Elmer Optima 7000DV instrument. As standard (1000mg/L, Sigma-Aldrich), Se standard (1000mg/L, Sigma-Aldrich) and multi-element standard (Cl^- 2000 mg/L, Br^- 1000 mg/L, and NO_3^- 400 mg/L, Sigma-Aldrich) were used to determine the concentration of various anions.

3.2.3. Results and discussion

3.2.3.1. Characterization

The powder X-ray diffraction (PXRD) pattern of Co, Al-LDH sample in Figure. 1a shows the classic nature of hydrotalcite materials, where diffraction peaks at 2θ of 9.95, 20.02, 34.08, and 37.52° are ascribed to (003), (006), (012), and (015) diffraction planes respectively, matching with the hexagonal phase of $(\text{Co}_4\text{Al}_2(\text{OH})_{12}\text{CO}_3(\text{H}_2\text{O})_3)_{0.5}$ (JCPDS card no. 97-017-2995).

IR spectra further verifies the formation of LDH in Figure. 1b. The prominent peak at 1365 cm^{-1} confirms the presence of intercalated CO_3^{2-} in it.¹⁶ Along with this, the broad band in the range of $3300\text{--}3600\text{ cm}^{-1}$ is attributed to O-H stretching vibrations of surface hydroxyl groups.

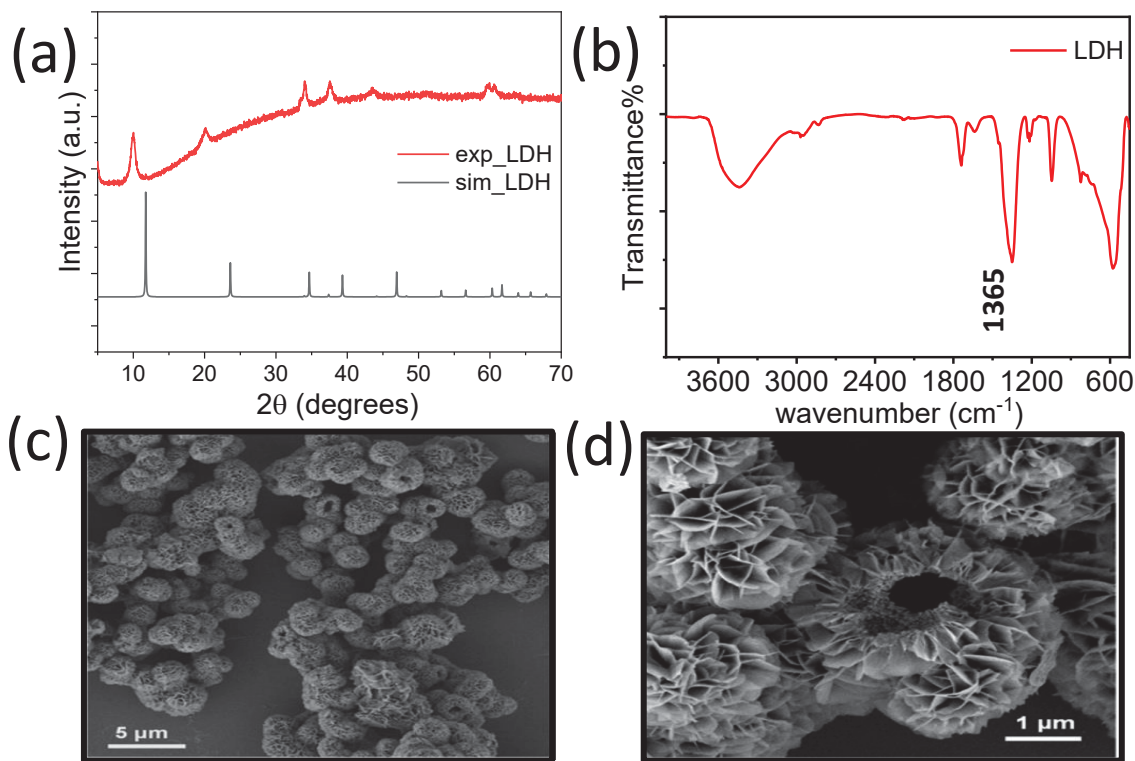


Figure 1. (a) PXRD patterns, (b) Infrared Spectra, (c) and (d) FESEM images of Co, Al-LDH.

The field emission scanning electron microscopy (FESEM) images of Co, AL-LDH show well-defined distinct microspheres of $\sim 1\text{--}3\text{ }\mu\text{m}$ in diameter (Figure 1c, d), different from traditional hexagonal platelet crystallites of LDHs, which upon drying, form irregular stone-like

aggregates that hinder the adsorption performances. Here, the addition of a small amount of ammonium fluoride (NH₄F) in the synthesis acts as a structure mediating agent, which is responsible for the formation of these 3D crystalline hollow coral-like structures. The higher magnification FESEM image (Figure 1c) depicts that the microspheres have a nature-inspired coral-like hierarchical morphology comprising self-organized hexagonal nanoplates extending from the center of microspheres and distributing consistently in all directions leading to hollow structures.

3.2.3.2. Quantitative analysis

Adsorption isotherm studies

In order to determine the maximum uptake capacity of the LDH material towards the oxoanions of As (V) and Se (IV), adsorption equilibrium experiments are performed using batch method. It is clear from the observed results (Table 1 and 2) that the amount of As (V) as well as Se (IV) adsorbed by Co, Al-LDH increases with increasing initial concentration. For As(V), the maximum adsorption capacity is found to be 105 mg/g, which is much higher than the theoretical capacity of 78.0 mg/g calculated from the molecular formula considering complete ion exchange. It simply implies that, apart from the ion exchange between CO₃²⁻ and As (V) oxoanion, surface adsorption on positively charged LDH layers also takes place. Similarly, we obtain a maximum adsorption capacity of 123 mg/g for Se (IV), which is also greater than the theoretical value (82.2 mg/g).

The adsorption data for As (V) gets best fitted with the Langmuir-Freundlich isotherm model expressed as below.

$$q = q_m \frac{(bc_e)^{1/n}}{1+(bc_e)^{1/n}}$$

Table 1: Sorption results of Co, Al-LDH toward As (V). ($V/m = 500 \text{ mL/g}$)

C_o (ppm)	C_e (ppm)	% Removal	q (mg/g)	K_d (mg/g)
100.2	1.331	98.67	49.43	3.71×10^4
159	16.71	89.49	71.14	4.25×10^3
261.9	97.62	62.72	82.14	0.84×10^3
340.4	165.1	51.49	87.65	0.53×10^3
493.8	299.2	39.40	97.30	0.32×10^3
625.1	420.8	32.68	102.15	0.24×10^3
761.7	551.6	27.58	105.05	0.19×10^3

where q (mg/g) is the amount of the cation sorbed at equilibrium concentration C_e (ppm), q_m is the maximum sorption capacity of the adsorbent, C_o is the initial concentration, b (L/mg) is the

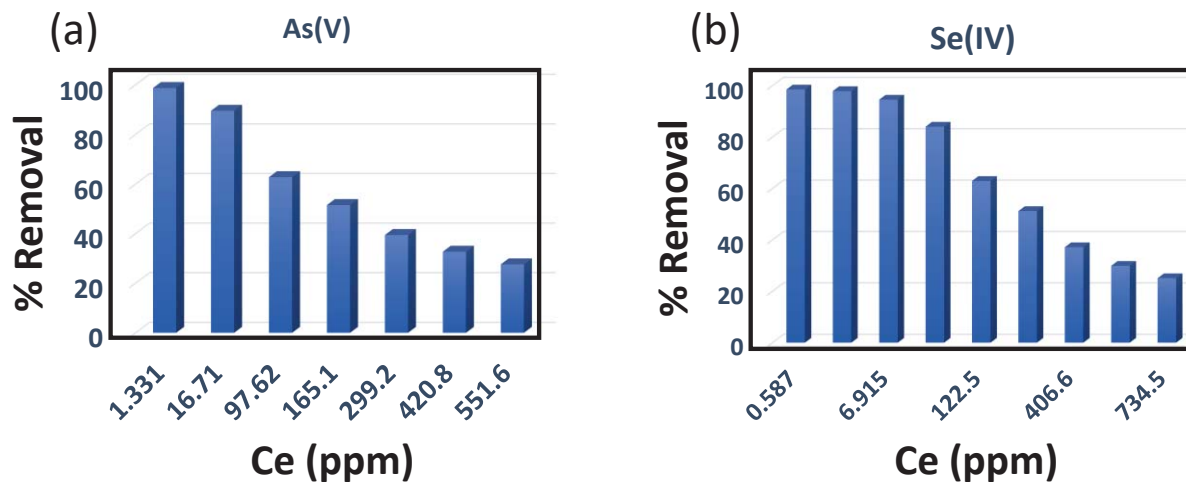


Figure 2. (a) Removal percentage as a function of equilibrium concentration for (a) As (V) and (b) for Se (IV)

Langmuir-Freundlich constant assigned to the affinity of the ions towards the adsorbents. $1/n$ is a measure of the intensity of adsorption where n is a constant.

Table 2: Sorption results of Co, Al-LDH toward Se (IV).

C_i (ppm)	C_f (ppm)	% Removal	q (mg/g)	K_d (mL/g)
39.51	0.587	98.51	19.46	3.315×10^4
66.11	1.383	97.90	32.36	23.40×10^4
127.3	6.915	94.56	60.19	8.70×10^3
196.1	31.27	84.05	82.41	2.63×10^3
330.4	122.5	62.97	103.95	0.84×10^3
462.8	225.8	51.21	118.5	0.52×10^3
646.8	406.6	37.13	120.1	0.29×10^3
815	571.4	29.88	121.8	0.21×10^3
980.4	734.5	25.08	122.95	0.16×10^3

The q_m value obtained for As (V) from fitting curve (Figure. 3a.) is 129.22 mg/g, which is approximately 1.2 times of the experimental value of 105.05 mg/g.

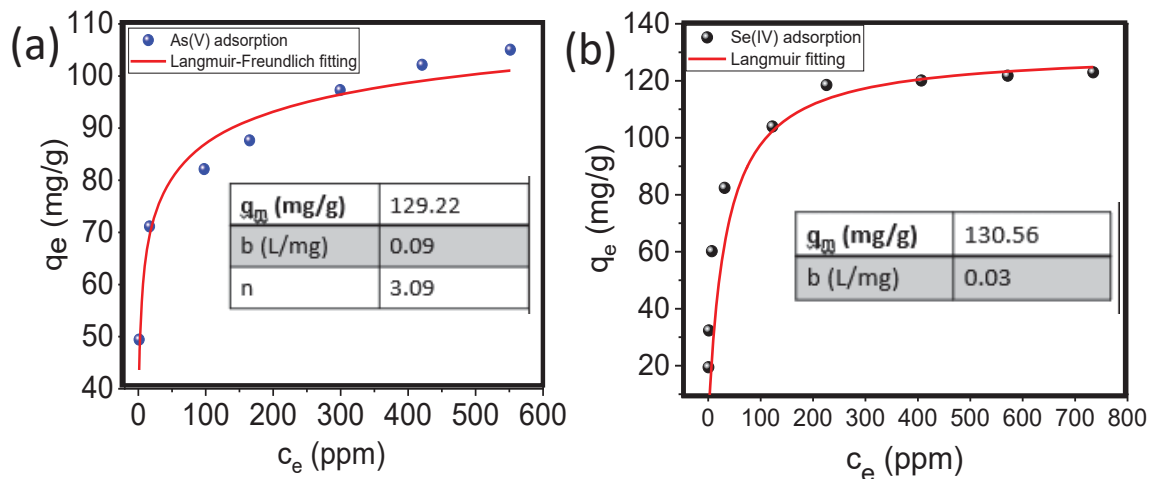
**Figure 3.** Adsorption isotherm for the sorption of (a) As (V) and (b) Se (IV)

Figure. 3b. shows experimental Se (IV) adsorption isotherm data, best fitted with the Langmuir isotherm model for heterogeneous surfaces.

$$q = q_m \frac{bc_e}{1+bc_e}$$

which signifies the monolayer type of coverage of the sorbent on an adsorbent surface. Once an adsorption site is occupied, no further adsorption can happen at the same site. The q_m value obtained from Langmuir fitting curve (Figure. 3b) is 130.56 mg/g, which is approximately similar to the experimental value of 123 mg/g.

In both cases, we have achieved the K_d values of around 10^4 order (Table 1 and 2) which is quite good, indicating the promising capability of Co, Al-LDH for the capture of toxic oxoanions of As (V) and Se (IV).

Kinetics studies.

To understand the dynamics of As (V) and Se (IV) sorption, kinetics studies were carried out where, samples are analyzed at different contact time intervals. The results (Table 3 and 4) certify the rapid removal of oxoanions. Within an hour, > 95% removal of As (V) oxoanion takes place. In case of Se (IV), more exciting results are obtained as > 95% removal occurs in just one minute. These interesting outputs place the Co, Al-LDH among one of the topmost adsorbents for capture of As (V) and Se (IV) from water.

Table 3. Kinetics data of Co, Al-LDH toward As (V).

Time (min)	C _i (ppm)	C _f (ppm)	% Removal	q (mg/g)
0	104.9	104.9	0	0
1	104.9	15.73	85.00	44.58
5	104.9	11.83	88.7	46.53
10	104.9	9.47	90.97	47.71
20	104.9	7.804	92.56	48.54
40	104.9	5.75	94.51	49.57
60	104.9	4.899	95.32	50.00
120	104.9	3.677	96.4	50.61
180	104.9	2.947	97.19	50.97
240	104.9	2.66	97.46	51.12
720	104.9	1.508	98.56	51.69
1440	104.9	1.228	98.82	51.83

The pseudo first order and pseudo second order mechanism are employed to determine the sorption nature. The rate equation of these two are as follows:

Pseudo first order kinetic model. $\ln(q_e - q_t) = \ln q_e - k_1 t$

Pseudo second order kinetic model. $\frac{t}{q_t} = \frac{1}{k_2 q_e^2} + \frac{t}{q_e}$

where q_e (mg/g) is the amount of adsorbed element per unit mass of sorbent at equilibrium and q_t (mg/g) is the adsorbed amount at time t , while k_1 (min⁻¹) and k_2 (g/mg min⁻¹) are equilibrium rate constants of pseudo-first order and pseudo-second order sorption

interactions, respectively. The k_1 value was obtained by plotting $\ln(q_e - q_t)$ against t and k_2 by plotting t/q_t against t .

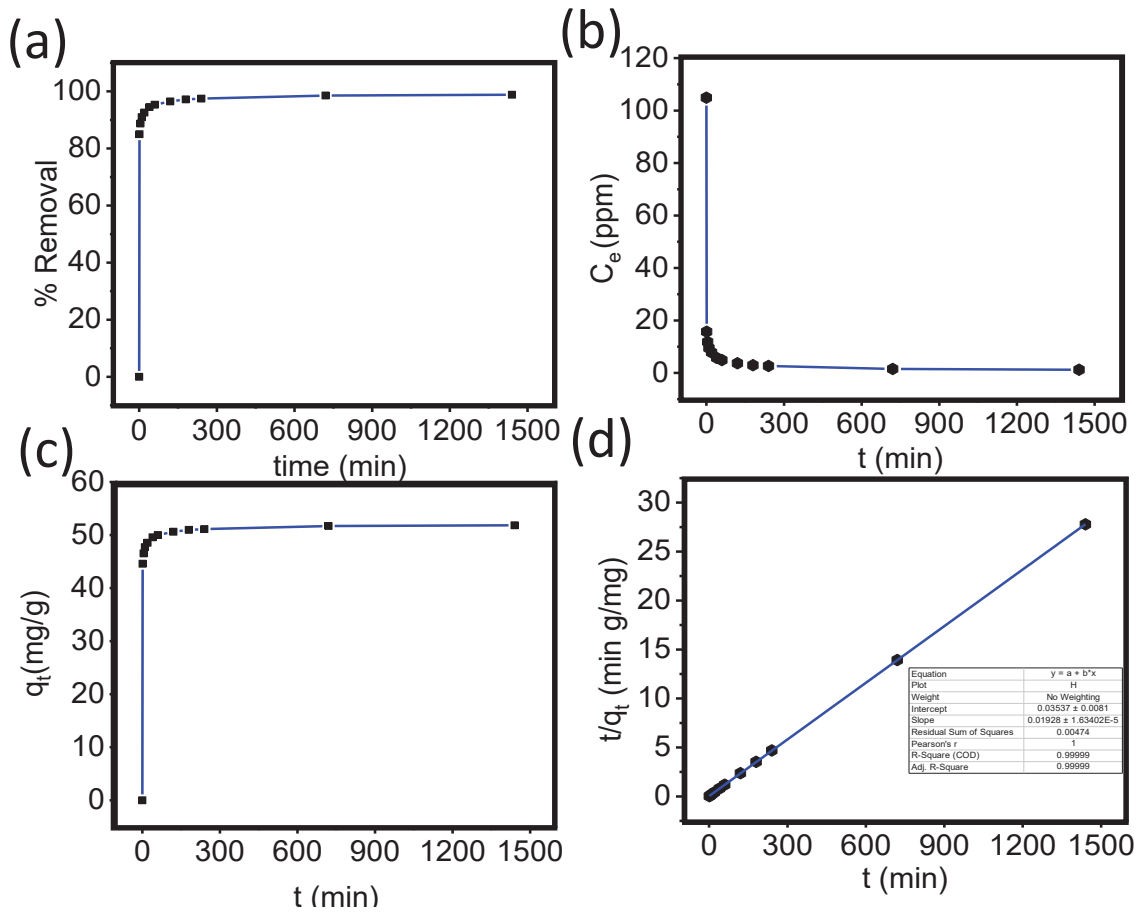


Figure 4. Sorption kinetics curve for As (V): (a) removal % of As(V) as a function of contact time (b) ion concentration change with contact time (c) sorption capacity (q_t) with contact time and (d) pseudo-second-order kinetic plots for As(V) sorption.

Table 4: Kinetics data of Co, Al-LDH toward Se (IV).

Time (min)	C _i (ppm)	C _f (ppm)	% Removal	q (mg/g)
0	61.59	61.59	0	0
1	61.59	3.04	95.06	29.27
5	61.59	2.90	95.17	29.30
10	61.59	2.53	95.87	29.52
20	61.59	2.32	96.22	29.63
40	61.59	2.12	96.55	29.73
60	61.59	2.09	96.59	29.74
120	61.59	1.90	96.90	29.84
180	61.59	1.85	96.98	29.86
240	61.59	1.78	97.10	29.90
480	61.59	1.55	97.48	30.01
720	61.59	1.5	97.56	30.04
1440	61.59	1.5	97.56	30.04

The sorption kinetics curve for both As (V) and Se (IV) get best fitted with the pseudo second order model (Table 5 and 6) as the goodness of fit coefficients (R^2) are closer to 1 for it. It simply suggests that the chemisorption phenomenon takes place for both of them.

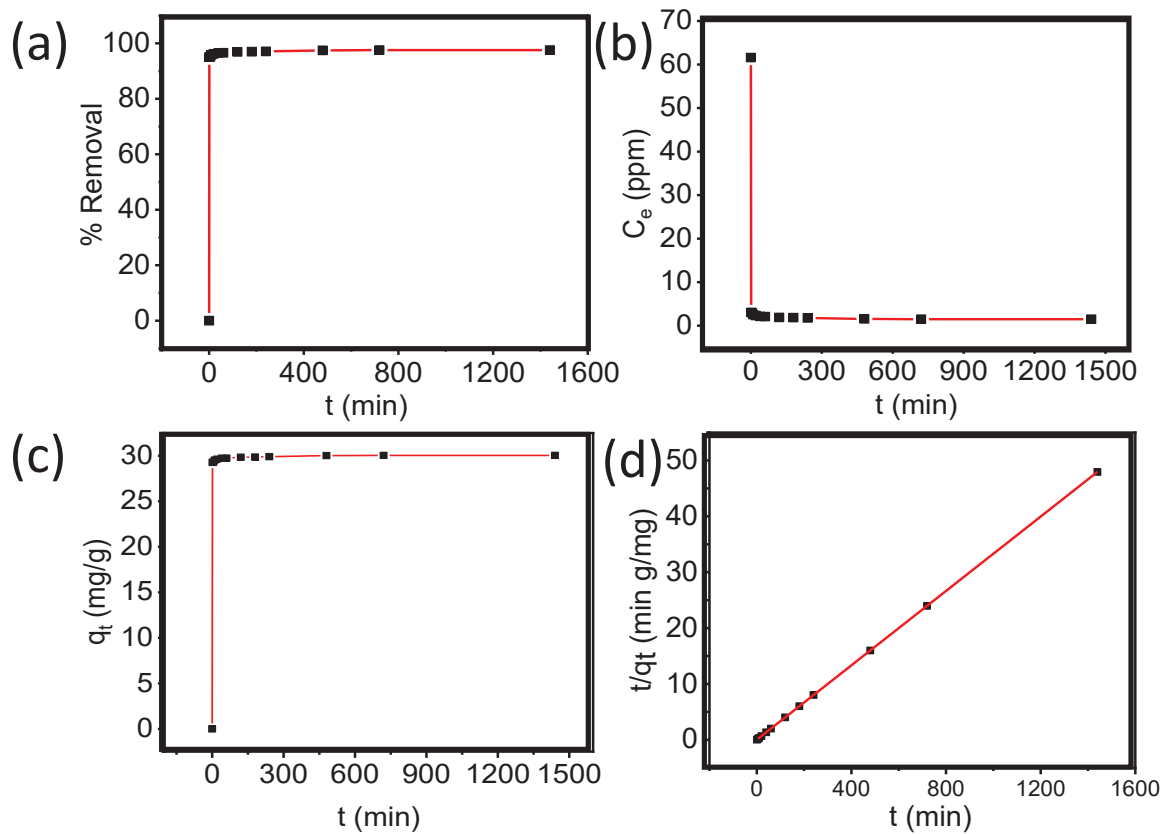


Figure 5. Sorption kinetics curve for Se (IV): (a) removal % of Se (IV) as a function of contact time (b) ion concentration change with contact time (c) sorption capacity (q_t) with contact time and (d) pseudo-second-order kinetic plots for Se (IV) sorption.

Table 5. Kinetic parameters for sorption of As (V) by Co, Al-LDH with two different models

	Adsorbate	R^2	$q_e(\text{exp})$	$q_e(\text{calc.})$	k (g/mg/min)
Pseudo 1 st order	As(V)	0.86	51.83	2.52	2.14×10^{-3}
Pseudo 2 nd order	As(V)	0.99	51.83	51.86	1.05×10^{-2}

Table 6. Kinetic parameters for sorption of Se(IV) by Co, Al-LDH with two different models

	Adsorbate	R ²	q _e (exp)	q _e (calc.)	k(g/mg/min)
Pseudo 1 st order	Se (IV)	0.51	30.04	6.34	3.632x10 ⁻³
Pseudo 2 nd order	Se (IV)	1.0	30.04	30.04	3.99x10 ⁻²

Studies at different pH.

pH stability plays an important role in the manifestation of a material. Co, Al-LDH shows stability in wide pH range of 1.93 to 12.22. It is well known that arsenate form H_2AsO_4^- dominates at low pH, which is less than about pH 6.9 and at high pH, HAsO_4^{2-} is dominant. Similarly, selenite species exists at pH=5 as HSeO_3^- , at pH=7, as equi-combination of HSeO_3^- and SeO_3^{2-} and at higher pH, contribution of SeO_3^{2-} increases. So it seems quite mandatory to find out the efficiency of LDH in contaminated water of different pH. We have seen that the percentage removal of oxoanions is not much affected by pH. (Table 7 and 8) However, at very high pH, slight decrement in percentage removal is observed. It may be due to the broad coverage of plenty of OH^- ions on positively charged layers of LDH, which can hinder the surface adsorption of oxoanions.

Table 7: Removal of As (V) at different pH

pH	C_i (ppm)	C_f (ppm)	% Removal	q (mg/g)	K_d (mL/g)
1.17	81.31	29.59	63.60	25.86	0.87×10^3
2.6	111.7	19.42	82.61	46.14	2.37×10^3
3.85	112.7	10.9	90.32	50.9	4.66×10^3
5.6	111	7.69	93.07	51.65	6.71×10^3
7.5	115.6	4.27	96.30	55.66	13.01×10^3
9.8	113.1	5.09	95.4	54.00	10.59×10^3
11.35	110.9	13.88	87.48	48.51	3.49×10^3
12.5	85.91	13.71	84.04	36.1	2.63×10^3

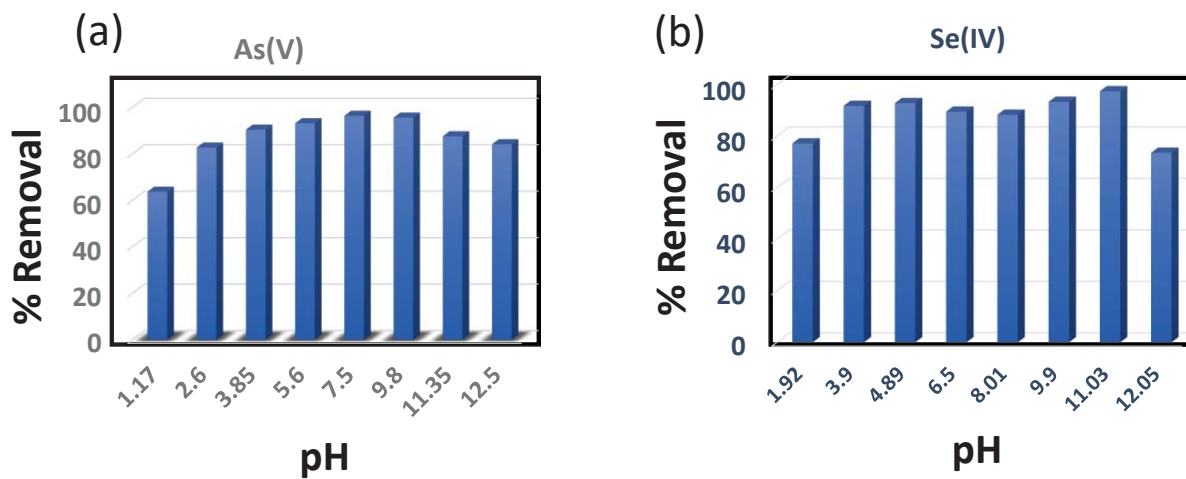
**Figure 6.** Percentage Removal at different pH (a) for As (V) and (b) for Se (IV)

Table 8: Removal of Se (IV) at different pH

pH	C_i (ppm)	C_f (ppm)	% Removal	q (mg/g)	K_d (ml/g)
1.92	62.13	14.19	77.16	23.97	1.68×10^3
3.9	56.25	4.65	91.72	25.79	5.54×10^3
4.89	66.85	4.81	92.79	31.01	6.43×10^3
6.5	67.12	7.06	89.47	30.02	4.25×10^3
8.01	68.11	7.97	88.29	30.06	3.77×10^3
9.9	67.28	4.5	93.31	31.39	6.97×10^3
11.03	66.97	1.73	97.41	32.62	18.85×10^3
12.05	57.73	15.28	73.53	21.22	1.38×10^3

Competitive ion exchange studies.

To analyze whether this material is selective for oxoanions of As (V) and Se (IV) or not, competitive ion exchange experiments are performed. The obtained results (Figure. 7) indicate that the presence of F^- , Cl^- , Br^- , I^- , NO_3^- and SO_4^{2-} does not affect the capture efficiency of oxoanions. Even the

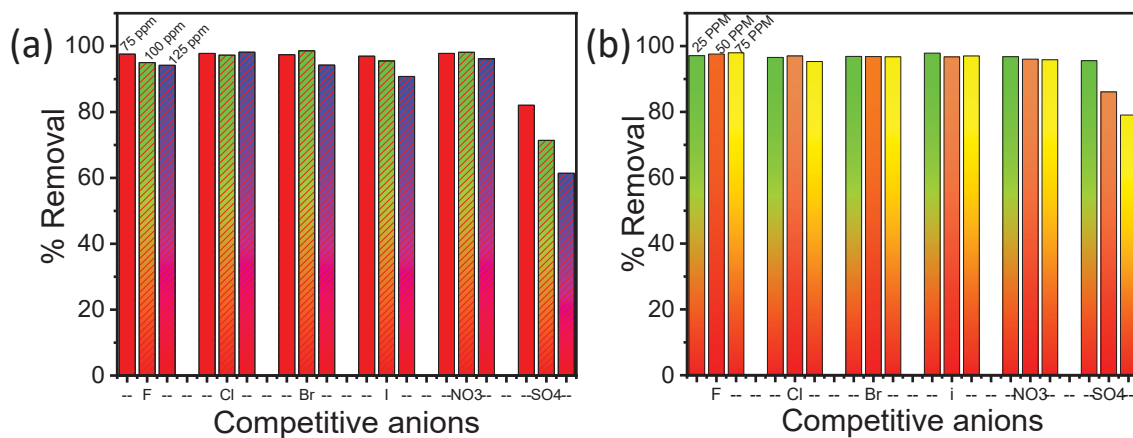


Figure 7. Percentage Removal of (a) As (V) and (b) Se (IV) in presence of various competitive anions (F^- , Cl^- , Br^- , I^- , NO_3^- , SO_4^{2-}) at different concentrations.

the different concentrations of other competitive anions are also not the matter of concern for LDH during sequestration of oxoanions. This favours the highly selective nature of Co, Al-LDH towards these toxic oxoanions AsO_4^{3-} and SeO_3^{2-} .

3.2.3.3. Post-adsorption qualitative analysis and sorption mechanism

After the sorption experiments, the solid samples were air-dried to conduct XRD and IR analyses to establish the adsorption mechanism. The PXRD pattern of As (V) and Se (IV) adsorbed material resembles with that of pristine LDH, which signifies the occurrence of topotactic sorption. We have observed the clear shift of basal peak to lower angle as shown in Figure. 8b.

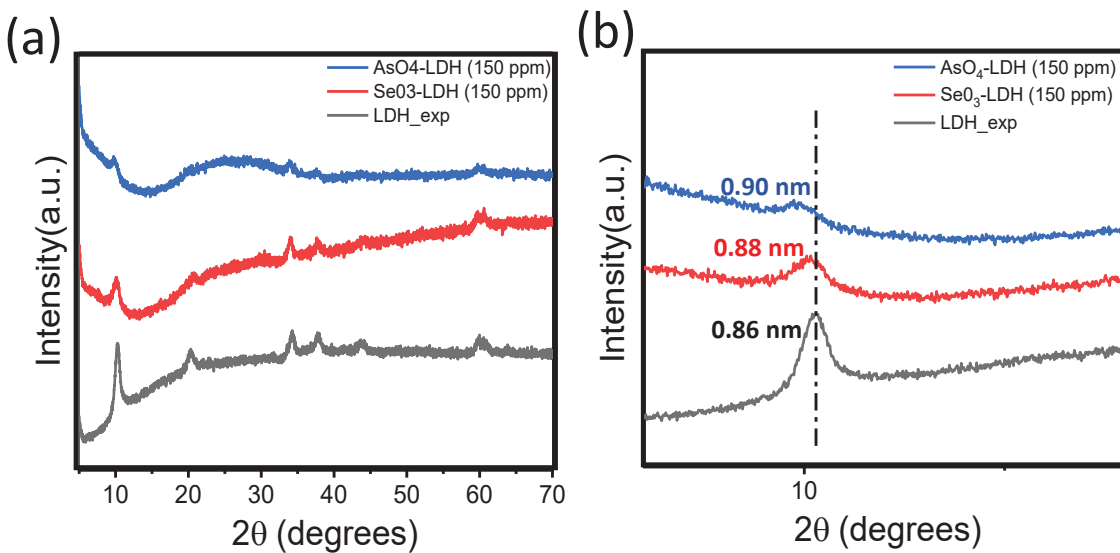


Figure 8. (a)PXRD pattern of Co, Al-LDH after adsorption, (b) zoomed view of PXRD pattern.

This shifted peak indicates the increased basal spacing between the layers of LDH. In case of As (V) adsorption, this increment is from 0.86 nm to 0.90 nm and for Se (IV) adsorption, shift is from 0.86 nm to 0.88 nm. This data facilitates the ion-exchange mechanism. When CO_3^{2-} intercalated LDH encounter the oxoanions environment, these oxoanions get exchanged with the trivalent carbonate ions and due to their larger size than carbonate, the LDH gallery gets widened.

The FTIR spectra also confirms the anion exchange mechanism. After adsorption, the peak (at 1365 cm^{-1}) attributed to CO_3^{2-} gets diminished, implying the removal of carbonate anions from

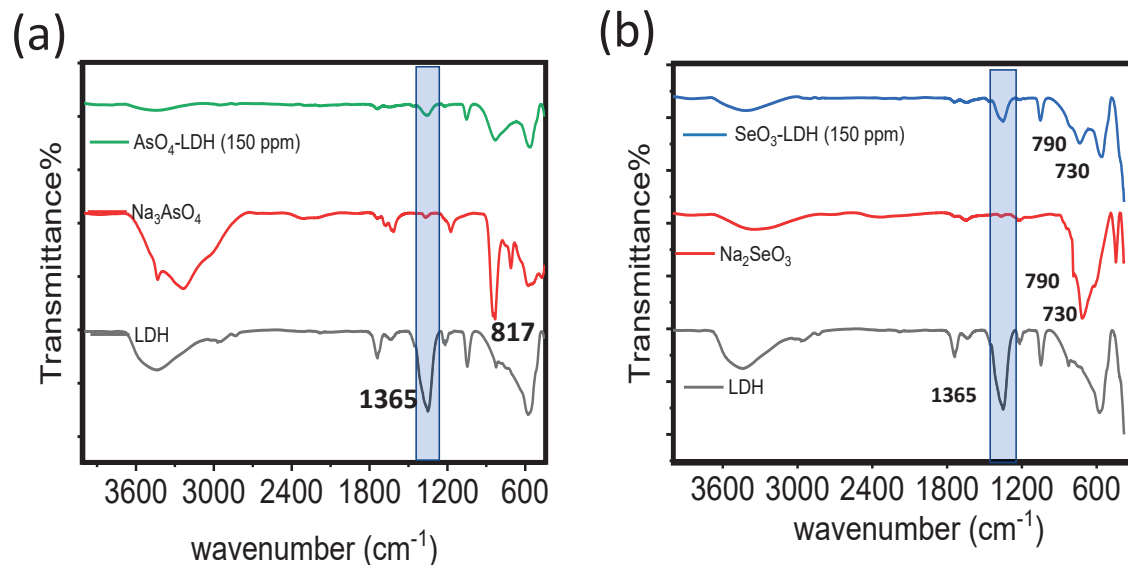


Figure 9. FTIR spectra of Co, Al-LDH after adsorption of (a) As (V) and (b) Se (IV)

Table 9: Comparison of Sorption capacities of various adsorbents for As (V)

Adsorbents	q_m (mg/g)	Reference
CoAl-CO ₃ -LDH	129	This work
MgAl-MoS ₄ -LDH	56	17
Fe-BTC _a	12	18
MNPs	16	19
SMZY-100-S	1.3	20
PPhSi-MNPs	50	21
MgAl-LDH	58	22
CaFe-Cl-LDH	4.6	23
MgAl-CO ₃ -LDH	32.6	24

the LDH gallery. Also, the signature of $\nu_{\text{As-O}}$ at 817 cm^{-1} and $\nu_{\text{Se-O}}$ at 790 cm^{-1} , 730 cm^{-1} are observed in the spectra of $\text{AsO}_4\text{-LDH}$ and $\text{SeO}_3\text{-LDH}$ respectively (Figure. 9b.), confirming the entrance of oxoanions (AsO_4^{3-} and SeO_3^{2-}) into the LDH gallery.

Table 10: Comparison of Sorption capacities of various adsorbents for Se (IV)

Adsorbents	q_m (mg/g)	Reference
CoAl-CO ₃ -LDH	130	This work
MgAl-CO ₃ -LDH	30–90	25
Mg, Al-Cl-LDH	119	26
Mg/Al (Zn/Al)-LDH	119	26
OPBent-2	5.0	27
sulfuric-acid-treated peanut shell	43.0	28
CuFe ₂ O ₄	14.1	29
NU-1000	102	30

3.2.4. Conclusion and future outlook

In conclusion, we have shown that the nature-inspired coral like layered Co, Al-LDH selectively and efficiently sequesters toxic oxoanions of As (V) and Se (IV) in a very wide pH range from ~1.9 to ~12.5 and with a high capacity of 129.22 mg g^{-1} for As (V) and 130.56 mg g^{-1} for Se (IV). The high adsorption capacity for As (V) and Se (IV) are superior to other reported adsorbents, indicating the great potential of this material for trapping these oxoanions. The adsorption equilibrium is reached within ten minutes for both of them, indicating very rapid removal of As (V) and Se (IV) from wastewater by Co, AL-LDH. The reason for rapid removal can be attributed

to the weak bonding interaction between SeO_3^{2-} and AsO_4^{3-} towards brucite-like layers which promotes the efficient anion exchange. In future, to explore the detailed mechanism, we will do characterization of post adsorbed materials by the techniques like Raman, FESEM, Zeta potential and XPS. We will also do ppb level removal and regeneration study of the As and Se sorbed LDH material and finally we will make a prototype cartridge for practical applications.

3.2.5. References

1. Chakraborti, D.; Das, B.; Rahman, M. M.; Chowdhury, U. K.; Biswas, B.; Goswami, A. B.; Nayak, B.; Pal, A.; Sengupta, M. K.; Ahamed, S., Status of groundwater arsenic contamination in the state of West Bengal, India: A 20-year study report. *Mol. Nutr. Food Res.* **2009**, *53* (5), 542-551.
2. Leupin, O. X.; Hug, S. J.; Badruzzaman, A., Arsenic removal from Bangladesh tube well water with filter columns containing zerovalent iron filings and sand. *Environ. Sci. Technol.* **2005**, *39* (20), 8032-8037.
3. Michael, H. A., An arsenic forecast for China. *Science* **2013**, *341* (6148), 852-853.
4. Guha Mazumder, D., Chronic arsenic toxicity: clinical features, epidemiology, and treatment: experience in West Bengal. *J. Environ. Sci. Health* **2003**, *38* (1), 141-163.
5. Water, S.; Organization, W. H., Guidelines for drinking-water quality [electronic resource]: incorporating first addendum. Vol. 1, Recommendations. **2006**.
6. Associates, A., *Arsenic in Drinking Water Rule Economic Analysis*. United States Environmental Protection Agency, Office of Ground Water.: 2000.
7. Fordyce, F., Selenium geochemistry and health. *Ambio* **2007**, 94-97.
8. Organization, W. H., *Trace elements in human nutrition and health*. World Health Organization: 1996.
9. Zhu, Q.; Li, J.-G.; Zhi, C.; Ma, R.; Sasaki, T.; Xu, J.; Liu, C.; Li, X.; Sun, X.; Sakka, Y., Nanometer-thin layered hydroxide platelets of $(Y_{0.95}Eu_{0.05})_2(OH)_5NO_3 \cdot x H_2O$: exfoliation-free synthesis, self-assembly, and the derivation of dense oriented oxide films of high transparency and greatly enhanced luminescence. *J. Mater. Chem.* **2011**, *21* (19), 6903-6908.
10. WHO., Guidelines for drinking-water quality. *WHO Chronicle* **2011**, *38* (4), 104-108.
11. Jadhav, S. V.; Bringas, E.; Yadav, G. D.; Rathod, V. K.; Ortiz, I.; Marathe, K. V., Arsenic and fluoride contaminated groundwaters: a review of current technologies for contaminants removal. *Environ. Manag. Today* **2015**, *162*, 306-325.
12. Li, Y.; Yuan, H.; von Dem Bussche, A.; Creighton, M.; Hurt, R. H.; Kane, A. B.; Gao, H., Graphene microsheets enter cells through spontaneous membrane penetration at edge asperities and corner sites. *Proc. Natl. Acad. Sci.* **2013**, *110* (30), 12295-12300.
13. Ruan, X.; Chen, Y.; Chen, H.; Qian, G.; Frost, R. L., Sorption behavior of methyl orange from aqueous solution on organic matter and reduced graphene oxides modified Ni-Cr layered double hydroxides. *Chem. Eng. Prog.* **2016**, *297*, 295-303.

14. Gérardin, C.; Kostadinova, D.; Sanson, N.; Coq, B.; Tichit, D., Supported metal particles from LDH nanocomposite precursors: control of the metal particle size at increasing metal content. *Chem. mater.* **2005**, *17* (25), 6473-6478.
15. Rathore, E.; Maji, K.; Biswas, K., Nature-Inspired Coral-like Layered $[\text{Co}_{0.79}\text{Al}_{0.21}(\text{OH})_2(\text{CO}_3)_{0.11}] \cdot m \text{H}_2\text{O}$ for Fast Selective ppb Level Capture of Cr (VI) from Contaminated Water. *Inorg. Chem.* **2021**, *60* (13), 10056-10063.
16. Gao, H.; Cao, R.; Xu, X.; Xue, J.; Zhang, S.; Hayat, T.; Alharbi, N. S.; Li, J., Surface area-and structure-dependent effects of LDH for highly efficient dye removal. *ACS Sustain. Chem. Eng.* **2018**, *7* (1), 905-915.
17. Ma, L.; Islam, S. M.; Liu, H.; Zhao, J.; Sun, G.; Li, H.; Ma, S.; Kanatzidis, M. G., Selective and efficient removal of toxic oxoanions of As (III), As (V), and Cr (VI) by layered double hydroxide intercalated with MoS_4^{2-} . *Chem. Mater.* **2017**, *29* (7), 3274-3284.
18. Zhu, B.-J.; Yu, X.-Y.; Jia, Y.; Peng, F.-M.; Sun, B.; Zhang, M.-Y.; Luo, T.; Liu, J.-H.; Huang, X.-J., Iron and 1, 3, 5-benzenetricarboxylic metal-organic coordination polymers prepared by solvothermal method and their application in efficient As (V) removal from aqueous solutions. *J. Phys. Chem. C* **2012**, *116* (15), 8601-8607.
19. Liu, C.-H.; Chuang, Y.-H.; Chen, T.-Y.; Tian, Y.; Li, H.; Wang, M.-K.; Zhang, W., Mechanism of arsenic adsorption on magnetite nanoparticles from water: thermodynamic and spectroscopic studies. *Environ. Sci. Technol.* **2015**, *49* (13), 7726-7734.
20. Yusof, A. M.; Malek, N. A. N. N., Removal of Cr (VI) and As (V) from aqueous solutions by HDTMA-modified zeolite Y. *J. Hazard. Mater.* **2009**, *162* (2-3), 1019-1024.
21. Badruddoza, A. Z. M.; Shawon, Z. B. Z.; Rahman, M. T.; Hao, K. W.; Hidajat, K.; Uddin, M. S., Ionically modified magnetic nanomaterials for arsenic and chromium removal from water. *Chem. Eng. Prog.* **2013**, *225*, 607-615.
22. Bujdosó, T.; Patzkó, Á.; Galbács, Z.; Dékány, I., Structural characterization of arsenate ion exchanged MgAl-layered double hydroxide. *Appl. Clay Sci.* **2009**, *44* (1-2), 75-82.
23. Xu, Y.; Dai, Y.; Zhou, J.; Xu, Z. P.; Qian, G.; Lu, G. M., Removal efficiency of arsenate and phosphate from aqueous solution using layered double hydroxide materials: intercalation vs. precipitation. *J. Mater. Chem.* **2010**, *20* (22), 4684-4691.
24. Lazaridis, N.; Hourzemanoglou, A.; Matis, K., Flotation of metal-loaded clay anion exchangers. Part II: the case of arsenates. *Chemosphere* **2002**, *47* (3), 319-324.
25. Chubar, N., EXAFS and FTIR studies of selenite and selenate sorption by alkoxide-free sol-gel generated Mg-Al-CO₃ layered double hydroxide with very labile interlayer anions. *J. Mater. Chem. A* **2014**, *2* (38), 15995-16007.

26. Mandal, S.; Mayadevi, S.; Kulkarni, B. D., Adsorption of aqueous selenite [Se (IV)] species on synthetic layered double hydroxide materials. *Ind. Eng. Chem. Res.* **2009**, *48* (17), 7893-7898.
27. Orucoglu, E.; Hacıyakupoglu, S., Bentonite modification with hexadecylpyridinium and aluminum polyoxy cations and its effectiveness in Se (IV) removal. *Environ. Manag. Today* **2015**, *160*, 30-38.
28. El-Shafey, E., Removal of Se (IV) from aqueous solution using sulphuric acid-treated peanut shell. *Environ. Manag. Today* **2007**, *84* (4), 620-627.
29. Sun, W.; Pan, W.; Wang, F.; Xu, N., Removal of Se (IV) and Se (VI) by MFe₂O₄ nanoparticles from aqueous solution. *Chem. Eng. Sci.* **2015**, *273*, 353-362.
30. Howarth, A. J.; Katz, M. J.; Wang, T. C.; Platero-Prats, A. E.; Chapman, K. W.; Hupp, J. T.; Farha, O. K., High efficiency adsorption and removal of selenate and selenite from water using metal–organic frameworks. *J. Am. Chem. Soc.* **2015**, *137* (23), 7488-7494.

Biography



Animesh Das was born on September 23, 1998, in Bardhaman, West Bengal (India). He did his B.Sc. Hons. Chemistry (2016) from Jadavpur University, Kolkata. He joined as an Int. PhD student (Chemical Sciences) at New Chemistry Unit of Jawaharlal Nehru Centre for Advanced Scientific Research (JNCASR), Bangalore, India in August 2019. He received the prestigious Bapu Matru Prasad Scholarship 2020, for securing highest CGPA in courses in 1st year Int. Ph.D. programme in Chemical Sciences. Currently, he is working with Prof. Kanishka Biswas as MS student from May 2020. His research work is focused on thermoelectric energy conversion and removal of heavy metals from wastewater.